Coherent Optical Access Networks: Rate Dynamic and Multiple Access

Zixian Wei

Department of Electrical & Computer Engineering
McGill University
Montréal, Québec, Canada

June 13, 2024

A thesis submitted to McGill University in partial fulfllment of the requirements of the degree of Doctor of Philosophy.

Abstract

Coherent technology is a competitive candidate for next-generation 100/200-G passive optical networks (PON) with 40 km coverage. The characteristics of linear optical field conversion, digital compensation, and superior receiver sensitivity enable coherent PON (CPON) to have higher capacity, larger coverage extended reach, and higher density support. The evolution of access networks' scale, scalability, and flexibility leads to a series of dynamic behaviors in CPON. In this thesis, the selected topics related to potential business issues, including rate flexibility, parameters monitoring, dynamic encryption, and service fairness of downstream links over CPON are analyzed and demonstrated emphatically.

This thesis first explores and demonstrates point-to-point (P2P) and point-to-multipoint (P2MP) coherent optical communication systems and access networks. A time-variant entropy-regulated probabilistic constellation shaping (PCS) 64-quadrature amplitude modulation (64-QAM) scheme is proposed. Then, an active learning-aided entropy-tunable automatic modulation identification (AL-aided ET-AMI) scheme is demonstrated. The dynamic time-varying entropy is embedded in the constellation diagram and is re-extracted at the receiver. A 10-km/ 350 $\sim$ 550-Gb/s result is achieved over

a 10-km link within hard-decision-forward error correction (HD-FEC). For an entropy tuning step with 0.1, the recognition accuracy of AL-aided ET-AMI can reach 98% with data aggregation. This scheme was subsequently extended to P2MP access networks. Our proposed scheme can provide an abundant system loss budget and fast graphical monitoring for flexible coherent optical transmission systems and networks.

Physical layer security is becoming an important topic in the commercial deployment of ultra-100-G optical access networks. With the regulation of initial entropies, the PCS-based optical link can realize a bit stream with a tunable data rate, which facilitates mass multi-rate access. Digital signal processing (DSP) chaotic encryption attracts more and more attention in fiber-optic networks. We first demonstrate a chaotic-encrypted transmission on a PCS-based rate-flexible CPON. The transmitted signal with various entropy is encrypted and converted into a cipher via mapping from PCS-64-QAM to pseudo-m-QAM format. Net rate tuning from 211.80 Gb/s to 348.12 Gb/s with a step size of 3.408 Gbps/pol./λ is achieved by 0.1-step entropy interval at an ROP of -15 dBm, encrypted by different parallel chaotic sequences. This work provides a feasible solution for next-generation >100-G rate-flexible and physical layer security-enhanced optical transmission.

Finally, a time division multiplexing non-orthogonal multiple access scheme is proposed for high-capacity and dense-access CPON. The scheme is experimentally demonstrated between two far-near ONUs over CPON within a single timeslot with different transmission distances and split ratios. Different fairness indexes are defined and adopted to verify the fairness of the service from the OLT to the two far-near users. Four experiments are demonstrated with four coherent PON application scenarios.

A 400-Gb/s rate is achieved for two far-near users within HD-FEC and flexible HD-FECs. The signal-to-interference noise ratios or bit-error rates of far-near two users are almost the same. Our proposed scheme can provide a fair service for next-generation wide-coverage coherent optical access systems.

Résumé

La technologie cohérente est un candidat compétitif pour les réseaux optiques passifs (PON) de prochaine génération 100/200-G avec une couverture de 40 km. Les caractéristiques de conversion linéaire du champ optique, de compensation numérique et de sensibilité supérieure du récepteur permettent au PON cohérent (CPON) d'avoir une capacité plus élevée, une couverture étendue plus large et un support de densité plus élevée. L'évolution de l'échelle, de l'évolutivité et de la flexibilité des réseaux d'accès conduit à une série de comportements dynamiques dans le CPON. Dans cette thèse, les sujets sélectionnés liés aux problèmes commerciaux potentiels, y compris la flexibilité du débit, la surveillance des paramètres, le cryptage dynamique et l'équité du service des liaisons descendantes sur CPON, sont analysés et démontrés de manière rigoureuse.

Cette thèse explore et démontre d'abord les systèmes de communication optique cohérente point à point (P2P) et point à multipoint (P2MP) et les réseaux d'accès. Un schéma de modulation d'amplitude en quadrature 64 (64-QAM) façonné par constellation probabiliste régulée par l'entropie variant dans le temps (PCS) est proposé. Ensuite, un schéma d'identification automatique de modulation réglable par entropie as-

sisté par apprentissage actif (AL-aided ET-AMI) est démontré. L'entropie dynamique variable dans le temps est intégrée dans le diagramme de constellation et est ré-extraitée au récepteur. Un résultat de 10 km / 350 $\sim$ 550-Gb/s est atteint sur une liaison de 10 km dans le cadre de la correction d'erreurs en avant à décision dure (HD-FEC). Pour une étape de réglage de l'entropie de 0,1, la précision de reconnaissance de l'AL-aided ET-AMI peut atteindre 98 % avec l'agrégation des données. Ce schéma a ensuite été étendu aux réseaux d'accès P2MP. Notre schéma proposé peut fournir un budget de perte système abondant et une surveillance graphique rapide pour des systèmes et réseaux de transmission optique cohérente flexible.

La sécurité de la couche physique devient un sujet important dans le déploiement commercial des réseaux d'accès optiques ultra-100-G. Avec la régulation des entropies initiales, le lien optique basé sur le PCS peut réaliser un flux de bits avec un débit de données réglable, ce qui facilite l'accès multi-débit en masse. Le cryptage chaotique par traitement de signal numérique (DSP) attire de plus en plus d'attention dans les réseaux à fibre optique. Nous démontrons d'abord une transmission cryptée chaotique sur un CPON flexible en termes de débit basé sur le PCS. Le signal transmis avec diverses entropies est crypté et converti en chiffre via le mappage du PCS-64-QAM au format pseudo-m-QAM. Le réglage du débit net de 211,80 Gb/s à 348,12 Gb/s avec une taille de pas de 3,408 Gbps/pol./λ est atteint par intervalle d'entropie de 0,1 pas à un ROP de -15 dBm, crypté par différentes séquences chaotiques parallèles. Ce travail fournit une solution réalisable pour une transmission optique flexible en termes de débit et améliorée en sécurité de la couche physique de prochaine génération $>$100-G.

Enfin, un schéma d'accès multiple non orthogonal à multiplexage par répartition dans le temps est proposé pour le CPON à haute capacité et accès dense. Le schéma est démontré expérimentalement entre deux ONUs éloignées-proches sur CPON dans un seul créneau temporel avec différentes distances de transmission et ratios de division. Différents indices d'équité sont définis et adoptés pour vérifier l'équité du service de l'OLT aux deux utilisateurs éloignés-proches. Quatre expériences sont démontrées avec quatre scénarios d'application de PON cohérent. Un débit de 400 Gb/s est atteint pour deux utilisateurs éloignés-proches dans le cadre du HD-FEC et des HD-FECs flexibles. Les rapports signal-bruit d'interférence ou les taux d'erreur binaire des deux utilisateurs éloignés-proches sont presque les mêmes. Notre schéma proposé peut fournir un service équitable pour les systèmes d'accès optique cohérents à large couverture de prochaine génération.

To my father.

Acknowledgements

As summer approaches in Montreal, I have finally ended my prolonged ten-year study journey after leaving my hometown in 2013. These ten years have been filled with unimaginable pain, and I am glad that I persevered through it. I am also grateful for the support from my family, knowing it has not been easy for them, especially for my mother, Qiuyan Lin.

I am deeply grateful to my supervisor, Prof. David V. Plant, who provided me with countless supports, a liberal academic atmosphere, well-equipped laboratories, and opportunities for deep connections with industry. What Prof. Plant has given me beyond the original definition of supervisor. I will never regret choosing McGill University in the winter of 2019, and in the following four years, as I reviewed my work round after round, I reshaped my own values towards natural sciences. At the same time, I would like to express my gratitude to my PhD supervisory committee, Prof. Ioannis Psaromiligkos, and Prof. Songrui Zhao, for their valuable and significant suggestions at every stage.

I achieved many milestones during my years at McGill University. I received the IEEE and SPIE International Graduate Awards for my contributions to optics and pho-

tonics. As the first McGill alumnus to be nominated and awarded the Marconi Society Paul Baran Young Scholar, the night in Washington, DC is a night I will never forget. I would like to thank John Janowiak, Joseph Kakande, Dennis Roberson, Vivian Chen, and others from the Young Scholars Committee Member for recognizing my work. I will always remember the encouragement delivered to me by Sir David N. Payne, Federico Faggin, Martin Cooper, and other Marconi fellows.

After I came to McGill University, I conducted a lot of research on high-speed optical communication systems and coherent access networks, many of which had groundbreaking significance for the entire community. 99% of the time is frustrating, but we still enjoy the 1% of wonderful moments after the struggle together. In the long run, we will never get tired of it. I would like to thank Ciena first for the use of the WaveLogic modem in my experiments. I would like to give special thanks to Jinsong Zhang. We helped each other and completed many work. I would also like to thank my colleagues, including Dr. Md Samiul Alam, Dr. Essam Berikaa, Dr. Deng Mao, Dr. Zhenping Xing, Dr. Xueyang Li, Aleksandar Nikic, Charles St-Arnault, Codey Nacke, Mostafa Khalil, Kh. Arif Shahriar, James Skoric, Ramon Gutierrez-Castrejo, Santiago Bernal, Weijia Li, Yannick D'Mello, and Yixiang Hu for all the precious moments spent fighting with you.

I would like to thank many international scholars for their support over the past few years, including Prof. Hongyao Fu, Prof. Lai Wang, and Prof. Yuhan Dong from Tsinghua University, Prof. Changyuan Yu from The Hong Kong Polytechnic University, Prof. Junbin Fang, Prof. Ji Zhou, and Prof. Huihui Lu from Jinan University, Prof. Chen Chen from Chongqing University, Prof. Yanbin Yang from Sichuan University,

and Prof. Chester Shu from The Chinese University of Hong Kong. I would also like to thank the international colleagues who collaborated with me, including Zhaoming Wang, Yuan Zhang, Zhenquan Zhao, Yibin Li, Bohua Deng, Zhongxu Liu, Zijian Li, and Chen Ding, for their dedication and efforts.

I am grateful again for the time I have had these four years. The red bird guided me onward. The Saint Lawrence River flows forever. The campus next to Mount Royal remained vivid for over 200 years. "You can check out any time you like but you can never leave!" I finally graduated but will never forget the journey in Montreal!

My sincere gratitude,

Zixian Wei

12, Feb., 2024

Associated Publications

The original contributions of all the research works presented in this thesis on the selected topics of CPON are based on the following 6 first-authored publications **(4 journal papers and 2 conference papers, 1 of which is under review)**. The contributions of the first author and other coauthors are stated for each paper below, respectively.

In addition, I have first-authored and co-authored other 9 publications **(5 journal papers and 4 conference papers)**, which are not directly related to this thesis, through collaborations with my colleagues at the Photonics Systems Group, the Department of Electrical and Computer Engineering (ECE), McGill University.

Journal Articles Directly Related to This Thesis:

1. **Zixian Wei**, Jinsong Zhang, Weijia Li, Charles St-Arnault, Santiago Bernal, Mostafa Khalil, Ramón Gutiérrez-Castrejón, Lawrence R. Chen, and David V. Plant, " Physical Layer Service Fairness of 200-Gbps TDM-NOMA Coherent Passive Optical Networks within Single Timeslot," submitted to J. Lightwave Technol., (2024). Under Reviewing.

In this work, I conceived, designed, and verified the idea, developed and performed the experiment, captured the data, and wrote the manuscript. Jinsong Zhang helped me to discuss and complete the experiment. The other co-authors contributed to revising the manuscripts.

2. **Zixian Wei**, Jinsong Zhang, Weijia Li, and David V. Plant, "Active Learning-aided CNN-based Entropy-tunable Automatic Modulation Identification for Rate-flexible Coherent Optical System," J. Lightwave Technol., 41(14), 4598-4608 (2023).

In this work, I conceived, designed, and verified the idea, developed and performed the experiment, captured the data, and wrote the manuscript. Jinsong Zhang helped me to discuss and complete the experiment. The other co-authors contributed to revising the manuscripts.

3. **Zixian Wei**, Jinsong Zhang, Weijia Li, and David V. Plant, "400-Gbps/80-km Rate-flexible PCS-64-QAM WDM-CPON with Pseudo-m-QAM Chaotic Physical Layer Encryption," J. Lightwave Technol., 41(8), 2413-2424 (2023).

In this work, I conceived, designed, and verified the idea, developed and performed the experiment, captured the data, and wrote the manuscript. Jinsong Zhang helped me to discuss and complete the experiment. The other co-authors contributed to revising the manuscripts.

4. **Zixian Wei**, Jinsong Zhang, Weijia Li, and David V. Plant, "Time-variant Entropy Regulated Multiple Access for Flexible Coherent PON," Opt. Lett., 47(19), 5148-5151, (2022)

In this work, I conceived, designed, and verified the idea, developed and performed the experiment, captured the data, and wrote the manuscript. Jinsong Zhang helped me to discuss and complete the experiment. The other co-authors contributed to revising the manuscripts.

Conference Proceedings Directly Related to This Thesis:

5. **Zixian Wei**, Jinsong Zhang, Weijia Li, and David V. Plant, ”TDMA Frame Design and Demonstration of Encrypted Coherent Fronthaul with Flexible and Monitored Rate”, Conference on Lasers and Electro-Optics (CLEO), Paper SF2M.4, San Jose, California, USA, Mar., (2023). (Oral)

In this work, I conceived, designed, and verified the idea, developed and performed the experiment, captured the data, and wrote the manuscript. Jinsong Zhang helped me to discuss and complete the experiment. The other co-authors contributed to revising the manuscripts

6. **Zixian Wei**, Jinsong Zhang, Weijia Li, and David V. Plant, ”On the Rate Monitoring Performance of Active Learning-based Classifier for PCS-based Rate-flexible TWDM-CPON”, Conference on Optical Fiber Communication (OFC), Paper W2A.21, San Diego, California, USA, Mar., (2023).

In this work, I conceived, designed, and verified the idea, developed and performed the experiment, captured the data, and wrote the manuscript. Jinsong Zhang helped me to discuss and complete the experiment. The other co-authors contributed to revising the manuscripts.

Journal Articles Not Related to This Thesis:

1. **Zixian Wei**, Codey Nacke, Mostafa Khalil, Hao Sun, Kyle Stitt, James Lougheed, Lawrence Chen, and David V. Plant, “AL-aided AMC in multi-user white-light OFDMA VLC system over a light-diffusing fiber loop,” Opt. Lett., 48(14), 3661-3664 (2023)

In this work, I conceived, designed, and verified the idea, developed and performed the experiment, captured the data, and wrote the manuscript. Codey Nacke helped me to discuss and complete the experiment. The other co-authors contributed to revising the manuscripts

2. Jinsong Zhang, Luhua Xu, Deng Mao, Yannick D'Mello, **Zixian Wei**, Weijia Li, and David V. Plant, "Temperature-insensitive and low-loss single-mode silicon waveguide crossing covering all optical communication bands enabled by curved anisotropic metamaterial," Nanophotonics, (2023)

3. Weijia Li, Luhua Xu, **Zixian Wei**, Jinsong Zhang, Deng Mao, Yannick D'Mello, David V. Plant, "Silicon photonic broadband polarization-insensitive switch based on polarization-mode diversity conversion," Opt. Lett., (2023).

4. Jinsong Zhang, Essam Berikaa, Ramon Gutierrez-Castrejon, Md Samiul Alam, Fabio Cavaliere, Stephane Lessard, **Zixian Wei**, Weijia Li, and David V. Plant, "PAPR reduction and nonlinearity mitigation of optical digital subcarrier multiplexing systems with a silicon photonics transmitter," J. Lightwave Technol., (2023).

5. Weijia Li, Luhua Xu, Jinsong Zhang, Deng Mao, Yannick D'Mello, **Zixian Wei**, David V. Plant, "Broadband Polarization-insensitive Thermo-optic Switches on a 220-nm Silicon-on-insulator Platform," IEEE Photonics Journal, pp. 1-7, (2022)

Conference Proceedings Not Related to This Thesis:

6. Charles St-Arnault, Santiago Bernal, Ramon Gutierrez-Castrejon, Essam Berikaa, **Zixian Wei**, Janina Rautert, Sergey Poltavtsev, Alexey E. Gubenko, Vasilii Belykh, Vladimir Mikhrin, Alexey Kovsh, David Plant, "Performance comparison of QD-SOA, QW-SOA, Bulk-SOA, and PDFA for multi-Tbps O-band WDM links ", M3E, 24-28 March 2024, San Diago, OFC 2024. (Oral)

7. Santiago Bernal, Mario Dumont, Essam Berikaa, Charles St-Arnault, Yixiang Hu, Ramon Gutierrez-Castrejon, **Zixian Wei**, Antonio D'Errico, Alessandra Bigongiari,

Luca Giorgi, Stefano Stracca, Robert Brunner, Stephane Lessard, Fabio Cavaliere, John Bowers, David Plant, ”8.5 Tbps Net SiP O-band Coherent Transmission over 10 km Using a Quantum-Dot Mode-Locked Comb Laser ”, M3E, 24-28 March 2024, San Diago, OFC 2024. (Oral)

8. Weijia Li, Luhua Xu, **Zixian Wei**, Deng Mao, Jinsong Zhang, Yannick D'Mello, and David V. Plant, ”2×2 Broadband Thermo-optic Polarization-insensitive Switch on the SOI Platform”, Conference on Lasers and Electro-Optics (CLEO), Paper STu3J. 5, San Jose, California, USA, Mar., (2023). (Oral)

9. Luhua Xu, Weijia Li, Jinsong Zhang, Deng Mao, Md Samiul Alam, Yannick D'Mello, Santiago Bernal, **Zixian Wei**, and David V. Plant, ”Broadband High-Performance 2 × 2 MMI 3-dB Coupler Enabled by SWG Lateral Cladding for the Silicon-on-Insulator Platform”, Conference on Optical Fiber Communication (OFC), Paper Th2A.5, San Diego, California, USA, Mar., (2023).

Table of Contents

List of Figures

List of Tables

Chapter 1

Introduction

1.1 Motivation

1.1.1 Access-side Traffic Growth

In recent years, the development of access networks has been affected by various reasons, including technological innovation, market demand, policies and regulations, *etc.* Among them, the rapid growth of traffic on the access side is the main driving force for the evolution of access networks to the next generation [1, 2, 3].

The development history of access networks can be traced back to the early stages of computer networks. With the popularization and development of the Internet, the evolution of access networks has mainly gone through two important stages. The first stage (1980s-1990s) was the dial-up Internet era when the Internet was just emerging. The broadband access era from the early 2000s to the present is the second stage. Digital subscriber lines (DSL) [4], cable modems, fiber-to-the-home (FTTH), *etc.* are iconic technology routes [5, 6]. FTTH based on Passive Optical Networks (PON) has made a significant mark in the history of optical communications over the past two decades and achieved great market success. Users can get faster Internet speeds and more stable connection quality. The new architecture of next-generation PON and the digital signal processing (DSP) in it are also the subject of this thesis.

In recent years, new consumer electronics products and new Internet applications have spurred continuous growth in access-side traffic. On the one hand, users' demands for high-speed broadband, multimedia content, and cloud services are increasing, prompting operators and equipment manufacturers to accelerate the launch of more advanced access technologies and products. On the other hand, the rapid development of emerging applications such as 5G, Internet of Things, and cloud computing has put forward higher requirements for the performance and capabilities of access networks, promoting the development and upgrading of access network technology [7, 8].

1.1.2 PON Development History

In scenarios including beyond-fifth-generation/ sixth-generation (B5G/6G) wireless networks, Internet of Everything (IoE) systems, data center (DC) interconnections, 8K/16K video streaming, optical wireless communication, and cloud and extended reality (XR) services, the currently fixed optical access networks (OANs) are facing unprecedented pressure to support several hundred gigabit/s or even terabit/s aggregate rates [1, 9, 10, 11, 12, 13]. It also brought abundant market opportunities for the development of next-generation >100-G PON [13, 14]. In the coming beyond the fifth-generation/ sixth-generation (B5G/6G) era, the penetration rate of PON in the access network will continuously increase [15]. A passive optical network (PON) refers to a network framework from a single optical line terminal (OLT) to multiple optical network units/ terminals (ONUs/ONTs) without any active components. PON has the advantages of flexible networking, simple operation, strong anti-interference ability, low failure rate, high reliability, and low maintenance cost, which directly lead to the continuous increase in the popularity of wide fiber-to-the-X (FTTX, where X means home, office, cell, *etc.*) applications [16].

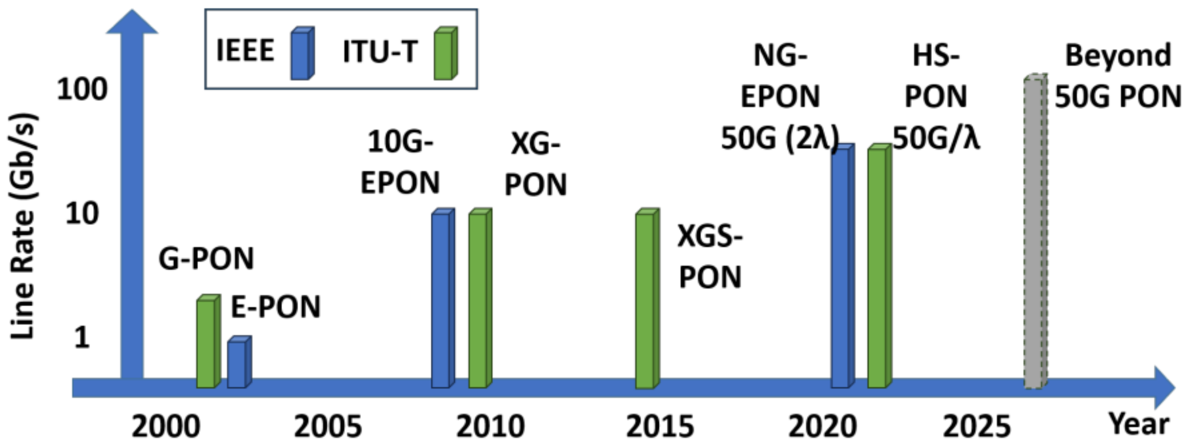

Figure 1.1: The roadmap for IEEE and ITU-T standards of PONs. This figure is reproduced from J. Zhou *et al.* [1]

After several generations of iterations during the last two decades, passive optical networks (PON) have achieved great success in the engineering development of fiber-to-the-X (FTTX) [17, 18]. The 50-Gbps PON based on intensity modulation and direct-detection (IM/DD) has been standardized and many telecommunication operators have begun to lay them out [19, 20]. From the PON standards defined by the Institute of Electrical and Electronics Engineers (IEEE) or the International Telecommunication

Union Telecommunications Standardization Sector (ITU-T), the service throughput is improving by a factor of nearly 4 times. Therefore, in recent years, 100/200-Gbps PON using multi-wavelength intensity modulation with direct detection (IM/DD) or coherent technology has triggered a new round of extensive discussion [21, 22]. In a traditional PON architecture, severing a range within 20 km, multiple end-users share the same front-fiber distributed connection, and the distribution and management of the fiber is done between a central device optical line terminal (OLT) and multiple optical network units (ONUs) [12]. Upgrading the next-generation fixed access networks, PON based on IM/DD fails to meet the requirements in terms of $>$100-Gbps aggregate capacity, $\sim$40-km covering range, and $<$1:64 access density [23]. Coherent PON is subsequently presented as a competitive candidate [24, 25, 26].

The demands for higher speed and more flexible rate regulation, higher security, and larger-scale user access continue to grow, which also promotes the current standardization process of PON [12, 27]. Time division-multiplied (TDM) and wavelength division-multiplexed (WDM) are two important deployment strategies in the early developmental history of PON [28]. For the standardization process, since 2013, time and wavelength division-multiplexing PON (TWDM-PON) has been selected as a basic solution for next-generation PON stage-2 (NG-PON2) by The Full Services Access Network Group (FSANG) [28, 29, 30]. Until 2019, 25/50G next-generation Ethernet PON (25/50G NG-EPON) with WDM specification and 50G single-wavelength time division multiplexing (TDM)-PON are launched and standardized by International Telecommunication Union-Telecommunications Standardization Sector (ITU-T)/ FSANG, respectively [19, 31]. Through the formulation and continuous improvement of these standards, as shown in Fig. 1.1, PON technology has been continuously improved and upgraded in terms of bandwidth, speed, delay, *etc.*, and has become one of the main technologies in modern access networks [1]. However, the mentioned PON solutions are all based on intensity modulation/direct detection (IM/DD) over the physical layer, which physically limits the development of >100-G PON. At the same time, coherent access was proposed to provide higher speed, sensitivity, and flexibility [32, 33]. As the prices of optical equipment and modules drop, the proposal of coherent solutions is greatly accepted by the market [34, 35]. Some recent experiments and field-trial reports [36] of high-speed flexible coherent PONs (FLCS-CPONs) combined with ultra-density WDM [37, 38], or TDM [39, 40], support the above view.

1.1.3 Next-generation Coherent PON

Coherent-based receivers in PON results in a longer-distance transmission capability and a higher receiving sensitivity, which makes it suitable for the applications of wider coverage and dense access, including urban, suburban, and rural areas [26]. However, the expansion of service scope makes the next-generation PON architecture have a larger and more complex topology, together with more complex service management and scheduling. Super-PON with wider spatial coverage ($\sim$50 km) became a widely recognized concept in the recent next-step evolution progress [41]. To prevent the performance of the ONU group from being limited by the worst receiving point in the network, rate flexibility is proposed to correspond to the bandwidth or other resource requirements of different ONUs [26, 42, 43]. Modulation format switching, bandwidth allocation, and constellation shaping have been proposed and experimentally proven to have cost reduction or excellent spectral efficiency performances [26, 44, 45, 46]. Even if the rate-fixed service, at a different time slot within a TDM-PON can be provided, the performance of the service will be affected due to different path losses and split ratios (SR). Specifically, it is reflected in the signal-to-noise ratio (SNR) and bit error rate (BER).

1.1.4 The Rate-flexible Access

The development of the Internet of Everything (IoE), the sharp increase in the number of mobile users, and the expansion of the network scale, all bring huge challenges to the traditional fixed-rate optical communication system in the beyond fifth-generation/ sixth-generation (B5G/ 6G) era [13, 47, 48]. To meet the exponentially growing data traffic and access numbers, the development of next-generation metropolitan core and aggregation optical networks is moving towards a system with higher data rates and more flexible regulation and monitoring [49]. The concepts of elastic optical networks (EONs) [50], agile optical networks (AONs) [51], and virtualized optical networks (VONs) have been proposed and developed over the past decade [52], and then a lot of adaptive modulation/ multiplexing schemes spanning multiple dimensions were designed to accommodate the aforementioned rate-flexible multi-rate access [53]. On the other hand, the traditional four-channel coherent optical communication system architecture with in-phase/ quadrature (I/Q) and dual polarization (X/Y) is not used by operators in medium/ short-distance access networks because of its uneconomical and impractical features. However, the trend of photonic integration and coherent sinking recently bring new development opportunities towards short-reach access optical links, especially in intra- and inter-data center links [54, 55]. Many techniques from hardware and software are widely discussed to reduce the architectural complexity, digital signal processing (DSP) complexity, and power consumption for coherent optical systems, without compromising their original high capacity, receiver sensitivity, and impairment compensation capability. Local oscillation-free (LO-free) down conversion schemes represented by Stokes vector detection [56] or Kramers-Kronig detection [57] have been successively proposed, which speed up the coherent sinking process. N. Suzuki *et al.* recently reviewed simplified digital coherent technologies for beyond-100G optical access network applications in the B5G/6G era [58]. Therefore, the development and application of short-range rate-flexible coherent technology are a potential direction next.

Flexibility access is an increasingly important issue on >100-G PON, which allows us to optimize the capacity of each independent transmission link through different dimensions [59]. The flexible PONs (FLCS-PONs) help to improve the performance of short-range optical interconnects according to the actual user's traffic requirements [60, 61, 62]. A large number of studies and demonstrations on rate-flexible optical communication systems have been realized by orthogonal frequency division multiplexed-PON (OFDM-PON). The flexible frequency-domain allocation characteristics of OFDM subcarriers enable rate adaptation possible for different access points in PON [62, 63]. However, the high peak-to-average power ratio (PAPR) characteristic of OFDM signals introduces a larger nonlinear phenomenon and limits the performance increase [63]. On the other hand, two-dimensional (2D) probabilistic constellation shaping (PCS) and geometric constellation shaping (GCS) are used to modify traditional m-level pulse amplitude modulation (m-PAM) or m-order quadrature amplitude modulation (m-QAM) formats for providing a solution closer to the specific channel capacity [64, 65]. According to the tunable spectral efficiency characteristic of PCS, a rate adaptation scheme is provided by regulating the shaping factor/ entropy of the signals. This technical route realizes a more continuous link rate control compared to the scheme of adjusting the frequency resources such as the number of subcarriers. [66, 67]. For example, R. Borkowski *et al.* proposed the concept and demonstrated 100-G FLCS-PON in a field trial, which is further prototyped with soft-input forward error correction (FEC) [59, 68].

1.2 Thesis Objective

According to the introductions and discussions presented in the previous Section, this thesis addresses the following research issues:

1. How can the physical layer parameters be monitored passively changing with the rate in an access network with a more complex topology?
2. How do we design dynamic encryption to make it difficult to miss-transmit and be attacked in dense access scenarios?
3. How do we achieve fairness in physical layer performance between far and near users in a wide-coverage access network to further ensure service quality?

Therefore, the objectives of this thesis are to:

1. Build 100G/200G coherent optical access network in a laboratory environment;

2. Design a graphical method to allow computer vision to dynamically monitor rate/entropy/signal-to-noise ratio;

3. Propose a simple and effective method to dynamically encrypt information for different transmission destinations at different rates;

4. Demonstrate NOMA research on service fairness at the physical layer in high-capacity ($>$ 100 Gbps) access networks.

1.3 Original contributions

In this section, we summarize our original contributions. The original contributions of this thesis can be grouped into three broad categories and summarized as follows:

Automatic Modulation Identification for Rate-flexible Coherent Optical Systems and Networks (Chapter 3)

Flexible rate and real-time link monitoring are important tasks in the development of software-defined EONs. The tunable spectral efficiency characteristic of probabilistic constellation shaping (PCS) naturally allows dynamic regulation of the rate for future optical communication systems. In this work, we first propose an active learning-aided entropy-tunable automatic modulation identification (AL-aided ET-AMI) scheme based on a convolution neural network (CNN) model for a PCS-based coherent optical system. An AL-based neural network allows monitoring of the link rate and signal-to-noise ratio (SNR) with tuning entropy or optical power fluctuation. The proposed AL-aided ET-AMI scheme is demonstrated over a 350 $\sim$ 550-Gbps line rate 10-km dual-polarized coherent optical communication system at entropies from

3.5 to 5.5. When the entropy tuning step is 0.1, corresponding to a rate tuning step of 5 Gbps at 50 Gbaud, the recognition accuracy can reach 98% with data aggregation (DA). When the fluctuation of SNR is 1 dB, the recognition rate can reach 87% at an entropy of 4.5 over 400 samples. The verifications show that our proposed AL-aided ET-AMI solution can monitor the rate and SNR performance of PCS-based high-speed rate-flexible optical links well. The solution provides a new perspective and tool for future optical systems and network monitoring.

We further propose a time-variant entropy-regulated multiple access scheme, which can further expand the capacity of FLCS-CPONs via time slot allocation. By changing the entropy values from 3.5 to 5.5, the OLT transmitter (Tx.) can send data frames of any length in any time slot at 5 rate levels. The ONU receiver (Rx.) distinguishes different users via the entropy values, which can be obtained using an image classifier designed for constellation monitoring. A real-time coherent transmission setup is implemented, in which PCS-64-quadrature amplitude modulation (64-QAM) format with the tunable SE allows high and flexible throughput. A data rate of 450 Gb/s is realized at the entropy of 4.5 with the x-polarized bit error rate (BER) of 3.7 × 10^{-3} and y-polarized BER of 3.4 × 10^{-3}, both of which are lower than 7% overhead hard-decision-forward error correction (HD-FEC). The proposed scheme shows superiority in terms of data rate, rate flexibility, synchronization, etc.

Then, a rate-flexible TWDM-CPON setup is presented with a 350-Gb/s/$\lambda \sim$ 450-Gb/s/λ for a specific ONU group. The minimum rate tunable rate step is single-polarized 5 Gbps at 50 Gbaud, corresponding to an entropy step of 0.1. For monitoring the entropy/rate varies in the TWDM-CPON, for the first time, an AL-based image classifier is proposed, designed, and verified at the post-digital signal processing (DSP) of the coherent receiver after 80-km transmission. In addition, to illustrate the trade-off between classification accuracy and complexity, we compared different image classifiers based on different working principles.

I conceived the idea, performed the simulation, and experiments, collected, and processed the data, and wrote the entire manuscript. Jinsong Zhang helped me implement the experimental process. All co-authors reviewed and revised the manuscripts before submitting them to the IEEE/Optica Journal of Lightwave Technology (JLT), Optics Letters (OL), and Optical Fiber Communication Conference (OFC 2023).

Rate-flexible Pseudo-m-QAM Chaotic Physical Layer Encryption over Coherent PON (Chapter 4)

For next-generation high-capacity, rate-flexible, and secure 400-G PON, a scheme jointed wavelength division-multiplexed (WDM), entropy-regulated probabilistic constellation shaping-64-quadrature amplitude modulation (PCS-64-QAM) and chaotic encryption mapping, is proposed and demonstrated. For the first time, chaotic encryption is realized over the PCS-based PON with the architecture from one optical line terminal (OLT) to multiple optical network units (ONUs). Chaotic encryption with an initial-value-sensitive feature can generate a large amount of parallel encrypted sequences which provide a key pair corresponding with every possible entropy/rate. A novel mapping from PCS-64-QAM with various entropies to pseudo-m-QAM is designed, which erases the entropy information of the link and encrypts the original information of the sequence. The encryption transmission is demonstrated over a real-time dual-polarized coherent optical platform with an 80-km link and typically one-to-many PON configuration, and a net 211.80 $\sim$ 348.12-Gb/s rate result within the hard-decision forward error correction (FEC) threshold is achieved for $6\lambda \times 2$ ONUs group. The rate of each polarization state can be tuned in a minimum 3.408-Gbps step in the demonstration. Expanding from the basis of the original WDM-CPON, this work prepares an adapted chaotic encryption scheme for large-scale access. Overall, our proposed scheme can provide an abundant system loss budget, a large rate tunable range, and basic physical layer security for next-generation rate-flexible coherent PON (FLCS-CPON).

Then, a TDMA scheme is proposed and demonstrated on a 10-km/225.39-Gbps $\sim$ 281.62-Gbps coherent optical transmission system with a tuning step of 3.124 Gbps/pol./λ. Then, the fast NCC coefficient template matching algorithm will determine whether the entropy/rate has changed between each time slot according to the point distribution of the constellation, and further define a specific value of the entropy/rate. Finally, the entropy value extracts the initial value of the chaotic system from the codebook to further chaotically decrypt the sequence.

I conceived the idea, performed the simulation, and experiments, collected, and processed the data, and wrote the entire manuscript. Jinsong Zhang helped me implement the experimental process. All co-authors reviewed and revised the manuscripts before submitting them to the IEEE/Optica Journal of Lightwave Technology (JLT) and the Conference on Lasers and Electro-Optics (CLEO 2023).

Physical Layer Service Fairness of 200-Gbps TDM-NOMA Coherent PON (Chapter 5)

As coverage increases or network topology becomes more complex, the power budget difference between any two access points in tree-like PON is uneven, causing service fairness problems at the physical layer. The service fairness of the far-near user access in 200-Gbps coherent PON with various user cases is discussed in this work. A fairness allocation mechanism based on TDM-NOMA in the time-power domain is proposed theoretically to provide fair transmission between the arbitrary two ONUs with the best and the worst performance within single timeslots. Then, a series of subsequent experiments are demonstrated with different path loss and split ratios (SR) to prove the effectiveness and practicality of the proposed NOMA scheme, totally including 12 subcases. Any sub-experiment proves that by optimizing power allocation, the signal-to-interference noise ratio (SINR) or bit-error rate (BER) on the physical layer can be approximated to the same value. The Jain's fairness index at a fixed and flexible hard-decision forward error correction (HD-FEC) standard, and modified fairness index are used to evaluate service fairness in different cases. This TDM-NOMA scheme may address the service fairness issue in next-generation coherent PON with wide coverage.

I conceived the idea, performed the simulation, and experiments, collected, and processed the data, and wrote the entire manuscript. Jinsong Zhang helped me implement the experimental process. All co-authors reviewed and revised the manuscripts before submitting them to the IEEE/Optica Journal of Lightwave Technology (JLT).

1.4 Thesis organization

The thesis is organized and divided into 6 chapters covering an introduction, theory, simulation, demonstrations (monitoring, encryption, and access techniques), and conclusions.

In **Chapter 1**, the history and background are introduced respectively, including the development of PON, the evolutions and standards of previous several-generation PON, and the proposal of coherent PON as a candidate for future optical access architecture.

Chapter 2 is the purely theoretical part, which includes all the mathematical tools used in this thesis from signal processing to system modeling.

Then, **Chapter 3**, **Chapter 4**, and **Chapter 5** are the main parts of the thesis. Each chapter will be relatively independent but in response to a unique selected issue in coherent PON. **Chapter 3** is the joint investigation of rate-flexible coherent systems/ networks and parameter monitoring such as entropy and SNR. **Chapter 4** describes chaotic-based dynamic encryption over rate-flexible point-to-multipoint coherent PONs. **Chapter 5** begins to implement TDM NOMA to respond to the fairness issue for users with accessing far-near effect.

Chapter 6 summarizes the thesis and looks ahead to the future.

Chapter 2

Fundamental Theories in CPON

2.1 Overview

This chapter is the theoretical part, including multiple summaries of the mathematics used from **Chapter 3** to **Chapter 5**. This mathematics involved here is used in the signal processing, system modeling, and simulation of coherent optical communication systems and networks in the following various experiments, including probability constellation shaping for rate tuning, pseudo-m-mapping for dynamic encryption, and power allocation for far-near user service fairness.

2.2 Fundamentals of Coherent Detection

The principle of coherent detection is to use a beam of local oscillator light and the input signal light to mix in an optical mixer to obtain an intermediate frequency signal that changes according to the same rules as the frequency, phase, and amplitude of the signal light. Compared with traditional intensity modulation/direct detection (IM/DD), coherent detection improves reception sensitivity by detecting the difference between the local oscillator and the signal light. According to the difference in frequency values between the signal light and the local oscillator light, it can be divided into homodyne detection, heterodyne detection, and intradyne detection. Among them, homodyne detection can directly restore the baseband signal and has the highest signal-to-noise ratio.

Coherent detection has many inherent advantages. First, optical coherent receivers can use complex modulated coherent optical communications to save optical bandwidth resources and further improve fiber transmission efficiency. In the past ten years of development, coherent optical transmission has become an excellent choice to further increase transmission bandwidth. Another advantage of optical coherent receivers is having rich reconfigurable digital signal processing capabilities. In addition, the demodulation process of digital coherent receivers is completely linear. All complex amplitude information of the transmitted optical signal including the polarization state can be fully recovered after detection. Therefore, various signal compensation processes can be performed, such as chromatic dispersion compensation and polarization mode dispersion compensation.

Coherent receivers are about 20 dB more sensitive than ordinary receivers, so the distance without a relay in the transmission system will be longer. Thanks to the high sensitivity of the receiver, we can reduce the number of amplifications on the long-distance transmission optical path. In the access network, the architecture using optical coherent receiver deployment can cooperate with optical amplifiers for ultra-dense user access.

Next, several different types of optical coherent receivers will be briefly analyzed.

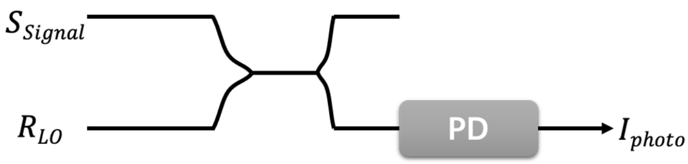

Figure 2.1: Coherent receiver based on single Photodiode (PD).

$$\begin{aligned} i_{photo} &= (S+R)(S+R)^* \\ &= (A_S e^{i\omega_S} e^{i\omega_S t} + A_R e^{i\omega_R} e^{i\omega_R t})(A_S e^{i\omega_S} e^{i\omega_S t} + A_R e^{i\omega_R} e^{i\omega_R t})^* \\ &= A_S^2 + A_R^2 + 2A_S A_R cos(\triangle\varphi + \triangle\omega t), \end{aligned} \tag{2.1}$$

Figure 2.1 shows one of the simplest coherent receivers with a single photodiode, where the latter converts the signal with a local oscillating beat frequency into a photocurrent. The photocurrent is determined by formula (2.1). Among them, A_S is the amplitude term, $\triangle\varphi+\triangle\omega t$ is the phase term, and A_R is a DC term that can be removed.

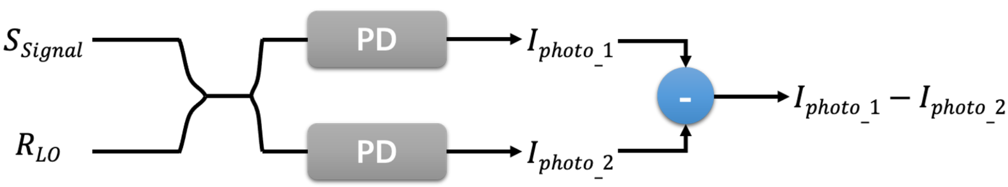

Figure 2.2: Coherent balanced receiver based on a balanced Photodiode (BPD).

$$
\begin{aligned}
i_1 - i_2 &= (S+R)(S+R)^* - (S-R)(S-R)^* \\
&= 4A_S A_R cos(\triangle\varphi + \triangle\omega t),
\end{aligned}
\tag{2.2}
$$

Evolved from Fig. 2.1, Fig. 2.2 presents a coherent balanced receiver based on a balanced Photodiode (BPD). The advantage of this design is that phase-independent terms can be eliminated.

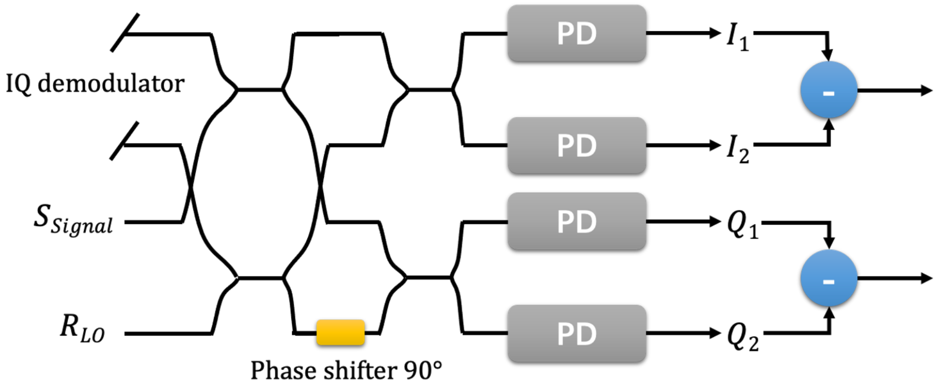

Figure 2.3: Unpolarized and multiplexed coherent optical signals detector.

$$
\begin{aligned}
I_1 - I_2 &\sim 4A_S A_R cos(\triangle\varphi + \triangle\omega t), \\
Q_1 - Q_2 &\sim 4A_S A_R cos(\triangle\varphi + \triangle\omega t),
\end{aligned}
\tag{2.3}
$$

Figure 2.3 shows a non-polarization multiplexed coherent signal receiver. This design includes orthogonal components and in-phase components under single polarization and is the most common design in single polarization receivers.

To recover amplitude and phase simultaneously, the IQ is separated into two independent output signals, so two balanced detectors are required. The local oscillator of component Q requires a phase shift of $\pi/2$. This signal is mixed only with local oscillator signal components with the same polarization state on the detector.

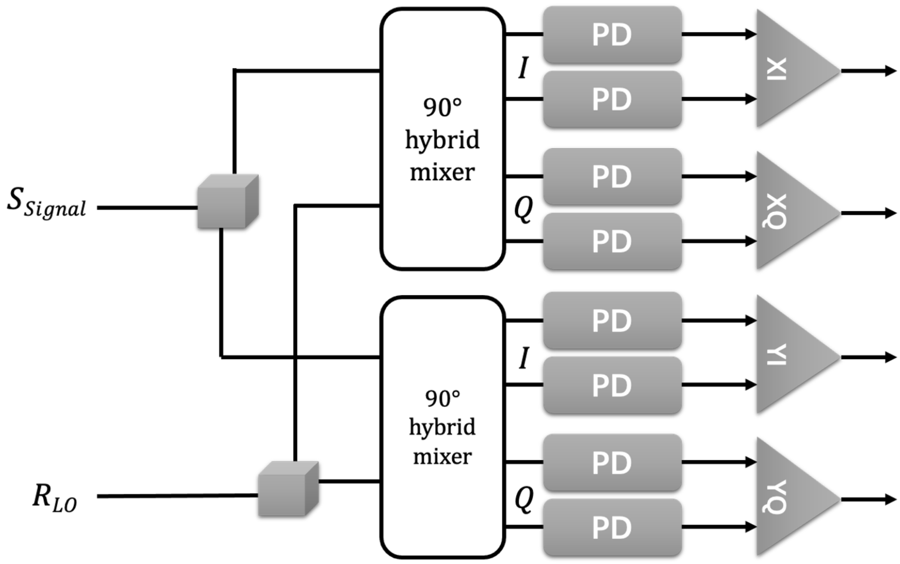

Figure 2.4: Dual-polarization coherent optical signal receiver.

$$
\begin{aligned}
XI_1 - XI_2 &\sim 4A_S A_R cos(\triangle\varphi + \triangle\omega t), \\
XQ_1 - XQ_2 &\sim 4A_S A_R sin(\triangle\varphi + \triangle\omega t), \\
YI_1 - YI_2 &\sim 4A_S A_R cos(\triangle\varphi + \triangle\omega t), \\
YQ_1 - YQ_2 &\sim 4A_S A_R sin(\triangle\varphi + \triangle\omega t),
\end{aligned}
\tag{2.4}
$$

Figure 2.4 shows a dual-polarization coherent signal receiver. This is also used in this thesis. Through the multiplexing of four channels (XI, XQ, YI, YQ), the purpose of expanding channel capacity and improving spectrum efficiency is achieved.

This design uses two IQ modulators, respectively for X polarization and Y polarization, and uses a polarization beam splitter (PBS) to separate the X and Y polarization components and beat the local oscillator light source to achieve coherent demodulation of dual polarization signals.

2.3 Fundamentals of PCS

Commonly, the Maxwell-Boltzmann distribution is applied to define the prior probabilities P_X of the M-QAM symbols $\chi = \{x_1, x_2, ..., x_M\}$ [32]:

$$P_X(x_k;\lambda) = \frac{e^{-\lambda\left|x^i\right|^2}}{\sum_{k=1}^{M} e^{-\lambda|x^i|^2}}, i = 1, 2, ...M, \tag{2.5}$$

where M is the size of the constellation and $\lambda(\lambda > 0)$ is the shaping parameter. Then the entropy of the transmitted PCS-M-QAM symbols can be expressed as:

$$H(P_X, \lambda) = -\sum_{k=1}^{M} P_X(x_k;\lambda) \log_2 P_X(x_k;\lambda), \tag{2.6}$$

For a fixed M, the entropy H is a monotonic function of λ. Specifically, when $\lambda = 0$, the constellation is equivalent to the uniform M-QAM, and the entropy H is maximized. As λ becomes larger, H decreases. Thus, we can achieve flexible-rate transmission by tuning λ. Suppose the tuning range of the entropy is

$$\Delta H(P_X) = H(P_X, \lambda_1) - H(P_X, \lambda_2) \tag{2.7}$$

Then, the line-rate range (per channel) of the tunable-rate communication system can be obtained by:

$$\Delta R = \Delta H(P_X, \lambda)B \tag{2.8}$$

where B is the baud rate of the signal with a single link.

2.3.1 Definitions of GMI and NGMI

In a practical optical communication system, binary soft-decision forward error correction (SD-FEC) codes are widely adopted, where bit-interleaved coded modulation (BICM) and bit-metric decoding (BMD) are employed. For such a scheme, the GMI and NGMI are considered effective channel metrics to predict post-FEC performance [33, 34]. The GMI can be estimated by:

$$GMI \approx \Delta H(P_X, \lambda) + \frac{1}{N}\sum_{k=1}^{N}\sum_{i=1}^{m}\log_2 \frac{\sum_{x\in\chi_{b_{k,i}}} q_{Y/X}(y/x)P_X(x)}{\sum_{x\in\chi} q_{Y/X}(y/x)P_X(x)}, \tag{2.9}$$

where $m = \log_2 M$, N is the length of the received symbol sequence, and $\chi_{b_{k,i}}$ is the symbol set containing symbols whose $i-th$ bit is $b_{k,i}$. The metric $q_{Y/X}$ is calculated as:

$$q_{Y/X}(y/x) = \frac{1}{\sqrt{2\pi\sigma^2}}e^{-\frac{|y-x|^2}{2\sigma^2}}, \tag{2.10}$$

where σ^2 is the noise variance of the AWGN channel.

While the GMI indicates the maximum number of information bits per symbol, the NGMI stands for the maximum number of information bits per transmitted bit. After the GMI is obtained, the NGMI can be calculated as:

$$NGMI = 1 - \Delta \frac{H(P_X, \lambda - GMI)}{m}. \tag{2.11}$$

2.4 Fundamentals of Chaotic Encryption

2.4.1 Entropy-aided Chaotic Encryption

Chaos encryption is a dynamic method, which is different from traditional encryption methods. At the same time, the post-encryption processing speed has nothing to do with the length of the key, and the chaotic encryption method has high computational efficiency and fast processing speed. For physical layer encryption, the chaotic encrypted information has extremely high confidentiality. The dynamic equation of the simplified Lorenz chaotic system can be expressed as follows:

$$\begin{cases} \dot{x} = a(x_2 - x_1) \\ \dot{y} = (24 - 4c)x_1 - x_1 x_3 + c x_2 \\ \dot{z} = x_1 x_2 + b x_3 \end{cases} \tag{2.12}$$

where $a = 10$, $b = 8/3$, c is the system parameter, when the system parameter c is within $c \in [-1.59, 7.75]$, the Lorenz system appears chaotic. When setting the system parameter $c = -1$, $h = 0.01$, where h is the iteration step size. The simplified Lorenz chaotic attractor phase diagram can be obtained, as shown in Fig. 2.5. The chaotic system has the characteristics of initial value sensitivity (a, b, and c), global stability, and local instability.

The chaotic system is bounded and stable in Fig. 2.5. Slightly changing the initial values of the system can make the trajectories subtly misaligned at the beginning. No matter how unstable the chaotic system is, the specific trajectory will continue to approach the attractor, making it always change within a fixed range. At the same time, the adjacent trajectories of the chaotic system are constantly repelled and separated, so the local part of the chaotic system is unstable.

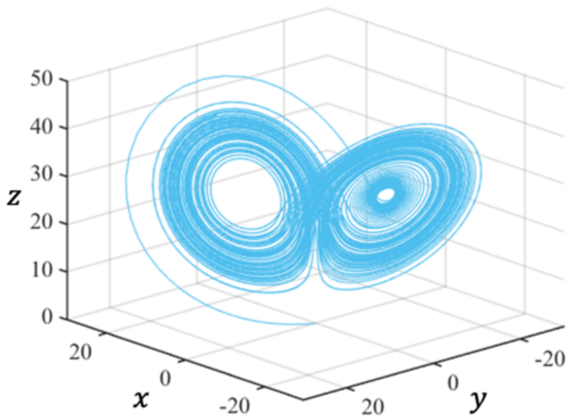

Figure 2.5: The simplified Lorenz solution of attractor x-y-z phase diagram.

When the transmitter and receiver use the same simplified Lorenz chaotic system, the drive-response synchronization Runge-Kutta algorithm can be used to solve and obtain the key. Fig. 2.6(a) shows the schematic of the classic drive-response synchronization, including the driving system ($\dot{x_1}$,$\dot{x_2}$,$\dot{x_3}$) and response system ($\dot{y_1}$,$\dot{y_2}$,$\dot{y_3}$) For a transmitting data sequence, if data is XORed twice with the same number, the original data can be recovered. Thus, if the driving and responding systems achieve synchronization and $x_1 - y_1$ are equal to a certain precision, the data can be recovered by XORing with x_1 and y_1, respectively. Here, x_1 and y_1 are the first data that comes from

Table 2.1: The codebook with different keys (initial values) and entropies.

Entropy	$\dot{x_1}/\dot{y_1}$	$\dot{x_2}/y_2\dot{3}$	$\dot{x_3}/\dot{y_3}$
3.5	0.000000001	0.000000005	0.000000002
4.0	0.000000002	0.000000006	0.000000003
4.5	0.000000003	0.000000007	0.000000004
5.0	0.000000004	0.000000008	0.000000005
5.5	0.000000005	0.000000009	0.000000006

the sequence $\dot{x_1}$ and $\dot{y_1}$, respectively. Firstly, the value of x_1 of the drive system is obtained, which is used as the key of the drive system to perform a bitwise XOR with the data to be transmitted. At the receiver, y_1 is taken from the responding system as the decryption key, and the data to be transmitted will be recovered at synchronizing status. Before synchronization, the initial values of the drive and response systems are quite different, resulting in a relatively large synchronization error value within a period. However, as the number of iterations increases, the error value of the internal state quantity of the two systems will be 0 finally.

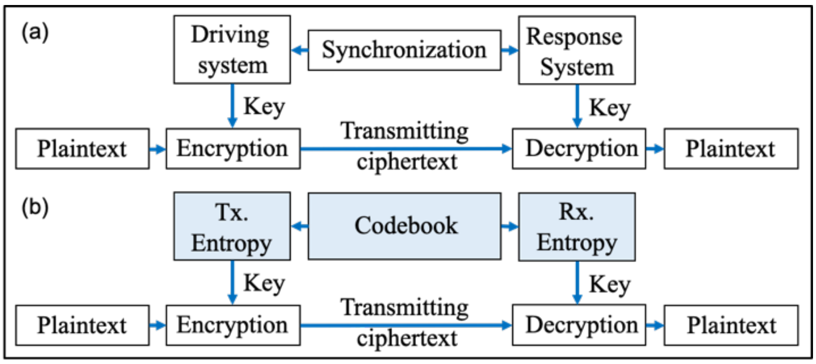

Figure 2.6: The cryptographic secure communication schematics based on (a) the synchronization system and (b) the joint entropy-initial value correspondence codebook.

Here, we modified the original drive-response system and proposed an encryption scheme by jointing entropy-initial values in a foreknown codebook. The corresponding schematic is shown and compared in Fig. 2.6(b). At the transmitter, the plaintext is encrypted through the entropy value, which corresponds to initialize values of the transmitting driving system in the codebook. After being received through the optical channel, the chaotic system's initial values are obtained by referring to the corresponding relationship between entropy and key in the codebook. In this work, an arbitrary initial value is chosen as shown in Tab. 2.1, which also presents a $> 10^{24}$ encryptable space. When the entropy is correctly identified and the data is decrypted, the errors of the three sequences are all 0 in the initial period, as shown in Fig. 2.7(a) to Fig. 2.7(c). The Lissajous-Figures from Fig. 2.7(d) to Fig. 2.7(f) of the complete synchronization state are achieved. At this time, the receiver can obtain the key through entropy, and further obtain the plaintext. Compared with the previous drive-response scheme, the entropy-based codebook scheme does not need to wait for an increase in the number of iterations. With the same entropy/initial values, the drive and response systems immediately reach a synchronized state without waiting for long synchronization. However, when the entropy-initial value correspondence from the codebook is wrong, the destination cannot obtain the plaintext, thus, protecting the transmitted information at the physical layer.

2.4.2 Implementation and Rate Definitions

To implement PCS in a practical way, probabilistic amplitude shaping (PAS) is usually used. In our setup, we simulate a 2-D PAS scheme, which is shown in Fig. 2.8. Fig. 2.8 illustrates the bit flow in the 2-D PAS schematic. The information bits are firstly split into n_{PAS} bits for shaping and n_L bits for labeling. The n_{PAS} bits are fed into the distribution matcher (DM). The DM is an essential component to realize PCS since it

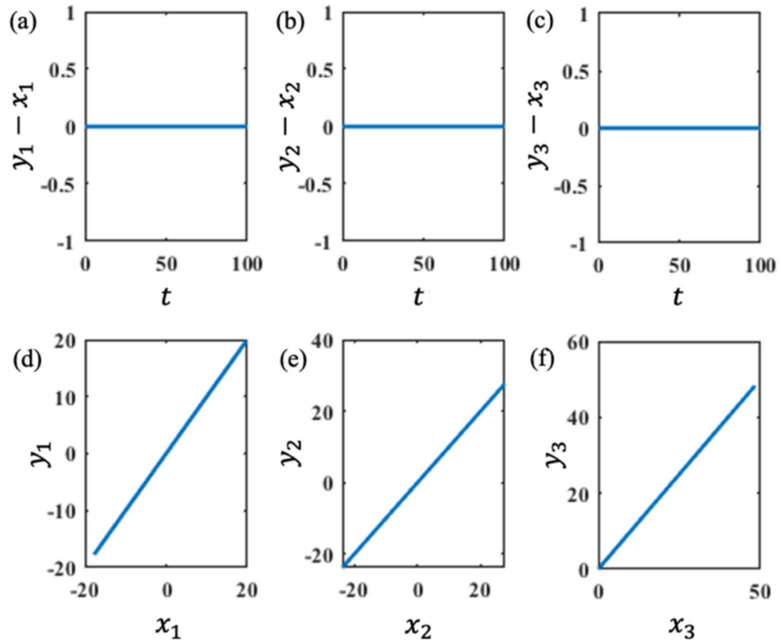

Figure 2.7: (a) (b) and (c): The error value of the internal state quantity of the transmitter and the receiver system is 0, and (d) (e) and (f): the Lissajous-Figures of the complete synchronization state are achieved.

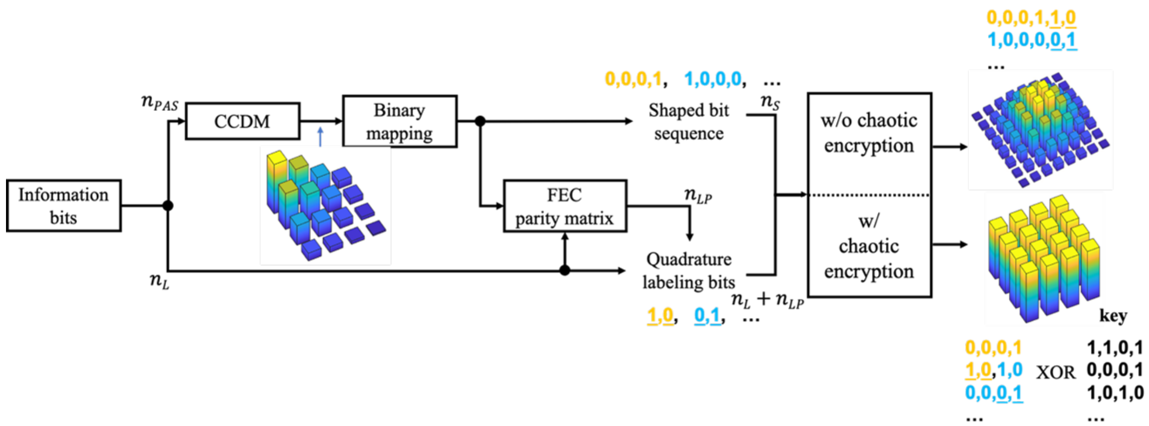

Figure 2.8: Schematic of combined PAS and encryption process. The inset figures show the probability mass function of the symbols in the corresponding stage.

converts uniformly distributed bit sequences into codewords containing symbols with a certain probability distribution. In this work, a constant composition distribution matcher (CCDM) [69] is applied. The CCDM is a fixed-to-fixed length code, and the rate loss depends on the output codeword length. To minimize the rate loss from the CCDM, the codeword length is set to 1000.

The CCDM produces probabilistically shaped symbols from n_{PAS} bits, but only within one quadrature of the PCS-64-QAM symbols, which can be regarded as shaped 16-QAM symbols as shown in Fig. 2.8. These symbols are then mapped back to n_S binary bits by standard 16-QAM demodulation. Suppose the target entropy of the CCDM is $\widehat{H}$, and the DM is ideal without any rate loss, then:

$$n_s = \frac{4n_{PAS}}{\widehat{H}}. \tag{2.13}$$

The n_S shaped bits and the n_L labeling bits are the input of the systematic FEC coding. The coding generates parity bits with the length of:

$$n_{LP} = \frac{1-R}{R}(n_s + n_l). \tag{2.14}$$

where the code rate of the FEC coding is R. The parity bits, together with the n_L labeling bits, are used to label the quadrature of the shaped symbols. For each shaped 16-QAM symbol (4 bits), 2 bits are required to indicate the quadrature. Therefore,

$$n_s = 2(n_L + n_{LP}). \tag{2.15}$$

It is inferred from Equations 2.13, 2.14, and 2.15 that:

$$\frac{n_{PAS}}{n_L} = \frac{\widehat{H}}{6R-4}. \tag{2.16}$$

which indicates the ratio between the shaping bits and the labeling bits when splitting the information bits at the beginning. Meanwhile, the ratio R_I between the information bit length and the transmitted bit length is calculated as follows:

$$R_I = \frac{n_{PAS} + n_L}{n_s + n_L + n_{LP}} = R + \frac{\overset{\frown}{H}}{6} - \frac{2}{3} = R + \frac{H}{6} - 1 \tag{2.17}$$

where the entropy of the PCS-64-QAM symbol H equals to $\overset{\frown}{H}$ $+2$, considering the two uniformly distributed labeling bits.

Although the bits before the encryption can be mapped to PCS-64-QAM symbols, after encryption, the probability distribution of the bits is changed. Consider a 4-bit sequence demodulated from a shaped 16-QAM symbol $\mathbf{b} = [b^1, b^2, b^3, b^4]$, which is a random vector with a certain joint probability distribution P. The alphabet $\mathbf{B} = \{\mathbf{b}_1, \mathbf{b}_2, ..., \mathbf{b}_{16}\}$ contains the bit sequences corresponding to the 16-QAM constellation. The distribution P_{enc} for the encryption 4-bit codes $\mathbf{b}_{enc}$ is assumed to be a discrete uniform distribution with the same alphabet as P:

$$P_{enc}(\mathbf{b}_{enc} = \mathbf{b}_n) = \frac{1}{16}, m = 1, 2, ..., 16 \tag{2.18}$$

Then the probability mass function of the sequence after the XOR operation,$\bar{b}$ is expressed as:

$$
\begin{aligned}
\bar{P}(\bar{\mathbf{b}} = \mathbf{b}_m) &= \sum_{16}^{k=1} P(\mathbf{b} = \mathbf{b}_k) P_{enc}(\mathbf{b}_{enc} = (\mathbf{b}_k \oplus \mathbf{b}_m)) \\
&= \frac{1}{16} \sum_{16}^{k=1} P(\mathbf{b} = \mathbf{b}_k) \\
&= \frac{1}{16} (m = 1, 2, ..., 16)
\end{aligned} \tag{2.19}
$$

where $\oplus$ is the bitwise exclusive or operation. One can see that the encryption process converts the shaped sequence to uniformly distributed bits. The bits can then be transmitted in the channel with any modulation format. Therefore, the scheme is named pseudo-*m*-QAM transmission, since the transmitted uniform QAM symbols contain rate-flexible information. Although this method no longer benefits from the gain stemming from the PCS, such implementation maximizes the compatibility with the conventional PAS scheme and masks the entropy information during transmission, which provides privacy and exclusivity for the ONUs.

Since the encryption and the decryption are both bitwise, the hard-decision FEC code with a 3.8 × 10^{-3} BER threshold and 7% redundancy ratio where $R = 1/(1+0.07)$, is applied in the proposed system. At the receiver, the bits are decided before the decryption, which is followed by the hard-decision FEC decoding. To achieve the threshold, pseudo-16-QAM with a baud rate of 51.12 GBaud is chosen for transmission, making the line rate 408.96 Gbps. Therefore, if we consider entropies of PCS-64-QAM ranging from 3.5 to 5.5, as demonstrated in our previous work [41], we can obtain the range of the net rates in our proposed scheme using Equation (2.17), which is 211.80 $\sim$ 348.12 Gbps.

2.5 Fundamentals of NOMA

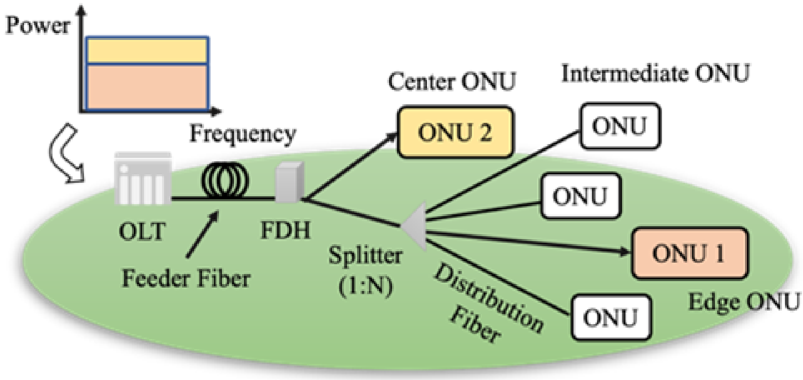

Figure 2.9: Schematic of wide-coverage TDM-NOMA coherent PON with far-near users. In the digital domain, the power factor of center ONU 2 is smaller than the power allocation for the edge ONU 2, considering the path loss and split level. FDH: Fiber distribution hub.

In this section, by establishing a digital-domain power-division TDM-NOMA system model, the constraints and evaluation criteria for downlink channels capacity and service fairness between two far-near users within the same timeslot are theoretically derived. Figure 2.9 presents a general schematic of TDM-NOMA PON with multiple access ONUs with different distances. The edge ONU is the weakest user side exhibiting the largest path loss. In contrast, the center ONU is the strongest user side with the widest power budget. Here, the time-domain QPSK signal for a specific ONU is denoted as x_i (*i*=*1*, *2*). The superimposed baseband signal x to be transmitted is

$$x = \sqrt{p_1}x_1 + \sqrt{p_2}x_2 \tag{2.20}$$

where $p_i (i = 1, 2, p_1 > p_2, p_1 + p_2 = p = 1)$ is the normalized power allocation factor for two far-near ONUs. The normalized transmit power is 1. After transmitted power normalization, the PAR between two users, β , is defined as

$$\beta = \frac{p_1}{p_2}. \tag{2.21}$$

In this work, the values of β are selected from 2 to 9 for evaluating the experimental setup performance. At the ONU side receiver, the receiving signal $y_i (i = 1, 2)$ with normalized power can be expressed as

$$y_i = h_i \otimes x\Lambda_i + N_i = F^{-1} H_i x \Lambda_i + w_i, \tag{2.22}$$

where h_i and H_i are the temporal and frequency response of the superimposed baseband signal, Λ_i is the phase rotation matrix caused by phase noise, $F(F^{-1}))$ denotes the inverse Fast Fourier Transform (IFFT), and N_i and w_i is the frequency format and temporal format of additive white Gaussian noise (AWGN), $\otimes$ is the convolution symbol, respectively. Hence, for the two far-near transmission channels, the receiving signal of far-edge ONU 1 is

$$y_1 = F^{-1} H_1 \sqrt{p_1} x_1 \Lambda_1 + F^{-1} H_1 \sqrt{p_2} x_2 \Lambda_1 + w_{0,1}, \tag{2.23}$$

and the receiving signal of the near center ONU 2 is

$$y_2 = F^{-1} H_2 \sqrt{p_1} x_1 \Lambda_2 + F^{-1} H_2 \sqrt{p_2} x_2 \Lambda_2 + w_{0,2}, \tag{2.24}$$

At the DSP of the receiver ONU side, signal operations including dispersion compensation, channel equalization, and phase noise removal will be performed, and the overall profile of h_i can be known through channel estimation. Therefore, the recovery signal can be expressed as

$$\begin{aligned} x_i &= (H_i^T H_i)^{-1} H_i^T F y_i \Lambda_i^{-1} \\ &= (H_i^T H_i)^{-1} H_i^T F (F^{-1} H_i x \Lambda_i + w_i) \Lambda_i^{-1} \\ &= \sqrt{p_1} x_1 + \sqrt{p_2} x_2 + (H_i^T H_i)^{-1} H_i^T F w_i \Lambda_i^{-1} \\ &= \sqrt{p_1} x_1 + \sqrt{p_2} x_2 + k w_i \Lambda_i^{-1}. \end{aligned} \tag{2.25}$$

Next, according to Shannon's theorem, we can modify and obtain the channel capacity C_1 of the far edge ONU 1 with strong power allocation, which is approximated as

$$C_1 = B \log_2 \left(1 + \frac{p_1 |h_1|^2}{p_2 |h_1|^2 + N_{0,1}} \right), \tag{2.26}$$

where the item of $\xi_1 = \frac{p_1|h_1|^2}{p_2|h_1|^2+N_{0,1}}$ is the signal-to-interference plus noise ratio (SINR) of the far ONU 1. B is the system bandwidth. For point-to-multiple point architecture, assuming that the value of bandwidth is not decreased by the increasing of the transmission distance. While for the near ONU 2, the channel capacity of the weak user side without SIC is approximated as

$$C_{1,2} = B \log_2 \left(1 + \frac{p_2 |h_2|^2}{p_1 |h_2|^2 + N_{0,2}} \right), \tag{2.27}$$

where the item of $\xi_2 = \frac{p_2|h_2|^2}{p_1|h_2|^2+N_{0,2}}$ is the SINR of the near ONU 2. Assuming that perfect SIC can be achieved, the transmission information of ONU 1 is subtracted from the total information frame, and the corresponding pure channel capacity is approximated as

$$C_{1,2} = B\log_2\left(1 + \frac{p_2\left|h_2\right|^2}{N_{0,2}}\right), \tag{2.28}$$

If two ONUs are on the same layer without far-near effect, the users have similar distances and pass through the same amount of optical passive splitter with the same SR. Then $h_1 \approx h_2$ and $N_{0,1} \approx N_{0,2}$. Hence, the sum channel capacity can be obtained from the following derivation, which is approximated as

$$\begin{aligned} C_{SUM} &= B\log_2\left(1 + \frac{p_1\left|h_1\right|^2}{p_2\left|h_1\right|^2 + N_{0,1}}\right) + B\log_2\left(1 + \frac{p_2\left|h_2\right|^2}{N_{0,2}}\right) \\ &= B\log_2\left(1 + \frac{p_1\left|h_1\right|^2}{p_2\left|h_1\right|^2 + N_{0,1}}\right) + B\log_2\left(1 + \frac{p_2\left|h_1\right|^2}{N_{0,1}}\right) \\ &= B\log_2(1 + \frac{(p_1\left|h_1\right|^2 + p_2\left|h_1\right|^2)(p_2\left|h_1\right|^2 + N_{0,1})}{N_{0,1}(p_2\left|h_1\right|^2 + N_{0,1})}) \\ &= B\log_2(1 + \frac{p\left|h_1\right|^2}{N_{0,1}}) \end{aligned} \tag{2.29}$$

where the formula still satisfies the channel capacity relation of Shannon's theorem. To achieve service fairness between the edge ONU 1 and center ONU 2 at a certain power budget and with ROP difference, we chose to evaluate two fairness indexes from two perspectives. Experimentally, on the one hand, we allocate the two different power factors so that the relative power gain of the signal to remote ONU 1 can compensate for the path loss and division loss. The fairness of the service is demonstrated by comparing the fairness coefficient improvement of the same net rate under a specific FEC threshold. According to the fairness model proposed by Lei *et al.* in [37], we can use Jain's fairness index J to evaluate the fairness of the proposed multi-user system, which is

$$J_R = \frac{(\sum_{m=1}^{M} R_m)^2}{M \sum_{m=1}^{M} R_m^2}, \tag{2.30}$$

where R_m is the actual throughput rate of the m^{th} user and m represents the total number of users in a specific area. However, in the rate-fixed PON system, the modulation format with a specific data rate is fixed resulting in the inability to compare rates directly, unlike in the rate-flexible PON case.

On the other hand, theoretically, the optimal object between two far-near users can also be transformed as

$$\min_{p_1, p_2} f(p_1, p_2) = |\xi_1 - \xi_2| = \left| \frac{p_1 |h_1|^2}{p_2 |h_1|^2 + N_{0,1}} - \frac{p_2 |h_2|^2}{p_1 |h_2|^2 + N_{0,2}} \right| \tag{2.31}$$

which is restricted by the following conditions of

$$\begin{cases} \forall p_1, p_2 \in [0.1] \\ \quad p_1 > p_2 \\ p_1 + p_2 = p = 1 \end{cases} \tag{2.32}$$

Therefore, by adopting the power-division NOMA scheme and adjusting the PAR β at the DSP of OLT side, the SINRs of two far-near ONUs can be optimized to the nearest considering the link loss, which further ensures closer service performances.

A modification should be performed which replace R_m of the m^{th} user with the approximately achievable channel capacity C_m. The premise is to perform substitution and comparison under perfect SIC. We have a new modified fairness index J which is approximated as

$$J_C = \frac{(\sum_{m=1}^{M} C_m)^2}{M \sum_{m=1}^{M} C_m^2} \tag{2.33}$$

In the following PON demonstration, the fixed QPSK format is adopted and assigned to two far-near ONUs without changing the baud rate. However, with the increase of the power factor ratio, the improvement of service quality for the far ONU 1 is represented by the increase of SINR or the decrease of BER. According to formulas 2.26 and 2.28, the service fairness of OLT to multiple ONUs can be further compared. The following proposed and demonstrated coherent system only exists between two far-near ONUs. Therefore, for this two-user PON system, the above-modified fairness index, Eq. (2.33), can be approximated as:

$$J_{C,2} = \frac{(C_1 + C_{1,2})^2}{2(C_1^2 + C_{1,2}^2)} \tag{2.34}$$

where C_1 and C_2 are the achievable channel capacities of the edge ONU 1 and center ONU 2, respectively. We will select several power allocation factor combinations, and adopt the Equation 2.34 to evaluate the increase of service fairness of the far-near PON system under different path loss, SR, and the PAR.

2.6 Section Summary

This section summarizes the mathematics used in the following sections.

Chapter 3

Parameter Monitoring in CPON

3.1 Overview and Research Status

Two-dimensional constellation shaping technologies, such as probabilistic constellation shaping (PCS) [70], geometric constellation shaping (GCS) [71], and hybrid probabilistic geometric constellation shaping (HPGCS), are proposed to provide asymptotic gain which makes the information amount of reliable optical transmission closer to the theoretical capacity of Shannon's limit [35]. Considering the time-space complexity of DSP, since the relative positions of the constellation points remain the same, PCS is compatible with current algorithms and systems and is advanced for practical cost-efficient optical systems compared to GCS and HPGCS. In addition, PCS with tunable spectral efficiency characteristics provides a possibility for realizing higher throughput and more flexible rate regulation [72]. Compared with the previous scheme to implement rate adaptation by adjusting bandwidth/ spectrum resources, a new tuning dimension is provided [51][53]. At present, PCS has been widely applied and implemented in optical communication and networking, combined with staircase codes [73], turbo codes [74], and four-dimension (4D) coded modulation [75]. Joint PCS high-order modulation with dense constellation distribution increases the capacity but also becomes more vulnerable to channel distortion. However, for PCS-based optical link monitoring including rate and performance, no monitoring program has been proposed so far.

In most modulation formats including M-level pulse amplitude modulation (M-PAM) or M-order quadrature amplitude modulation (M-QAM), a change in the number of levels or orders can be easily observed. Compared with those general mapping schemes, the distribution changes in PCS are more imperceptible. However, the generation of constellation diagrams gives a bridge, which enables us to introduce some general computer vision (CV) methods into optical communication systems for entropy and performance monitoring. For traditional modulation formats such as quadrature phase shift keying (QPSK), and 8/16/32/64-QAM, some numerical solutions are used to identify the modulation format [76]. These methods have been widely reported for monitoring coherent optical transmissions [77][78]. Typical machine learning (ML) schemes such as support vector machines (SVMs) are also introduced as a route to simultaneously classify modulation formats and monitor the optical signal-to-noise ratio (OSNR) [79]. Q. Zhang *et al.* designed a bit error rate (BER) estimation scheme based on a K-means clustering-assisted Gaussian approach (GA) covering arbitrary modulation formats [80]. Subsequently, both the convolution neural network (CNN)-based deep learning (DL) technique and the k-nearest neighbor (KNN) algorithm were used to perform standard M-PAM or M-QAM modulation format identification and optical signal-to-noise ratio (OSNR) monitoring, simultaneously [81][82]. Recently, a series of pattern recognition algorithms based on DL have been widely mentioned and applied in coherent optical communication systems, or intensity-modulated direct detection (IM/DD) communication systems [83][84]. These methods have achieved great success, but often require a large amount of data to train the neural network. Hence, there are great requirements for the computing power of the processor as well as the challenge of power consumption. Active learning (AL), as a small-sample learning method, and data augmentation (DA) are the two key technologies we adopt. The goal is to obtain the highest possible recognition accuracy with the smallest possible available sample size and lowest power consumption [85][84].

In this work, we first propose an AL-aided entropy-tunable automatic modulation identification (AL-aided ET-AMI) scheme based on CNN for a PCS-64-QAM coherent optical communication system. The automatic transmission rate/ capacity regulation is achieved by tuning the value of signal entropy. A 350 $\sim$ 550-Gbps (at the entropies from 3.5 to 5.5) dual-polarized coherent optical transmission is experimentally demonstrated over a 10-km SSMF link. The generalized mutual information (GMI) and normalized generalized mutual information (NGMI) are calculated and presented at various entropy and received optical power (ROP). The change interval of entropy is 0.5 or 0.1 at the ROP of -8 dBm. The change interval of SNR is divided into 1 dB by using the nearest neighbor correspondence at the entropy of 4.5 with the ROP varying from -8 dBm to -27 dBm. When the entropy tuning accuracy is 0.5, corresponding to a rate tuning step of 25 Gbps, the recognition accuracy of AL-aided ET-AMI is 100%

without DA. When the entropy tuning accuracy is 0.1 (rate tuning step of 5 Gbps), the recognition accuracy is still around 95% and can be further improved to 99% by DA. This indicates that our proposed scheme can distinguish a rate tuning step as small as 5 Gbps at 50 GBaud. For the SNR change of 1 dB, the monitoring recognition accuracy is 87% with or without DA with 400 training samples. The three recognition experiments have consistently proved that the AL-aided AMI scheme has a good monitoring performance in rate-flexible PCS-based coherent optical communication systems.

3.2 AL-aided AMI principle and data pre-processing

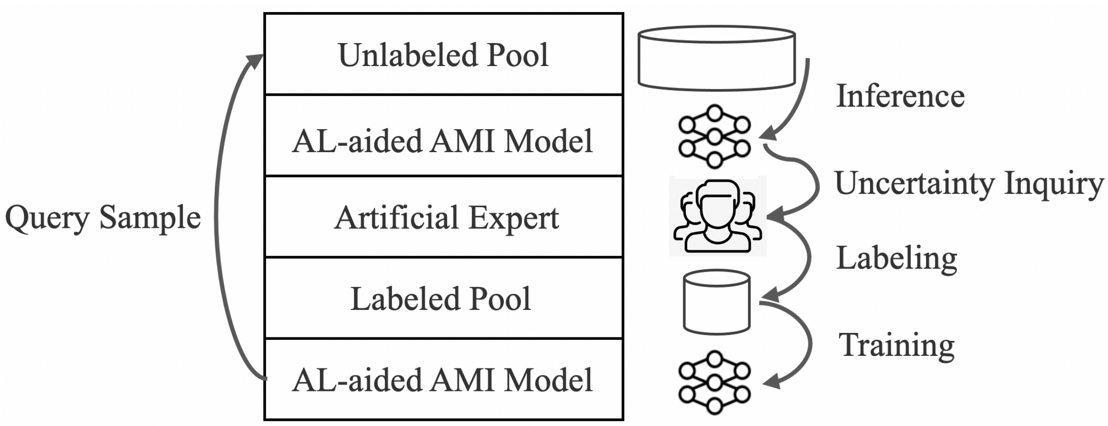

Figure 3.1: The flow chart of the proposed AL-aided AMI scheme.

Figure 1 shows the flowchart of the proposed AL framework, which includes an unlabeled pool, AL-aided AMI model, artificial expert, and labeled pool. The pool mainly contains all the collected PCS constellation diagrams with different entropy. At each training circle, AL queries the most useful unlabeled samples through uncertainty sampling, assigns the selected unlabeled samples to experts for labeling, and then uses the queried samples to train a specific neural network model to improve its classification accuracy. Compared with traditional CNN-based image classifiers, AL improves and accelerates the convergence process of the recognizer through the query sample process. Here, we abstract the problem into a pool-based AL classification model with 5 categories. The based CNN model is AlexNet which can be divided into 5 convolutional layers, 3 fully-connected layers, and 1 SoftMax layer, with 5 output interfaces. The number of outputs of the last layer can be flexibly adjusted according to the type of modulation format or entropy number identified. Therefore, AlexNet is used for contour stellar image feature extraction, while AL is used to reduce the size of the training dataset.

A batch of unlabeled samples is identified each time the entire pending dataset is tested and sorted according to the uncertainty. Then, by adopting margin sampling as the strategy of uncertainty sampling, for the most confusing samples, manual interrogation can annotate samples. The margin sampling can be expressed as follows:

$$s_M^* = arg\min_s \left(P_\theta \left(\frac{\widehat{h_1}}{s} \right) - P_\theta \left(\frac{\widehat{h_2}}{s} \right) \right), \tag{3.1}$$

where $\widehat{h_1}$ and $\widehat{h_1}$ are the first and second most probable entropy labels, which are predicted and ranked by AlexNet. s is a specific sample from the unlabeled samples poor and s_M^* is the most uncertain sample selected from the unlabeled pool. The sample with the smallest difference between the largest predicted probability and the second-largest predicted probability by the model is selected as the hard sample. In each AL round of training, 40 samples are selected and added to the data to be trained for further training of the AlexNet model. Therefore, the size of training samples and verification samples in each round increases gradually from 40 to 400.

DA is mainly used to maintain the relatively high robustness of the ET-AMI algorithm especially in the presence of phase noise, frequency offset, gain compression, and IQ imbalance. DA based on basic image manipulations is a common approach used in DL frameworks to augment training datasets. The underlying representations of the dataset consisting of contour stellar images are relatively well observed and separated. Here, the original constellation diagram is first converted to a contour stellar image. Then, as shown in Fig. 3.2, the rotation transformation of the converted contour stellar image is adopted randomly between 0° and 180° to further increase the number of training samples. As a method to expand the scale of the input image, DA does not increase the types of training samples but increases the input of multiple behavior patterns for each type. Here, the constellation diagram with a specific entropy value will be increased to 25 inputs.

3.3 Experimental Setup

The schematic of DSP flow and coherent optical system setup is shown in Fig. 3.3, mainly including the transmitter (Tx.) DSP, coherent optical communication loop, receiver (Rx.) DSP, and the recognition and processing of constellation images. The DSP of the transmission part is performed in real time, but the DSP of image processing is executed offline. At the transmitter, pseudo-random binary sequences (PRBS) are first generated and mapped in PCS-64-QAM formats. Then, the sequences are

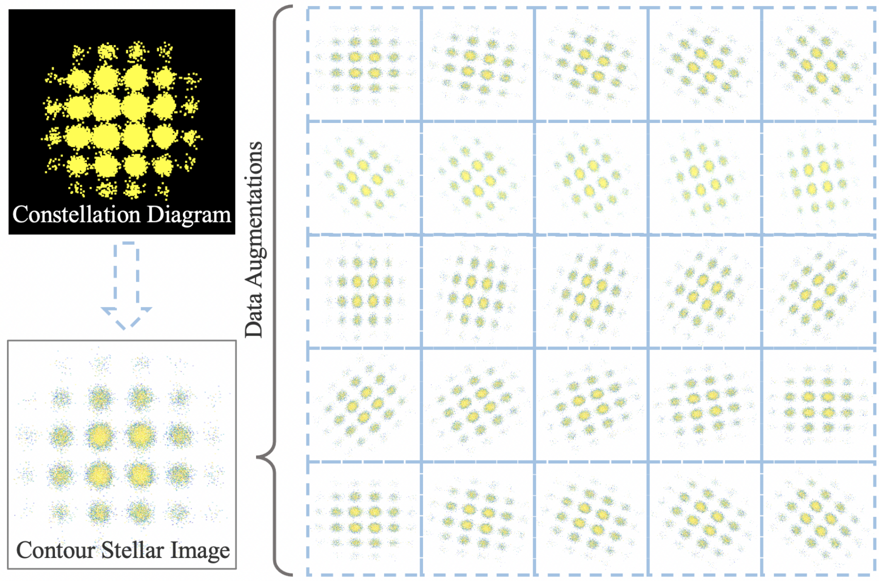

Figure 3.2: Dataset preparation: Converting the constellation diagram to contour stellar image and DA.

Table 3.1: The experimental setup parameters.

Parameter	Value
Operating wavelength	1548 nm
Launch optical power	0 dBm
Transmission distance	10 km
Baudrate	50 GBaud
Roll-off factor	0.1
RCC frequency range	[-27.5 GHz, 27.5 GHz]
RCC length	51 taps
Polarization state	2
Channel	4

up-sampled and shaped by a designed root-raised-cosine (RRC) pulse filter. In addition, pre-emphasis is used to compensate for channel impairments. The pre-emphasis function is done automatically and internally by the transmission equipment. Here, the transmission setup is a typical 4-channel system with IQ and XY. Four transmitted sequences are input into the digital-to-analog converter (DAC) and then modulated by the input light with a dual-polarized IQ modulator (DP-IQM). The experimental

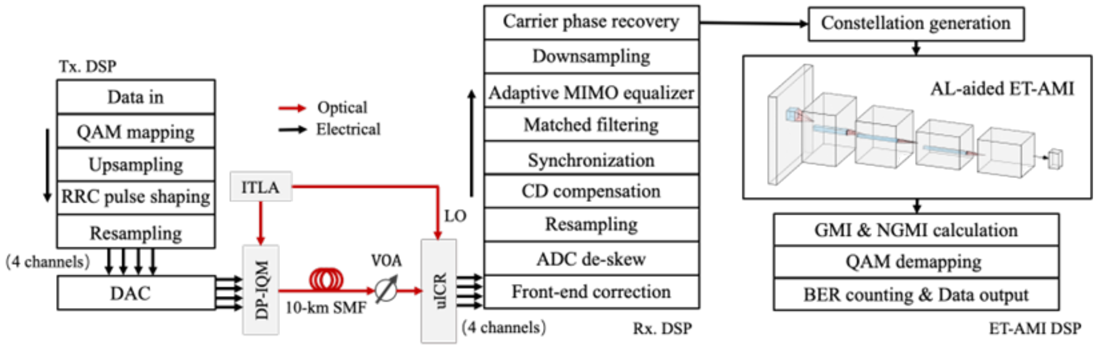

Figure 3.3: The DSP flow of AL-aided ET-AMI and the system architecture of PCS-based coherent optical system over a 10-km SSMF.

verification is performed over a coherent optical transmission platform with a 10-km standard single-mode fiber (SSMF). The integrated tunable laser assembly (ITLA) serves as the transmission light source and the local oscillator (LO) at the receiver, simultaneously, which avoids the problem of frequency offset. At the receiver side, a variable optical attenuator (VOA) is used to adjust the ROP for further variation of SNR identification experiments. Then, a micro-integrated coherent receiver (λ ICR) is adopted to capture and save the 4-channel receiving sequences, which is a typical coherent detection structure including pair polarized beam splitters (PBSs), 90° optical hybrid operator, balance photodetectors (BPDs), electric amplifiers (EAs) and analog-to-digital converter (ADC). Next, the Rx. DSP processes the received sequences of the 4-channels acquisitions in parallel. Front-end correction and ADC de-skew are performed first. Then, the sequences are resampled and the chromatic dispersion (CD) is compensated. Adaptive multiple-input multiple-output (MIMO) equalization is performed after synchronization and matched filtering. Here, the adaptive MIMO equalizer uses radius-directed equalization (RDE) and operates under 2 samples per symbol with a length of 15 taps. To ensure convergence, 2048 QPSK pilot symbols are inserted before the information sequence for pre-convergence by constant modulus algorithm (CMA). The optimal learning rate depends on the entropy of the transmitted signal. Before entering the digital imaging processing part, downsampling, phase carrier recovery, and constellation diagrams generation are executed in sequence accordingly. Finally, after the GMI and NGMI calculation, the sequences are demapped and the BERs are also counted. Tab. 3.1 presents the specific values of experimental coherent setup parameters.

For the ET-AMI experiment based on the CNN model, the dataset is prepared without considering the hard-decision FEC threshold (HD-FEC). Constellation diagrams for all states are captured with different entropy values at different SNRs. For some signals with relatively high entropy, reaching a BER below the hard-decision FEC threshold requires a higher SNR, which the system cannot achieve. Therefore, for the collected constellation diagrams for the ET-AMI dataset, some are in a case of link BER overload (BER $>$ 3.8×10-3). In addition, in the following communication and identification experiments, the results of the x-polarization component and the y-polarization component are separated. This is to obtain double the amount of data in one experiment. In practical dual-polarized IQ coherent optical communication systems, the two polarization components are usually evaluated together and generate an independent constellation diagram. On the other hand, compared with a practical coherent transmission system, we modified several hardware configurations to adapt the identification experiment. The first modified configuration is the ITLA provides both Tx. carrier and Rx. LO in the optical communication loop. Then, the transmission distance is 10 km with a VOA to adjust the ROP in the mentioned experimental setup, which may contradict the coherent optical architecture to support long-distance cognition. These hardware configuration changes are only to better demonstrate the effect of entropy/rate tuning and to better prepare and present the ET-AMI experimental dataset.

3.4 Results and Discussions

This section contains the experiment results and discussions. The input characterizations and the classification accuracy of AL-aided ET-AMI will be comprehensively presented, analyzed, and discussed in this section.

3.4.1 Characterization of basic input sequences

The coherent optical communication platform is used for transmitting data over x-polarized in-phase, x-polarized quadrature, y-polarized in-phase, and y-polarized quadrature (XI, XQ, YI, and YQ) channels in parallel. Fig. 3.4 and Fig. 3.5 show the characteristics of input 4-channel sequences characteristics which mainly include the double-side spectra and cumulative distribution histogram. The input profiles of the sequence of four channels almost completely coincide with the entropy of 4.5 at the baud rate of 50 GBaud. The 3-dB signal bandwidth shown in Fig. 4 is 50 GHz, ranging from -25 GHz to 25 GHz. The input probability distribution density can also be calculated from the cumulative distribution density in Fig. 3.5.

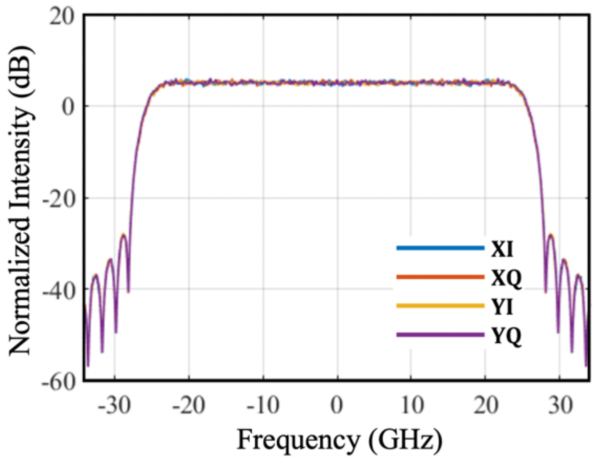

Figure 3.4: The double-side spectra of the input 4 real-value channels (XI, XQ, YI, and YQ) with the entropy of 4.5 at the baud rate of 50 GBaud.

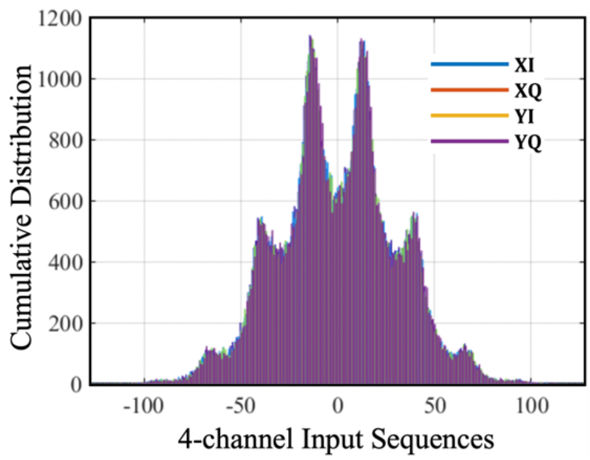

Figure 3.5: The input cumulative distribution histogram of the input 4 real-value channels (XI, XQ, YI, and YQ) with the entropy of 4.5.

3.4.2 Characterization of ET-AMI with tunable entropy

The experiment for the identification of tunable entropy is divided into two parts: the tuning step size of 0.5 and the tuning step size of 0.1 in terms of the entropy, corresponding to the tuning step sizes of the rate being 25 × 2 Gbps and 5 × 2 Gbps. In the experiment, the entropy of each transmitting frame is adjusted at the Tx. DSP. However, we envision that in a practical full-duplex symmetric optical communica-

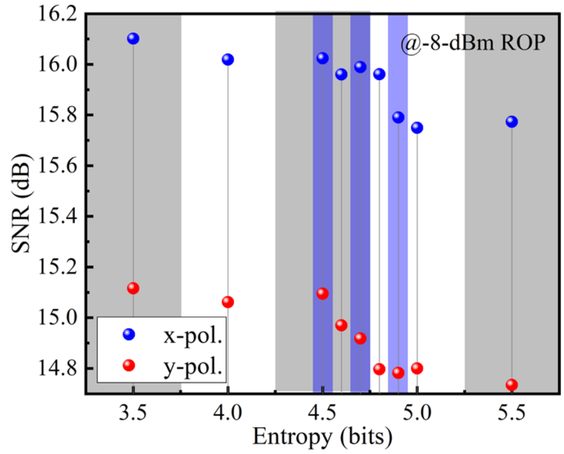

Figure 3.6: The SNR distribution of x-pol. and y-pol. of the dual-polarized coherent optical system with the entropy varying from 3.5 to 5.5 (interval 0.5) and varying from 4.5 to 4.9 (interval 0.1).

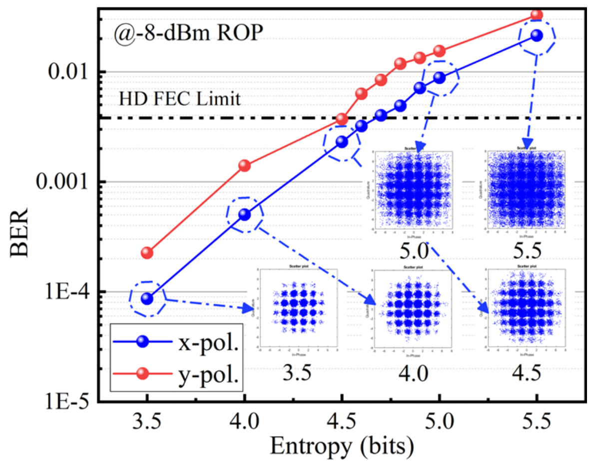

Figure 3.7: The BERs of x-pol. and y-pol. of the dual-polarized coherent optical system with the entropy varying from 3.5 to 5.5 (interval 0.5) and varying from 4.5 to 4.9 (interval 0.1). (Inset: the constellation diagrams of x-pol. at the entropy of 3.5, 4.0, 4.5, 5.0, and 5.5, respectively.)

tion link, the entropy/rate of downlink is adjusted according to the feedback of uplink from the terminal/user side. In the communication part, the interval of 0.5 is from the entropy of 3.5 to the entropy of 5.5, while the interval of 0.1 is from the entropy of 4.5 to the entropy of 4.9. The interval of 0.1 is the adjustable minimum step size in our current setup. Fig. 3.6 shows the SNR distribution of the x-polarized and y-polarized branches. The communication performance of the x-polarized component is slightly better than the y-polarized component inside the designed coherent optical system. The SNR does not change drastically as the entropy changes, despite the fact that the PCS technique may bring a larger peak-to-average power ratio (PAPR) to the transmitted signals when reducing the entropy. It can be inferred that the system in our experiment is limited by the average power rather than the peak power. For the x-polarized branch, at the ROP of -8 dBm, the SNR is 16.10 dB at the entropy of 3.5, which gradually decreases to 15.77 dB at the entropy of 5.5. While for the y-polarized component, due to a worse channel status, the SNRs are 15.12 dB and 14.73 dB at the entropies of 3.5 and 5.5, respectively. The slight change of SNR may be caused by imperfect receiver DSP that does not completely recover the signal at high entropy values. Nevertheless, the influence of such small SNR differences on the constellation generation is negligible. Then, the BERs are measured at the same ROP of -8 dBm. The polarization-dependent loss (PDL) here is close to $\sim$1 dB between the x-polarized component and the y-polarized component, which is due to some inherent defects of the optical components or the connection.

Figure. 3.7 presents the corresponding BER of the x-polarized and y-polarized branches, and the inset figures also show the PCS-64-QAM constellation diagrams of the x-component at the entropies of 3.5, 4.0, 4.5, 5.0, and 5.5, respectively. As the entropy increases from 3.5 to 5.5, the BER increases, and the constellation diagram gradually becomes larger and blurrier. When the entropy is lower than or equal to 4.5, the BERs of the x-component are $\leq 2.3 \times 10^{-3}$ which is lower than the HD-FEC threshold of 3.8 × 10^{-3}, while the BER of the y-component is $\leq$ 3.7 × 10^{-3} which is slightly lower than the HD-FEC threshold. Therefore, as we have shown in Fig. 3.7, only with the entropies of 3.5, 4, and 4.5, the BER reach below the HD-FEC threshold of 3.8 × 10^{-3}, corresponding to net rates of 327.1 Gb/s, 373.8 Gb/s, 420.5 Gb/s. For entropies of 5 and 5.5, it is mentioned in our manuscript that a lower baud rate is needed to achieve BERs lower than the HD-FEC threshold of 3.8 × 10^{-3}.

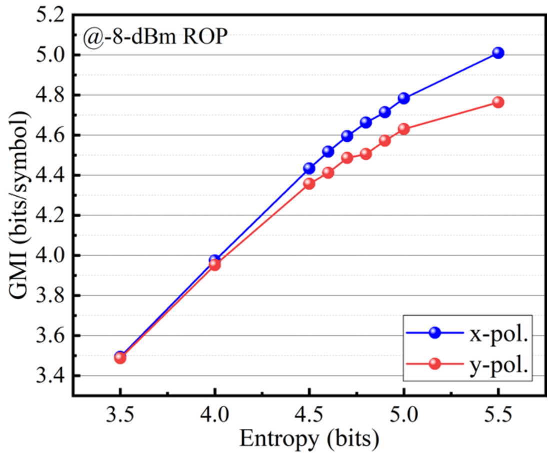

Figure 3.8: The GMIs of x-pol. and y-pol. of the dual-polarized coherent optical system with the entropy varying from 3.5 to 5.5 (interval 0.5) and varying from 4.5 to 4.9 (interval 0.1).

Figure. 3.8 and Fig. 3.9 show the GMI and NGMI of the x-polarized and y-polarized branch as the entropy varying from 3.5 to 5.5 over the proposed coherent optical system, respectively. As the entropy increases from 3.5 to 5.5, the GMI increases but the corresponding NGMI decreases. At the entropy of 3.5, the GMI and NGMI of the x-polarized component are 3.4932 bits/symbol and 0.9992, respectively. While at the entropy of 5.5 the GMI and NGMI of the x-polarized component, the GMI increases to 5.0094 bits/symbol, and the NGMI decreases to 0.9181. For a more specific data presentation of the coherent system, Tab. 3.2 shows the numerical values and im-

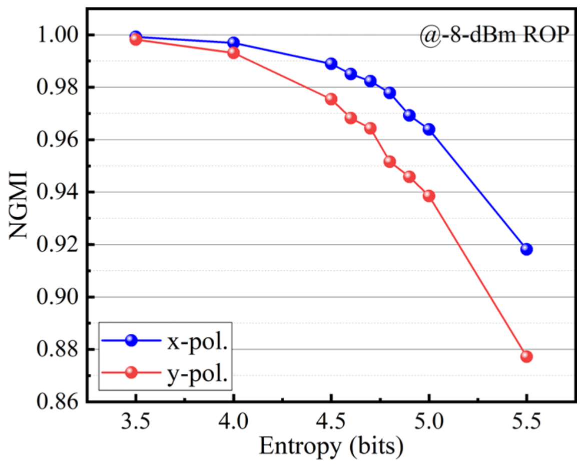

Figure 3.9: The corresponding NGMIs of x-pol. and y-pol. of the dual-polarized coherent optical system with the entropy varying from 3.5 to 5.5 (interval 0.5) and varying from 4.5 to 4.9 (interval 0.1).

Table 3.2: The performance comparison when entropy is changed at 0.5 intervals and -8 dBm ROP.

	Entropy	**3.5**	**4.0**	**4.5**	**5.0**	**5.5**
x-pol.	SNR	16.10	16.01	16.02	15.75	15.77
	GMI	3.49	3.97	4.43	4.78	5.01
y-pol.	SNR	15.12	15.06	15.09	14.80	14.73
	GMI	3.49	3.95	4.36	4.63	4.76

age information, including SNRs, GMIs, and contour stellar images at an interval of 0.5 of the x-component and the y-component, respectively. Tab. 3.3 presents similar information to Tab. 3.2, but the entropy ranges from 4.5 to 4.9 with an interval of 0.1. It can be observed that when the interval of the tunable entropy is 0.5, the contour stellar images captured by the coherent optical system can still be distinguished even by the naked eye. However, when the change interval of tunable entropy is 0.1, the contour stellar images are difficult to distinguish. The introduction of the CV-based method is to help detect the entropy/ rate, SNR, and other communication performance changes of the coherent transmission system in the case of more slightly tuned entropy.

Table 3.3: The performance comparison when entropy is changed at 0.1 intervals and -8 dBm ROP.

	Entropy	4.5	4.6	4.7	4.8	4.9
x-pol.	SNR	16.02	15.96	15.99	15.96	15.79
	GMI	4.43	4.52	4.59	4.66	4.71
y-pol.	SNR	15.09	14.87	14.92	14.70	14.78
	GMI	4.36	4.41	4.49	4.51	4.57

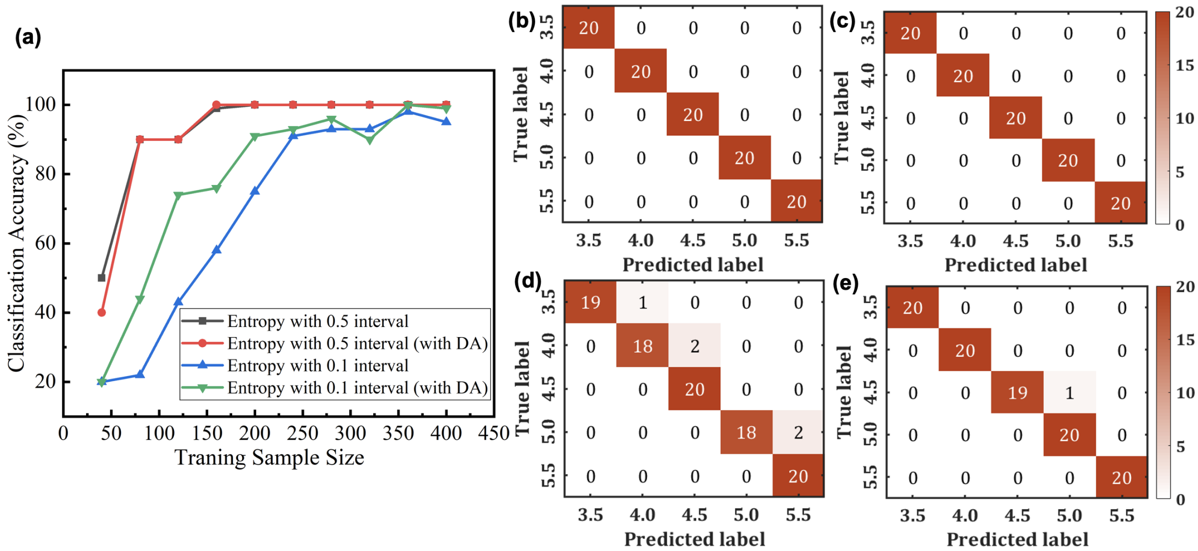

Figure 3.10: (a) Comparison of classification accuracy of ET-AMI scheme for tunable entropy changing in an interval of 0.5 and 0.1, respectively. Under 400 training sample size, the confusion matrices of the ET-AMI scheme at the entropy changing with an interval of 0.5 (b) without DA and (c) with DA; at the entropy changing with an interval of 0.1 (d) without DA and (e) with DA.

The classification accuracy of ET-AMI schemes and the corresponding confusion matrices are present in Fig. 3.10. When the change interval of entropy is 0.5, as shown in Fig. 3.10(a), the proposed ET-AMI scheme can easily achieve $>$ 99% recognition accuracy with a small sample size. These results can be well achieved with or without DA, over a training sample pool with a size as small as 160. The trend of the curve is consistent with the convergence trend with and without DA. The confusion matrices of the ET-AMI scheme at the entropy with a tuning step of 0.5 show superior performance at 100% classification accuracy at a 400 training sample size, as shown in Fig. 3.10(b) and Fig. 3.10(c). For the change interval of entropy of 0.1, the proposed ET-AMI scheme can reach 95% recognition accuracy, the result can be improved to 99% with DA with a training sample pool with size 400. The corresponding confusion matrices with and without DA are also presented in Fig. 3.10(d) and Fig. 3.10(e).

3.4.3 Characterization of AMI with changing SNR

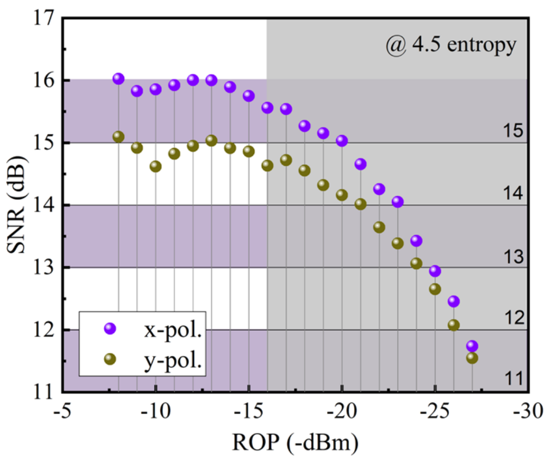

Figure 3.11: The SNR distribution of x-pol. and y-pol. of the dual-polarized coherent optical system at the entropy of 4.5 with the ROP varying from -8 dBm to -27 dBm.

Furthermore, the AMI model can also be used for channel SNR monitoring while transmitting PCS-64-QAM modulation formats. For this proposal, an experiment is further designed and demonstrated at the same entropy of 4.5 with various ROPs. We first measured and compared the SNR and BER of the x-component and the y-component at 50 GBaud, respectively, as shown in Fig. 3.11 and Fig. 3.12. A total data rate of 450 Gbps is transmitted by joint 4-channel. The output of the classification model here includes five categories, which are divided according to SNR>15 dB,

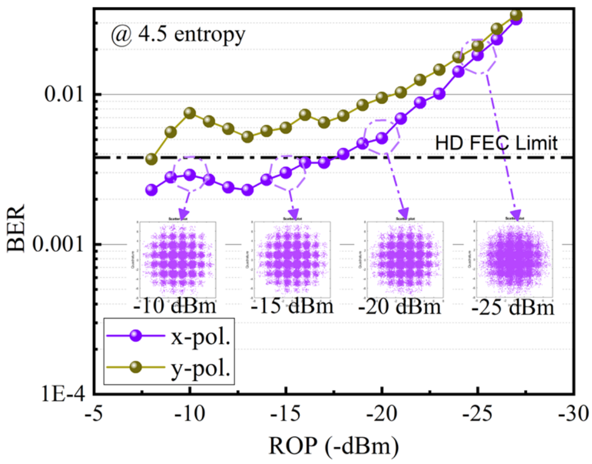

Figure 3.12: The BERs of x-pol. and y-pol. of the dual-polarized coherent optical system at the entropy of 4.5 with the ROP varying from -8 dBm to -27 dBm. (Inset: the constellation diagrams of x-pol. at the ROP of -10 dBm, -15 dBm, -20 dBm and -25 dBm, respectively.)

14∼15 dB, 13∼14 dB, 12∼13 dB, and <12 dB. In Fig. 3.11, for the x-polarized component, the SNRs exceed 15 with the ROP from -8 dBm to -21 dBm. There is no obvious linear downward trend in SNR until ROP is below -20 dBm. For the y-polarized component, before the ROP is lower than -21 dBm, the SNR is basically distributed between 14 dB and 15 dB. For the AMI model with five categories, the receiving data is captured at the ROPs of -16 dBm, -20 dBm, -24 dBm, -26 dBm, and -27 dBm, respectively. In Fig. 3.12, within the HD-FEC limitation, the configuration at -8 dBm ROP can achieve a 450 Gbps transmission over a 10-km SSMF, which is also shown in the above section. The tendency of the BER curves shows a strong correlation with SNR. The constellation diagrams of the x-polarized branch are generated and presented at ROPs of -10 dBm, -15 dBm, -20 dBm, and -25 dBm, respectively. As the ROP decreases, the received PCS-64-QAM constellation diagrams also become blurred.

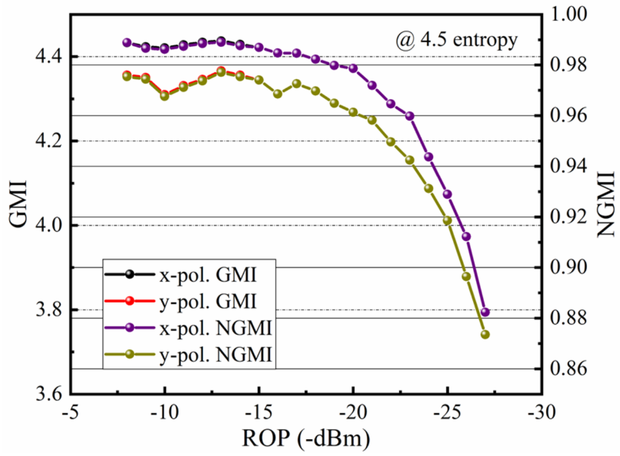

Figure 3.13: The GMIs of x-pol. and y-pol. of the dual-polarized coherent optical system at the entropy of 4.5 with the ROP varying from -8 dBm to -27 dBm.

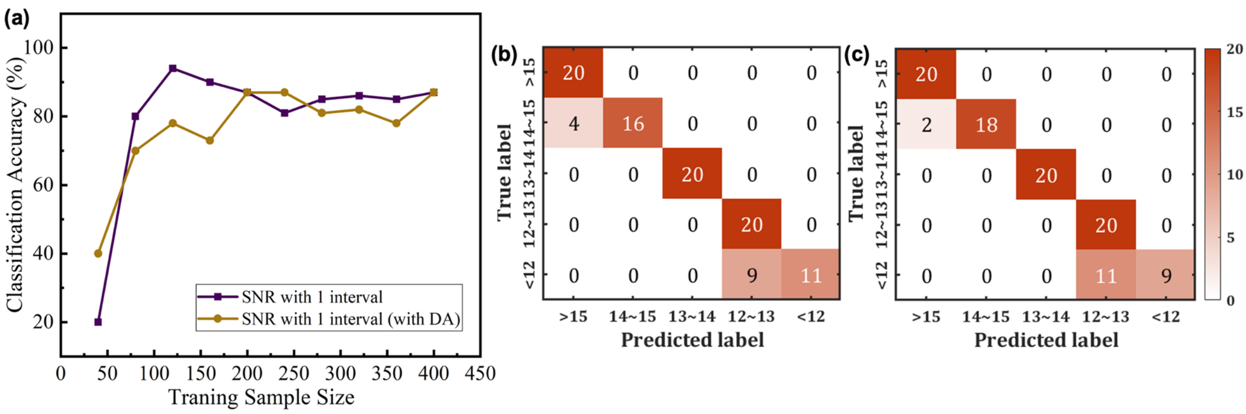

Figure 3.14: The (a) classification accuracy of AMI scheme at the entropy of 4.5 with SNR changing from 11 to 15, and the corresponding confusion matrices of AMI scheme under 400 training sample size (b) without DA and (c) with DA.

As shown in Fig. 3.13, the GMI and NGMI with various ROPs at the same entropy of 4.5 present a consistent trend, both in the x-component and y-component. With the ROP decreasing from -8 dBm to -27 dBm, both the GMI and NGMI show a decreasing trend correspondingly. The consistent trend of curves of GMI and NGMI can be interpreted as normalizing at the same entropy by a linear transformation $NGMI = 1 - (\frac{4.5-GMI}{6})$. Tab. 3.4 further presents the measurement detail including

Table 3.4: The performance comparison with various SNRs at the entropy of 4.5.

x-pol.	ROP (dBm)	-8 ∼-20	-21 ∼-23	-24	-25 ∼-26	- 27
	SNR	>15	14 ∼15	13 ∼14	12 ∼13	<12
	GMI	4.43@ -8	4.33@ -21	4.16@ -24	4.97@ -26	3.79@ -27
y-pol.	ROP (dBm)	-8	-9 ∼-21	-22 ∼-24	-25 ∼-26	- 27
	SNR	>15	14 ∼15	13 ∼14	12 ∼13	<12
	GMI	4.36@ -8	4.25@ -21	4.08@ -24	3.87@ -26	3.74@ -27

SNR, GMI, and contour stellar images with various ROP of the x-component and the y-component, respectively. According to the five SNR distribution ranges that have been specified, the contour stellar images at the ROP of -8 dBm, -21 dBm, -24 dBm, -26 dBm, and -27 dBm, respectively.

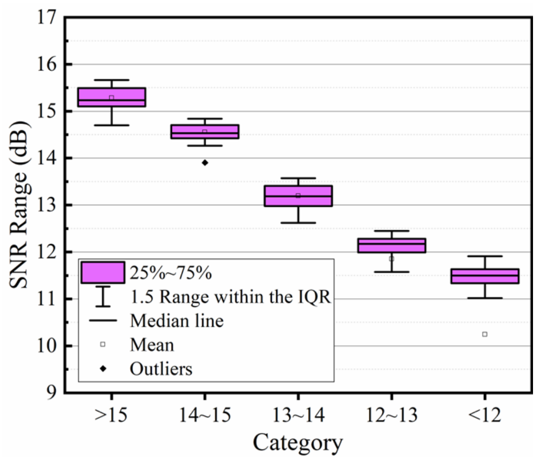

Figure 3.15: The boxplots for the total dataset at the entropy of 4.5.

The classification accuracy results of the SNR monitoring experiments using the proposed AMI model and the associated confusion matrices with and without DA are shown in Fig. 3.14. Fig. 3.14(a) presents the classification accuracy curves of the AMI scheme versus various training sample sizes without DA and with DA. In this experiment, the presence of DA was not able to achieve a significant classification advantage over the experiment without DA. Moreover, compared with the entropy classification experiment, the monitoring classification of SNR cannot achieve a decent result (>90% classification accuracy). After the training sample size reaches 120, the classification curve shows obvious fluctuations with the increase in training sample size, but the classification accuracy does not significantly improve. Without DA, the classification accuracy curve reaches a maximum value of 94% at 120 training samples but decreases to 87% when the training sample size is 400. The overall performance after DA is slightly inferior to when there is no DA operation. Fig. 3.14(b) and Fig. 3.14(c) further present the confusion matrices of the AMI scheme under 400 training sample sizes without DA and with DA. It is obvious that the classification results in the case of low SNR (SNR $<$ 12 dB) are very error-prone. The AMI exhibits nearly half the error rate. In the case of SNR>12 dB, the classification result is more accurate. Excluding the low SNR (SNR<12 dB), the classification accuracy of four samples can reach 95% (without DA) and 97.5% (with DA). This result can be predicted by theSNR test results shown in Fig. 11. The SNR fluctuates and declines with a larger slope as the ROP becomes lower. In order to further explain this phenomenon, we start from the total collected dataset and give a description of its distribution. The total dataset here includes the training dataset, validation dataset, and test dataset. Fig. 3.15 is the boxplot of all the acquired datasets, including x-polarization and y-polarization under 100 times captures. However, for the five datasets under different SNRs, the mean values are all within our specified SNR range. But for category 12$\sim$13, there are many constellation diagram samples actually collected at <12 dB level. While there are many outliers for categories $<$ 12. The instability is due to the fact that this dataset was acquired at an ROP of -27 dBm. These reasons together lead to the low classification accuracy of AL-based AMI between category 12$\sim$13 and category $<$12.

3.5 Time-variant entropy regulated multiple access for flexible coherent PON

This Section was published in Optics Letters (OL).

3.5.1 Introduction

Passive optical networks (PONs) have obtained huge success in the wide-scale deployment of different fiber-to-the-X (FTTX, where X means home, office, cell, etc.) scenarios in the past two decades [12, 14]. Time division-multiple-access (TDMA) and wavelength-division multiplexing (WDM) are the two most commonly adopted standards for current PONs, and their combination, as called time and wavelength division multiplexing (TWDM), can achieve a data rate of over 100 Gbps using direct detection in 2018 [34]. Orthogonal frequency-division multiple access (OFDMA)-PON can provide a dynamic rate and bandwidth allocation, which is beneficial to the uplink transmission from multiple optical network units (ONUs) to the optical line terminal (OLT) [34, 86]. In addition, for next-generation PON deployments, coherent access has been addressed as a promising scheme due to its sensitivity, flexibility, effectiveness, and scalable rate [32]. Using a four-channel coherent transmission system with in-phase/ quadrature (IQ) and dual polarization is not economical. However, following the trend of coherent sinking (towards shorter transmission distance), many low-complexity coherent detection schemes have been proposed, which has accelerated the evolution process [34, 37, 87]. For example, a real-time analog intradyne low-cost coherent receiver was proposed and implemented in a field trial [37]. Additionally, using transmit diversity schemes such as Alamouti coding enables the ONU to receive signals with a single detector [87].

Flexible PON (FLCS-PON) has been proposed as a potential solution recently. In addition, flexible coherent PON (FLCS-CPON) has shown increases in rate and sensitivity [62]. Also, high-order modulation formats can be adopted in power-limited coherent PONs to increase spectral efficiency (SE) [33, 38]. Various multiplexing schemes were proposed to refresh rates or expand scales [36, 39, 40, 53]. Zhang *et al.* adopted time-frequency-division-multiplexing (TFDM) schemes to achieve a 100-Gb/s FLCS-CPON, which regulated the rate in the frequency domain [53]. Among them, probabilistic constellation shaping (PCS) with tunable SE was able to extract additional shaping gain, which is considered a natural solution for beyond-100-Gb/s FLCS-CPONs [66, 68]. Based on the mentioned multiple access and multiplexing techniques, entropy, as a new variable, enables more flexible and adaptive CPONs. The entropy refers to the average amount of information bits per symbol, which also can represent SE in our case. Additionally, all the mentioned FLCS-PON schemes consider the flexible rate, but ignore how to distinguish different access users. Tab. 3.5 further summarizes and compares the performance of the CPONs works mentioned above recently.

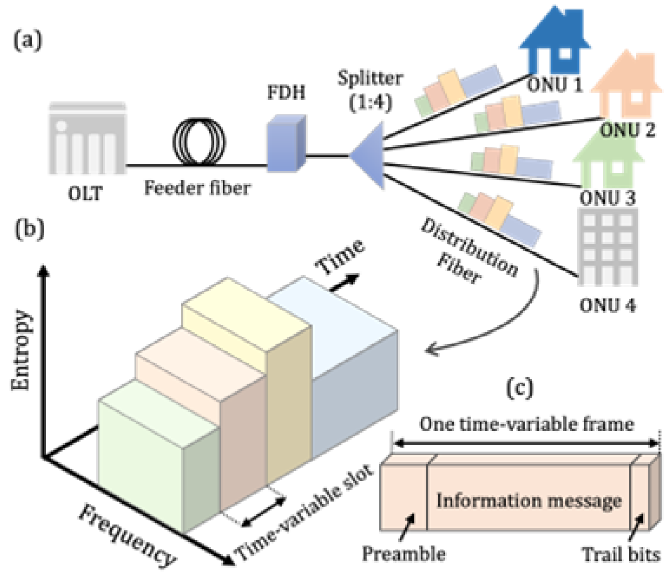

Figure 3.16: (a) The concept of time-variant entropy regulated multiple access scheme for FLCS-CPON. (b) The temporal data stream and (c) a frame structure with a specific entropy.

Table 3.5: Summary of the System Performances of Recent CPON Works.

Year	Group	Modulation format	Rate-flexible	Real-time	Data rate (Gb/s/λ)	Distance (km)
2016	Artiglia et al. [9]	ASK	N	Y	1.25	60
2017	Ferreira et al. [10]	DP-QPSK/8PSK	N	Y	5/7.5	100
2020	Zhang et al. [11]	PDM-QPSK	Y	N	100	50
2020	Xu et al. [12]	DP-64-QAM	Y	N	85.4 $\sim$352	1 $\sim$71.34
2021	Zhang et al. [13]	PDM-QPSK	N	N	100	50
2022	Li et al. [14]	TDM-16-QAM	N	N	200	50
2022	Xing et al. [15]	PCS-QAM	Y	N	85 $\sim$255	20
2022	Borkowski et al. [16]	PCS-PAM	Y	N/A	$<$100	15
2022	**This Letter**	**PCS-64-QAM**	**Y**	**Y**	**350 $\sim$450**	**10**

3.5.2 Principles, Architecture and Experimental Setup

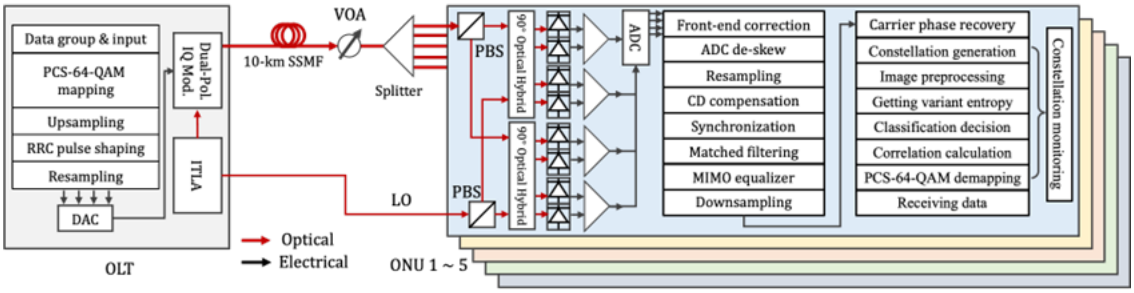

Figure 3.17: The schematic of time-variant entropy regulated multiple access scheme for the real-time dual-pol. FLCS-CPON.

Figure 3.17 presents the concept of the time-variant entropy-regulated multiple access scheme for FLCS-CPON, where Fig. 3.17(a) shows a general PON with a sequence of time-continuous information frames for four independent ONUs. Fig. 3.17(b) and Fig. 3.17(c) further show the temporal data stream of the time-variant entropy-regulated scheme and a specific frame structure. The height difference of continuously different color information frames in Fig. 3.17(b) represents the entropy interval of time-varying frames. The interval value of entropy refers to the minimum difference between all ONUs assigned the specified entropy value. In this work, the interval value of entropies is 0.5, the same for 5 ONUs. Each independent information frame has the modulation format of PCS-64-QAM with Maxwell-Boltzmann distribution. The standard fixed-slot TDMA format is modified to enable the length of the time slot and the value of the entropy for each information frame to be dynamically adjusted. A frame consists of time-variable slots, which consist of the preamble, the information message and the trail bits. The schematic of the time-variant entropy-regulated FLCS-CPON setup is shown in Fig. 3.17. Tx. and Rx. modules are integrated inside one unit with local oscillators operating at 1548 nm and a launch optical power at 0 dBm. At the Tx., a sequence of pseudorandom binary sequences (PRBS) is first generated and divided into 5 ONU groups. The 5 input data sequences are further subjected to PCS-64-QAM mapping with different shaping factors. A series of sequences with different entropy at differing time slots are generated, which will be further shaped by a root raised cosine (RRC) pulse filter with 0.1 roll-off factor, upsampled to 2 samples per symbol (SPS), and sent to a digital-to-analog converter (DAC). The frame length of each polarized component is 95022 samples (2 SPS). The time length of each frame is $\sim$90.9 μs at a 50-G baud rate, and the entropy value remains the same within a time slot. The next experiment is to verify whether these designed sequences with different entropies can be received by a specific ONU at any time slot. A four-channel coherent transmission system is implemented by a dual-polarized IQ modulator (Dual-Pol. IQ Mod.). Then the optical signal is passed through a 10-km standard single-mode fiber (SSMF), a variable optical attenuator (VOA), and a beam splitter to a specific ONU. The transmitted frames are captured by a standard dual-pol. coherent receiver. The converted frames are sampled and quantified by an analog-to-digital converter (ADC). Then, front-end correction, ADC de-skew, resampling to 2 SPS, chromatic dispersion (CD) compensation, synchronization, matched filtering, adaptive multiple input multiple output (MIMO) equalization, downsampling to 1 SPS, and blind phase search (BPS)-based carrier phase recovery are performed in order, before monitoring the constellation and signal-to-noise ratio (SNR). The compensated and corrected sequences are used to generate constellation diagrams. The preprocessing includes binarization and clipping of the input constellations since the generated constellations are relatively symmetrical. Then, the normalized cross-correlation coefficient (NCC) calculation and template matching are performed, according to the following formula:

$$C\left(u,v\right)=\frac{\sum_{x,y}\left[f(x,y)-\overline{f_{u,v}}\right]\left[t(x-u.y-v)-\bar{t}\right]}{\sqrt{\sqrt{\sum_{x,y}\left[f(x,y)-\overline{f_{u,v}}\right]^{2}\sum_{x,y}[t(x-u.y-v)-\bar{t}]^{2}}}},\tag{3.2}$$

where $C\left(u,v\right)$ is the NCC;$f\left(x,y\right)$ is the clipped input constellation diagram with the resolution of 344 × 263; $t\left(x,y\right)$ is the template diagram with the resolution of 514 × 433; $\bar{t}$ is the mean of the template; and $\overline{f\left(u,v\right)}$ is the mean of $f\left(x,y\right)$ in the region within the template range. The constellation identification refers to obtaining the corresponding transmitted entropy value from the specific received constellation, to determine whether it matches the assigned entropy value of ONU. Here, weighing the accuracy and complexity of the image classifier, a simple but effective weak classifier for real-time monitoring is installed. The NCC algorithm is designed to monitor the constellation and the matching accuracy is calculated at every sample time. A 5 × 8 constellation diagrams at different SNRs are captured to form 5 calibration groups. Then, the constellation captured at a specific moment is monitored in real-time and compared individually with the calibration groups. The NCC algorithm extracts and returns the entropy of every constellation at each moment.

3.5.3 Results and Discussions

Figure 3.18 shows the relationship between the SNR and received optical power (ROP) of the x/y-pol. channels, and similar tendencies can be observed. The SNR varies from 11 dB to 16 dB, which corresponds to a change in ROP from -10 dBm to -24 dBm. The

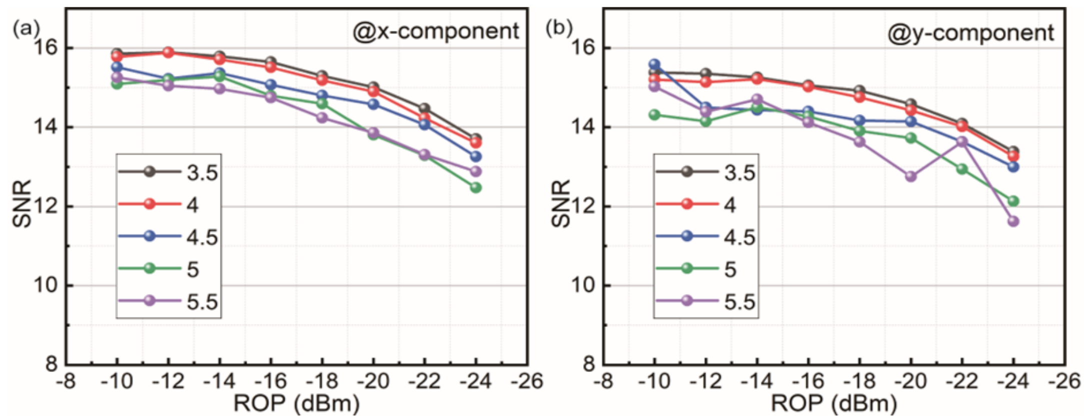

Figure 3.18: The SNR of (a) x-component and (b) y-component of the dual-pol. FLCS-CPON with the entropy varying from 3.5 to 5.5.

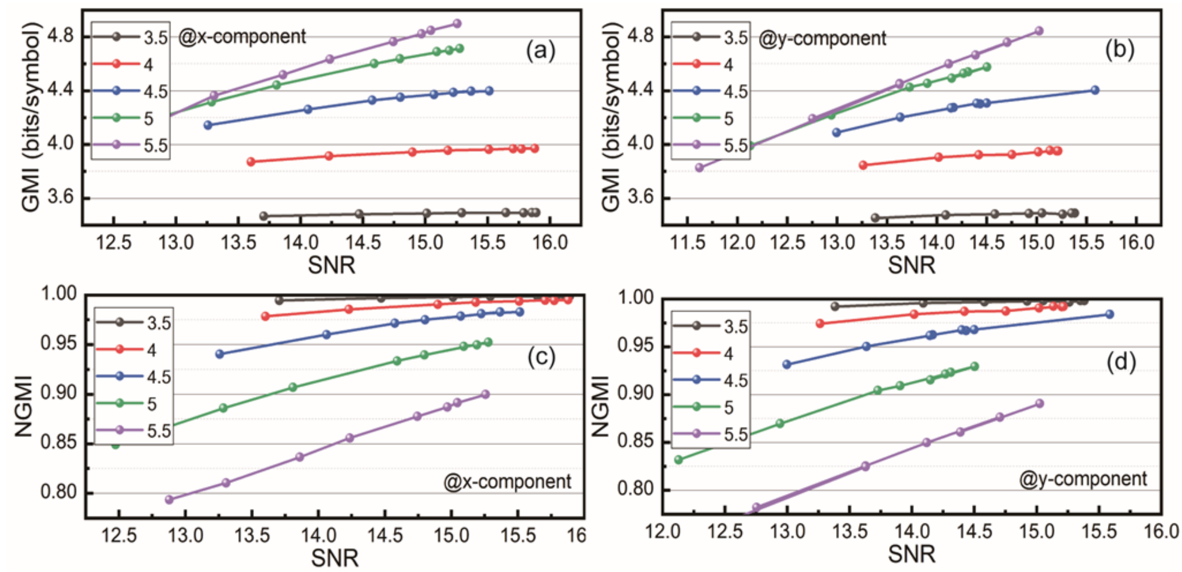

Figure 3.19: The GMI of (a) x-component and (b) y-component and the corresponding NGMI of (c) x-component and (d) y-component of the dual-pol. FLCS-CPON with the entropy varying from 3.5 to 5.5.

SNR decreases as the entropy increases. The generalized mutual information (GMI) and normalized generalized mutual information (NGMI) of the x/y-pol. component are presented in Fig. 3.19. Fig. 3.19(a) shows the x-pol. GMI as a function of SNR. This GMI shows a positive correlation with both entropy and SNR. The x-pol. NGMI results are shown in Fig. 3.19(c), which are negatively correlated with increasing entropy. The y-pol. branch presents similar GMI and NGMI results in Fig. 3.19(b) and Fig. 3.19(d).

The x/y-pol. BERs versus ROP with entropies from 3.5 to 5.5 are presented in Fig. 3.20(a) and Fig. 3.20(b). With an increase of entropy value, the BER rises in steps. For a specific ONU, the BER rises slightly with a decrease of ROP from -10 dBm to -24 dBm. A maximum 225-Gb/s PCS-64-QAM signal with an entropy of 4.5 can be successfully transmitted at an ROP of -10 dBm of x/y-polarization, below the HD-FEC threshold. The 200-Gb/s and 175-Gb/s signals can also be transmitted at an ROP range from -10 dBm to -24 dBm at 50 GBaud, but as for the entropy of 5 and 5.5, further baud rate reduction is required to decrease the BERs below the HD-FEC threshold. The entropies of 3.5, 4, and 4.5 correspond to the net rates of 327.1 Gb/s, 373.8 Gb/s, and 420.5 Gb/s, respectively. Clear gaps between the BER levels of different entropies are shown, which confirms the feasibility of distinguishing 5 different ONUs by time-varying entropy. The corresponding constellations extracted from Fig. 3.20(a) and Fig. 3.20(b) at -10-dBm ROP are shown in Fig. 3.20(c) and Fig. 3.20(d), which also show obvious differences. The interval of 0.5 reduces the complexity of monitoring and identification and also enables a real-time fast-matching algorithm.

Figure 3.21 shows the NCC coefficient between the 5 calibration image groups and 32 input image groups. The latter input groups include 5 variant entropies at different ROPs from -10 dBm to -24 dBm. The calibration image groups are obtained by the weighted average of multiple constellation diagrams under different SNRs as shown in the 5 inset figures of Fig. 3.21, and the captured input constellations are binarized and truncated to 1/4 size according to their approximate centrosymmetric properties.

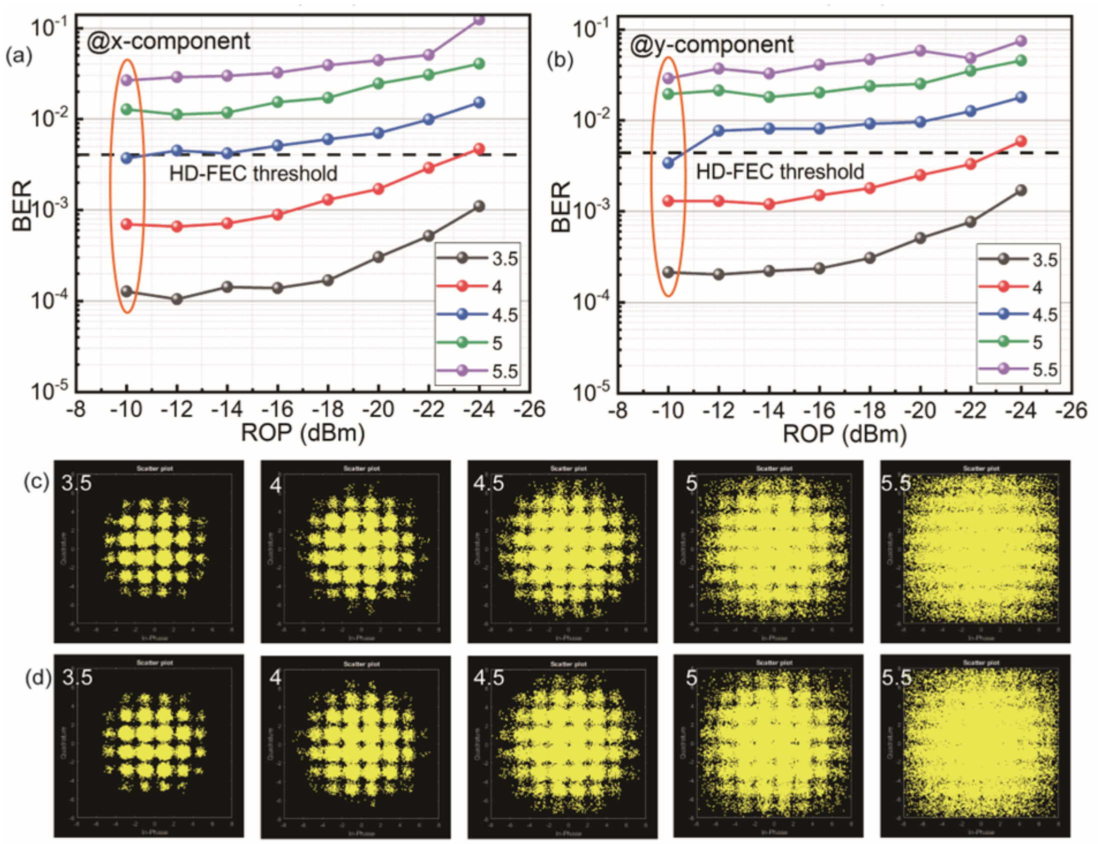

Figure 3.20: The BER of (a) x-component and (b) y-component of the dual-pol. FLCS-CPON with the entropy varying from 3.5 to 5.5. The corresponding constellation diagrams of (c) x-component and (d) y-component at -10-dBm ROP extracted from red circles of (a) and (b).

Then, the NCC distribution can be obtained. Obvious layering can be observed between each set of input image groups from Fig. 3.21. When the entropy of the input image is consistent with the calibration group, the NCC coefficient value is relatively higher compared with the other 4 groups, and this conclusion holds under all ROPs.

The time-variant entropies are respectively defined as 3.5, 4, 4.5, 5, and 5.5 for only 5 independent ONUs in our demonstration, and the length ratio of the time slots is arbitrarily chosen as 1:1:2:1:1. A total of 181 samples were sampled in the time domain, and due to dual-polarization, a total of 362 constellation samples were obtained

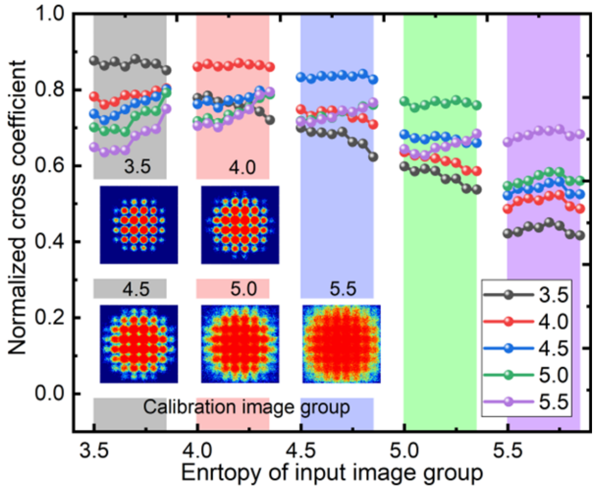

Figure 3.21: The NCC distribution of the constellation diagrams with different entropies and SNRs. (Inset: Five matching templates.)

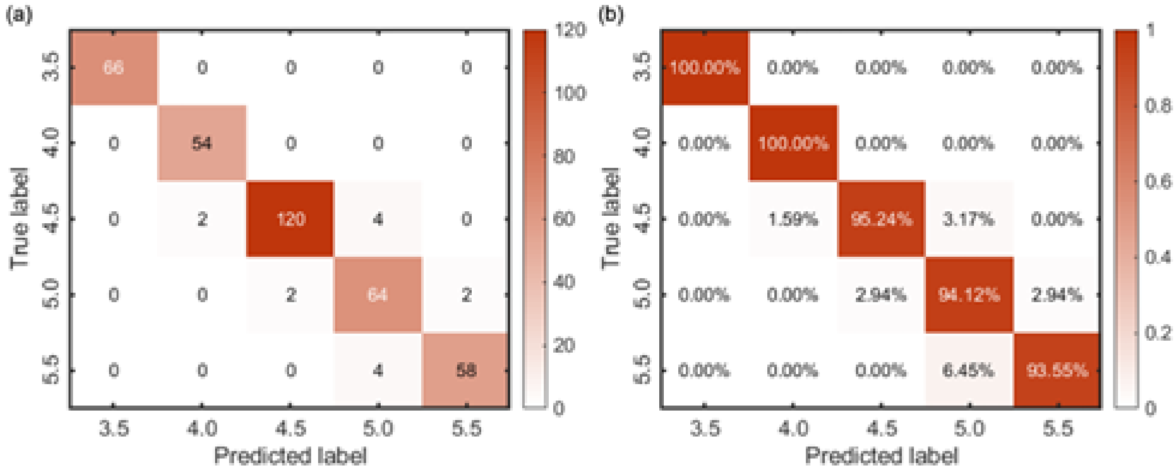

Figure 3.22: The (a) confusion matric of 362-times testing at different random sample times over the FLCS-CPON setup. (b) Expressed as a percentage.

for importing into the classifier for testing. The confusion matrix is presented in Fig. 3.22(a) and the accuracy of each category is also calculated and shown in Fig. 3.22(b). As an example, we captured a total of 62 acceptance sequences at the entropy of 5.5. The NCC classifier correctly decided and outputted 58 times. However, 4 of them were incorrectly judged as 5.0. During the acquisition process, the ROP is arbitrarily changed between -10 dBm and -24 dBm, which means that the captured constellations with different entropies will correspond to different SNRs. When the entropy is equal to 3.5 or 4, the classification accuracy reaches 100%. At the entropy is 4.5, 5, or 5.5, the NCC classifier will misjudge in some specific low-SNR cases. Overall, the classification accuracy can be maintained above 96.13%. More access capacity can be achieved either by designing finer entropy gaps with corresponding image classifiers, or by configuring power, wavelength, or polarization. The error correction mechanism at the receiver also needs to be developed to prevent identification errors under low SNR.

3.6 Rate Monitoring Performance of AL-based Classifier for Rate-flexible TWDM-CPON

3.6.1 Introduction

With the explosive growth of the information scale of Internet applications such as cloud computing, big data-based artificial intelligence (AI), and augmented reality/virtual reality (AR/VR) streaming media, the previous access network facilities have urgently needed upgrading to meet the requirements of ultra-high-speed and rate-flexible passive optical network (PON) [88]. On the one hand, with the increase in rate and performance requirements, the number of access optical network units (ONUs) also increases over a $\sim$80-km metro access ring from an optical line terminal (OLT) [89]. The development of simplified coherent detection technology reduces the cost and promotes the development of coherent optical communication to medium and short distances. Coherent access such as ¿100-G time-wavelength division multiplexing (TWDM) coherent PON (CPON) is considered as next-generation mainstream PON architecture [39, 90].

On the other hand, more adaptive and flexible rate changes must be developed to accommodate different channels and access points. Previous subcarrier division schemes in the frequency domain have achieved remarkable results in rate adaptation [53]. While probabilistic constellation shaping-based (PCS-based) with tunable spectral efficiency (SE) characteristics enable a more continuous rate-adaptative scheme by varying the entropy of the transmitted signal[39, 68, 84]. Thus, combining PCS with variable entropy and TWDM-CPON can not only improve capacity and performance but also flexibly allocate spectrum for large-scale access users. Regulating rate through time-varying entropy requires an entropy/rate monitoring scheme at the receiver. However, there is no mechanism and discussion to monitor the changing rate/entropy in PCS-based optical systems or networks.

3.6.2 Principles, Architecture and Experimental Setup

Figure 3.23 illustrates the schematic of the proposed entropy-regulated rate-flexible TWDM-CPON architecture and downstream experimental setup. At the transmitter (Tx.), the rate-flexible signal is generated by tuning the entropy value at different continuous time slots. The specific digital signal processing (DSP) for 4-channel dual-polarized IQ signals include PCS-64-QAM mapping, upsampling to 2 sps, RRC pulse shaping, resampling, and digital-to-analog converter (DAC), respectively. The electrical signal and the carrier lightwave from micro-integrable tunable laser assembly (micro-ITLA) overlapped inside a dual-polarized IQ modulator (DP-IQ Mod.), and they passed through an 80-km standard single-mode fiber (SSMF). The receiving optical power level to different ONUs can be changed by a variable optical attenuator (VOA). The inset Figure 3.23(a) shows a time frame stream with various entropy-regulated rates, which is packaged and delivered to all the ONUs. At the receiver (Rx.), a micro-ICR and an ADC are set to receive the signal, while the demodulation DSP can be divided into a signal recovery part and an entropy identification part. The converted electrical signal is firstly front-end corrected. Then analog-to-digital converter (ADC) de-skew, resampling to 2 sps, chromatic dispersion (CD) compensation, synchronization, matched filter, multi-input multi-output (MIMO) equalization, downsampling, and carrier phase recovery are executed sequentially. Then, the classifier will determine whether the entropy/rate has changed between each time slot according to the point distribution of the acquired constellation, and further define the specific value of the entropy/rate.

The inset of Fig. 3.23(b) is a general performance comparison of image classifiers based on different principles, and the red dotted line is the designed optimized direction. The trade-off among computational complexity, recognition accuracy, and data overhead is the criteria leading to proposing AL-based classifiers. Generally, some deep learning (DL)-based classified schemes ask to collect large amounts of data to train networks and maintain accuracy. Machine learning (ML)-based schemes are a compromise, which can get better recognition and maintain a small data overhead. In addition, the methods based on numerical calculation require only a few data samples for reference, but the recognition accuracy is relatively low. Next, the proposed AL scheme is further compared with deep neural network (DNN), support vector machine (SVM), and simply normalized cross-correlation (NCC) calculation.

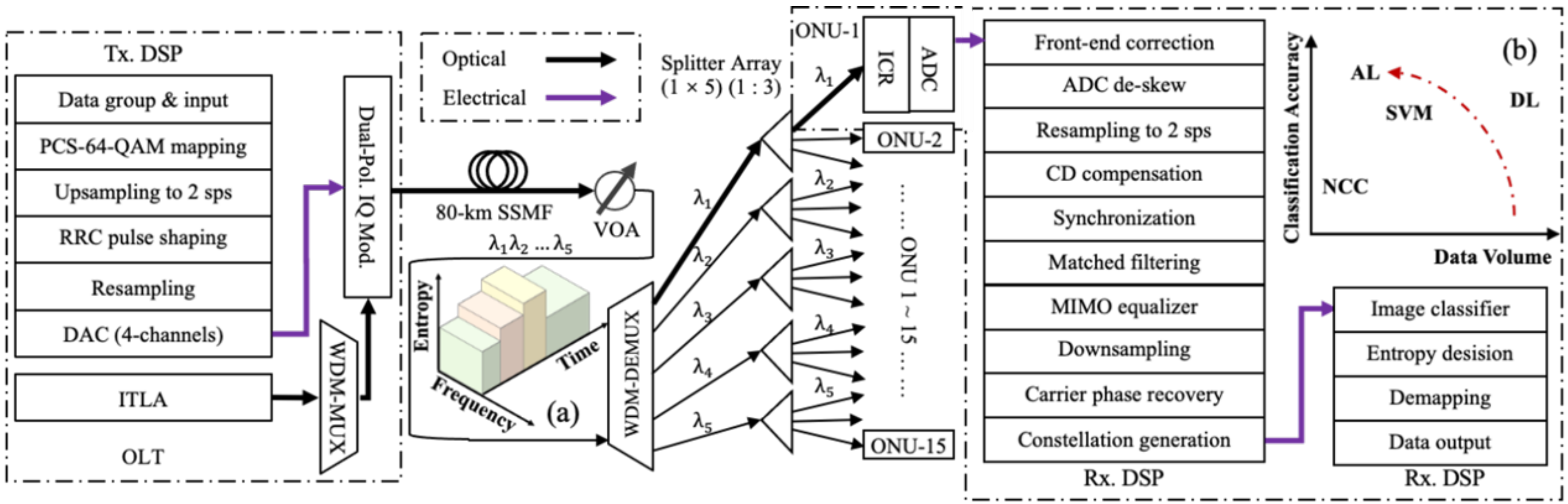

Figure 3.23: The 350-Gb/s/$\lambda \sim$ 450-Gb/s/λ downstream experimental setup for PCS-based rate-flexible TWDM-CPON with image classifier-based entropy/rate monitoring. Inset figures: (a) The frame structure of flexible rate by time-variant entropy for different ONUs; (b) General performance comparisons between training data volume and classification accuracy with classifiers based on different principles in our work.

3.6.3 Results and Discussions

In our TWDM-CPON setup, different ONUs groups are divided by wavelengths, while within the single ONUs group, the single ONU is divided by a 1:3 power splitter. Here, the entropy values are changed among 3.0, 4.0, and 4.5, corresponding to the rate changing from 350 Gb/s/λ $\sim$ 450 Gb/s/λ with a minimum rate tuning step of 25 Gb/s/pol./λ. For the specific ONUs group at 1560 nm, as shown in Fig. 3.24, the communication performance has an obvious layering phenomenon with the changing of entropy. In Fig. 3.24(a), the SNRs decrease with the decreasing of the ROP, and at the ROP of -15 dBm, the SNR can reach 16.0238 dB with an entropy of 3.5. The diagram of BERs versus ROPs is further shown in Fig. 3.24(b). The transmitted signals with the entropies of 3.5 and 4.0 are capable of reaching the hard-decision forward error correction (HD-FEC) threshold of 3.8 × 10^{-3}, and the BER values are 4.9 × 10^{-4} and 1.45 × 10^{-3}, respectively. Inset figures in Fig. 3.24(b) are the PCS constellation diagrams of 3.5, 4.0, and 4.5 at -15 dBm, respectively. The constellation points spread out with increasing entropy. The corresponding generalized mutual information (GMI) and normalized generalized mutual information (NGMI) are further presented in Fig. 3.24(c) and Fig. 3.24(d). For example, at -15-dBm ROP and 1560 nm, the GMI and NGMI are 3.4368 and 0.9899 at the entropy of 3.5. A further experimental measurement is conducted to demonstrate the stability among different ONUs groups at -15 dBm. Three wavelengths of 1560 nm, 1561 nm, and 1562 nm are adopted to support three ONUs groups. From Fig. 3.25(a) and Fig. 3.25(b), although the SNRs slightly decrease from 1560 nm to 1562 nm, the BERs performance is fairly consistent and stable across carriers. Similarly, we show the measured GMI and NGMI at different entropies and carriers in Fig. 3.25(c) and Fig. 3.25(d).

The overall identification performance is presented in Fig. 3.26. With few training samples, the AL-based scheme can achieve rapid convergence through the query mechanism in Fig. 3.26(a). At the entropy interval of 0.5 (black curve), corresponding to the entropies of 3.5, 4.0, and 4.5, the identification accuracy reaches 100% with only 96 training samples. Then, a confusion matrix with 92 % identification accuracy is further presented in Fig. 3.26(b) using 72 training samples. The abscissa constellation diagrams in Fig. 3.26(b) are with an entropy of 3.5, 4.0, and 4.5 with 0.5 intervals, respectively. When the step size of entropy/rate tuning is gradually reduced to 0.1/5 Gbps at 50 Gbaud, higher requirements are placed on the performance of the classifier. At 0.1 entropy interval, the AL-based classifier was able to improve the recognition accuracy of constellation maps to ¿91% under 144 training samples. Although there are some fluctuations in the curve with the increase in the sample size, it can be maintained above 90%. Next, Fig. 3.26(c) shows a confusion matrix with 98% identification accuracy with 216 training samples among 4.5, 4.6, and 4.7. In addition, in Fig. 3.26(a), NCC can reach a $\sim$ 96% identification accuracy with 24 samples but only works when the entropy interval is large and rapidly ineffective as the entropy interval narrows from 0.5 to 0.1. For a finer rate tuning, SVM cannot reach a relatively high accuracy at a low training sample, while a DL-based classifier requires a large set of training samples with annotations.

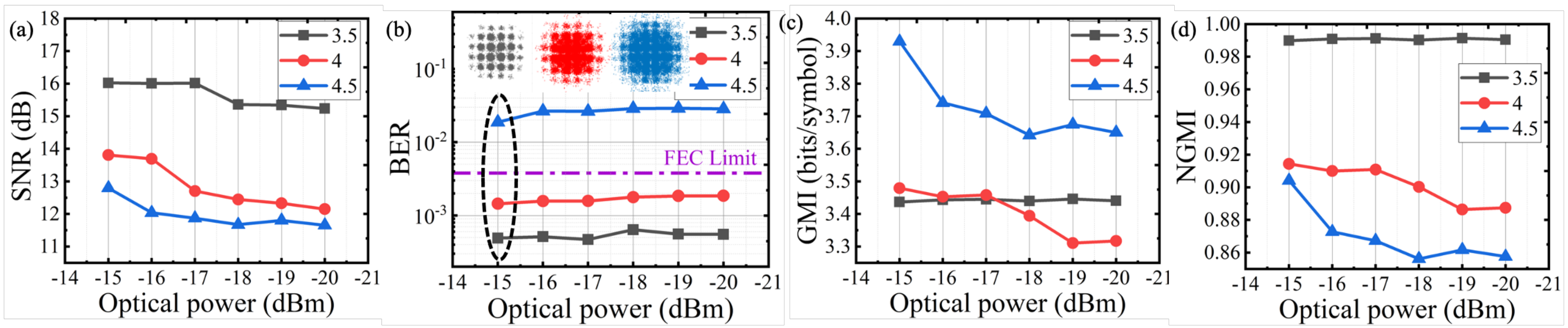

Figure 3.24: System performances of single ONU with 1560 nm at 50.12 Gbaud: (a) SNR, (b) BER, (c) GMI, and (d) NGMI versus ROP from -15 dBm to -22 dBm with entropy varying from 3.5 to 4.5; (Inset figures in (b): the constellation diagrams at ROP of -15 dBm.)

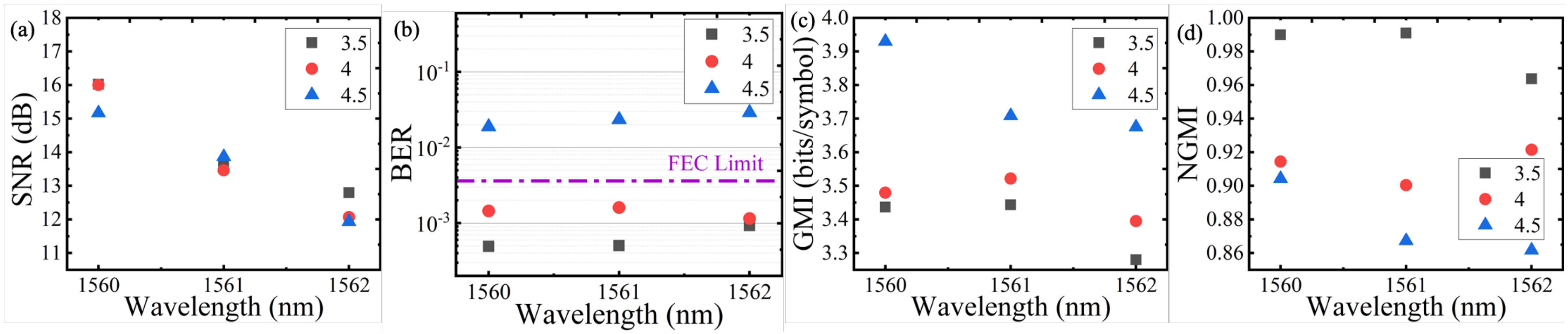

Figure 3.25: System performances of multiple ONUs with the wavelength of 1560 nm, 1561 nm and 1562 nm at 50.12 Gbaud at -15 dBm ROP: (a) SNR, (b) BER, (c) GMI and (d) NGMI versus various wavelengths with entropy varying from 3.5 to 4.5.

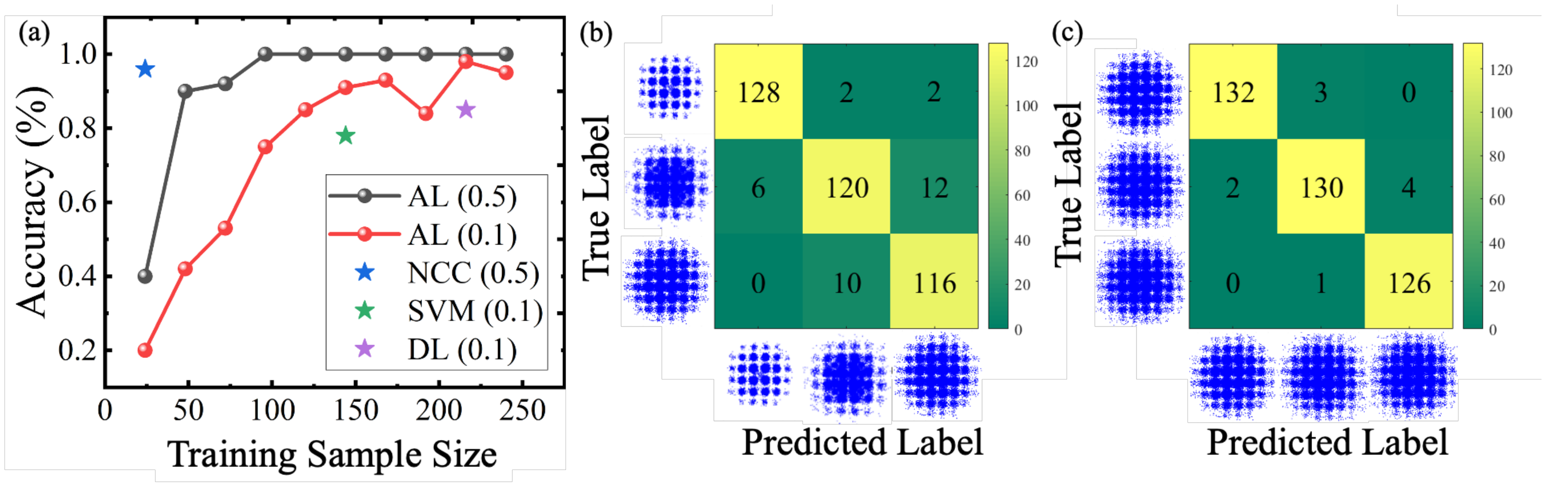

Figure 3.26: Classification performances and comparisons: (a) Classification accuracies of various schemes verse different training sample volumes from 24 to 240 at an entropy interval of 0.5 (from 3.5 to 4.5) or 0.1 (from 4.5 to 4.7). (b) The confusion matrix of the AL-based scheme at the entropy of 0.5 and training sample size of 72 (Coordinates: 3.5, 4.0, 4.5; 92% identification accuracy). (c) The confusion matrix of the AL-based scheme at the entropy interval of 0.1 and training sample size of 216 (Coordinates: 4.5, 4.6, 4.7; 98% identification accuracy).

3.7 Section Summary

This section describes our exploration of the estimation and monitoring of physical layer parameters in coherent optical systems and coherent optical access networks.

Chapter 4

Dynamic Encryption in CPON

4.1 Overview and Research Status

Many works have been reported to encrypt data at the media access control (MAC) layer, network layer, or transport layer. However, encryption at higher layers cannot protect physical layer control and header information, which can lead to further hardware attacks. The physical layer security issue is another pending problem with the development of >100-G access networks. On the other hand, for the rate-flexible system, dynamic encryption of data frames at each rate is also an urgent issue. To protect the users from physical layer attacks, a series of encryption methods has been proposed. Digital data encryption technologies such as advanced encryption standard (AES) [91], data encryption standard (DES) [92], Rivest-Shamir-Adleman (RSA) [93], Blowfish encryption [94], and chaotic generation algorithms [86, 93, 94, 95, 96, 97], can be implemented by low-costs DSP without additional hardware sustain. Among them, digital chaotic encryptions with noise-like and wide spectrum characteristics demonstrate superiority and compatibility considering a combination of confidentiality, randomness, key richness, and replacement in optical systems and networks. Since the chaotic key can be defined by slightly changing the initial values of chaotic systems, massively parallel encryption sequences can be easily generated. This characteristic is suitable for multiple-rate PON architecture in which an OLT node transmits information to multi-point ONU nodes. Chaos and deoxyribonucleic acid (DNA) encoding schemes were designed to enhance the security of OFDMA-PON [86]. A four-dimensional (4D) hyperchaotic partial transmit sequence (PTS) is implemented to generate the chaotic partition information for OFDM symbol synchronization in OFDM-PON [95]. Subsequently, a high-reliability and high-security OFDM-PON with a 14.7 Gb/s data rate over a 25-km standard single-mode fiber (SSMF) is proposed, using modified Lorenz chaotic mapping but without a flexible rate [96]. Then, Z. Yang *et al.* recently verified a 30-Gb/s coherent chaotic optical link of over a 340-km long fiber transmission with deep learning-aided synchronization [97]. Chaotic encryption was first proposed and combined in PCS-based 10-G fixed-rate PON as a constant composition distribution matching to enhance the physical layer security [98]. Exploiting the rich and initial value-sensitive properties of generating sequences from chaotic systems, the most important problem addressed in this work is the dynamic encryption problem in access networks for rate-tunable optical communication. We further list and compare some recent PON or CPON works in Tab. 4.1.

Table 4.1: Summary and comparison of recent works on TDM/ WDM/ TWDM-PON/ CPON works.

Year	Group/Ref.	Modulation format	Multiplexing scheme	Encryption	Rate-flexible	Real-time	Data rate (Gb/s/λ)	Distance (km)
2015	Hu et al. [15]	16-QAM	OFDM	Y	N	N	8.9	20
2016	Artiglia et al. [13]	ASK	WDM	N	N	Y	1.25	60
2017	Ferreira et al. [18]	DP-QPSK/8PSK	WDM	N	N	Y	5/7.5	100
2018	Zhang et al. [35]	QAM	OFDMA	Y	N	N	36.77	50
2020	Zhang et al. [11]	PDM-QPSK	TDM	N	Y	N	100	50
2020	Xu et al. [16]	DP-64-QAM	N/A	N	Y	N	85.4 $\sim$352	1 $\sim$71.34
2020	Ren et al. [39]	PCS-QAM	OFDM	Y	N	N	8.9	25
2020	Xiao et al. [27]	PCS-16-QAM	WDM	N	N	N	5 × 100	20
2021	Zhang et al. [26]	PDM-QPSK	N/A	N	N	N	100	50
2021	Shen et al. [37]	QAM	OFDM	Y	N	N	14.7	25
2021	Borkowski et al. [21]	NRZ/PAM4	TDM	N	Y	N/A	50/100	<17.3
2022	Li et al. [19]	16-QAM	TDM	N	N	N	200	50
2022	Xing et al. [28]	PCS-QAM	TDM	N	Y	N	85 $\sim$255	20
2022	Borkowski et al. [30]	NRZ/PAM4	TWDM	N	Y	N/A	<100	<15
2022	**This Work**	**PCS-64-QAM**	**WDM**	**Y**	**Y**	**Y**	**212.80 $\sim$348.12**	**80**

In this work, we proposed a physical layer security enhancement method for a high-speed rate-flexible PCS-based WDM-CPON framework. The rate of transmitted PCS-64-QAM signals can be tuned by the various entropies, which are further encrypted by utilizing Lorenz chaotic encryption sequences. The Lorenz system can generate a large number of chaotic sequences for parallel multi-channel transmission by setting different highly-sensitive initial seeds, and the PCS-64-QAM sequences are mapped in a pseudo-m-QAM format. Compared with the original PCS-64-QAM link, the pseudo-m-QAM mapping eliminates the entropy information of the original mapping and performs chaotic XOR on the link bits. Then, the generated rate-flexible security-enhanced pseudo-16-QAM sequences are experimentally demonstrated by a real-time dual-polarized WDM-CPON planform over an 80-km SSMF link. The entropy is changed from 3.5 to 5.5 with 0.5/0.1 interval in the demonstration, and the minimum adjustable-rate step size is 3.408 × 2 Gbps at 51.12 GBaud. A successful confidential transmission with data rate ranging from 211.80 Gbps to 348.12 Gbps is achieved for 6 $\lambda \times 2$ independent ONUs within the 7% hard-input forward error correction (FEC) threshold of 3.8×10^{-3}.

4.2 Experimental Setup

Table 4.2: The basic experimental WDM-CPON setup parameters and their corresponding values.

Parameter	Value
Operating wavelength	1560 nm ∼1562.5 nm
Operating wavelength interval	0.5 nm
Launch optical power (LOP)	0 dBm ∼4 dBm
Received optical power (ROP)	-15 dBm ∼-20 dBm
Max. supported ONUs	6 × 2
Transmission distance	80 km
Baud rate	51.12 GBaud
Entropy range	3.5 ∼5.5
Rate range	211.80 Gbps ∼348.12 Gbps
Min. tunable entropy	0.1
Min. tunable rate	3.408 × 2 Gbps
Roll-off factor	0.1
Polarization state	2
WDM Channel num.	6

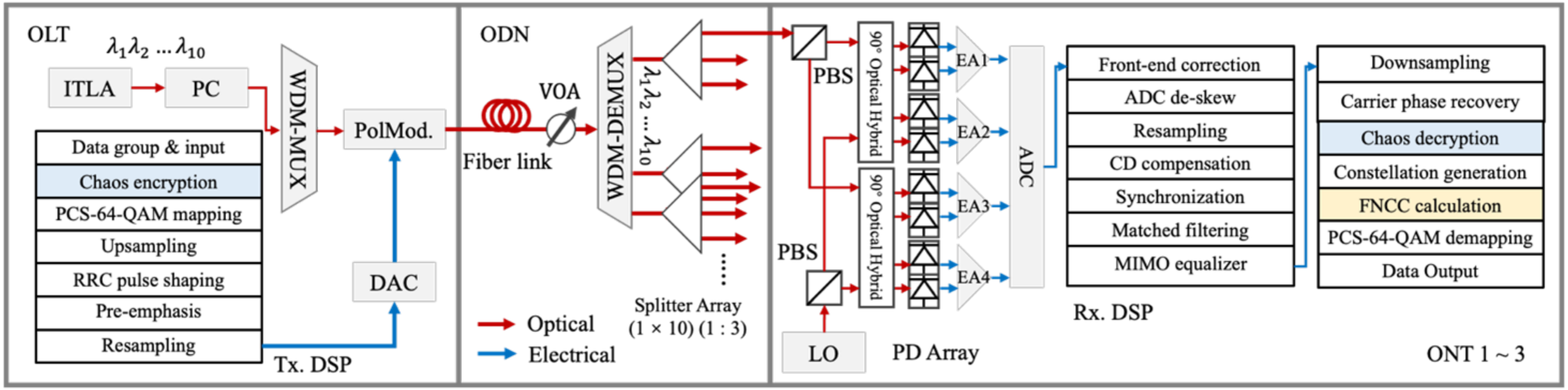

Figure 4.1: The experimental setup and DSP flow of rate-flexible PCS-64-QAM WDM-CPON architecture with chaotic entropy over 80-km SSMF, including (a) OLT transmitter; (b) optical distributed node; and (c) multiple ONU destinations. (Blue block: Chaotic encryption and decryption positions.)

Fig. 4.1 illustrates the baseline DSP flow and WDM-CPON architecture with an OLT comprising 6 $\times$ 2 ONTs, using 6 wavelengths of C-band and 2 divided power levels. The variant entropies change from 3.5 to 5.5, corresponding to a flexible rate from 211.80 Gbps to 348.12 Gbps (136.32-G tunable range) with a minimum of 0.1 tunable steps for a single polarization state at 51.12 GBaud. At the transmitter (Tx.) side in OLT, a micro-integrable tunable laser assembly (μ ITLA) generated light with 6 different wavelengths including 1560 nm, 1560.5 nm, 1561 nm, 1561.5 nm, 1562 nm, and 1562.5 nm, which are tagged as λ_1,λ_2,...,λ_6. After passing a polarization controller (PC) and a wavelength division multiplexer (WDM-MUX) module, the generated laser light with different wavelengths will be superimposed with the encrypted mapped and pre-emphasized data sequences, which is enabled by a compact dual-polarized IQ modulator (Dual-Pol. IQ Mod.). For the Tx. DSP, the data sequence is obtained firstly by generating a pseudo-random binary sequence (PRBS), which is then processed by the combined PAS and encryption scheme as introduced in Fig. 4.1. The encrypted symbol sequence is up-sampled to 2 sps, shaped by a root raised cosine (RRC) pulse filter, pre-emphasized and finally quantified. Among them, the chaotic sequence is generated from the proposed simplified Lorenz chaotic system. The encrypted 4-channel sequences are imported into a digital-to-analog converter (DAC). The modulator corresponds to 4 channels with IQ and dual polarization status, represented by XI, XQ, YI, and YQ, respectively.

The optical distribution node (ODN) consists of 80-km SSMF, a C-band variable optical attenuator (VOA), wavelength division de-multiplexer (WDM-DEMUX), and 1:2 beam splitter arrays, respectively. Here, two sub-ONUs are grouped together and differentiated by the power splitter. The entire coherent transmission platform has a total of 6 ONU groups which are differentiated by 6 wavelengths. Here, within an ONU group with 1:2 power division, the performance of its two sub-ONUs is almost the same. As for the division with six wavelengths among different ONU groups, the communication performance is slightly different.

Therefore, in subsequent experiments, ONUs at different wavelengths is compared, but not two units of the same ONU group. At every ONU, the local oscillator (LO) is also supported by the ITLA, and a typical coherent detection structure is provided by a micro-integrated coherent receiver (μ ICR), as shown in Fig. 5. For the Rx. DSP, front-end correction, analog-to-digital converter (ADC) de-skew, resampling to 2 sps, chromatic dispersion (CD) compensation, synchronization, matched filtering, adaptive multiple-input multiple-output (MIMO) equalization, downsampling to 1 sps, and phase carrier recovery are performed in order to eliminate link effects and obtain the original sequences before decryption. Here, the DAC and the ADC sampling rates are both $\sim$ 70 GSa/s with both 8-bit vertical resolutions. The carrier phase recovery is based on blind phase search (BPS), and the adaptive MIMO equalizer is achieved by radius-directed equalization (RDE) under 2 samples per symbol with a 15-taps length. Next, the received pseudo-16-QAM signal is demapped into bits, which are then decrypted using the same key as the transmitter side. The abovementioned DSP demonstration is all performed in real-time. For each varying entropy/rate value, there is a specific initial set to stimulate the same chaotic system and generate a corresponding encrypted sequence. Finally, the BER is calculated. In the following Tab. 4.2, the basic parameters of the proposed CPON setup are listed and the corresponding values are shown.

4.3 Results and Discussions

For evaluating the WDM-CPON performances, the spectrum and histograms are first calculated and presented at each Tx. steps in this section, respectively. Then, for the receiving performance of single or several ONUs, the SNRs and BERs are present with different entropies, ROPs, and wavelengths, respectively.

4.3.1 Characterization of encrypted input signals

Figure 4.2 shows the characteristics of electrical power versus frequency, and cumulative distribution histogram versus four-channel input sequences (XI, XQ, YI, and YQ). Taking the entropy of 5.5 and the baud rate of 51.12 GBaud as an example, the DSP of four input signals is equivalent at the transmitter. The spectrum of the four signal streams is highly overlapping in the frequency domain with a 51.12-GHz double-side bandwidth, as shown in Fig. 4.2(a), Fig. 4.2(c), and Fig. 4.2(e). And the cumulative distribution histograms are shown almost similar overlapping areas in Fig. 4.2(b), Fig. 4.2(d), and Fig. 4.2(f). Thus, the following conclusions can be extended to four-channel signals by analyzing only one single channel. The spectra of Fig. 4.2(a) are obtained from the signal mapping from the original data sequence to PCS-64-QAM format by fast Fourier transform (FFT). The double-side spectra of any signal appear very flat from -25.56 GHz to 25.56 GHz. Fig. 4.2(b) is the corresponding cumulative distribu-

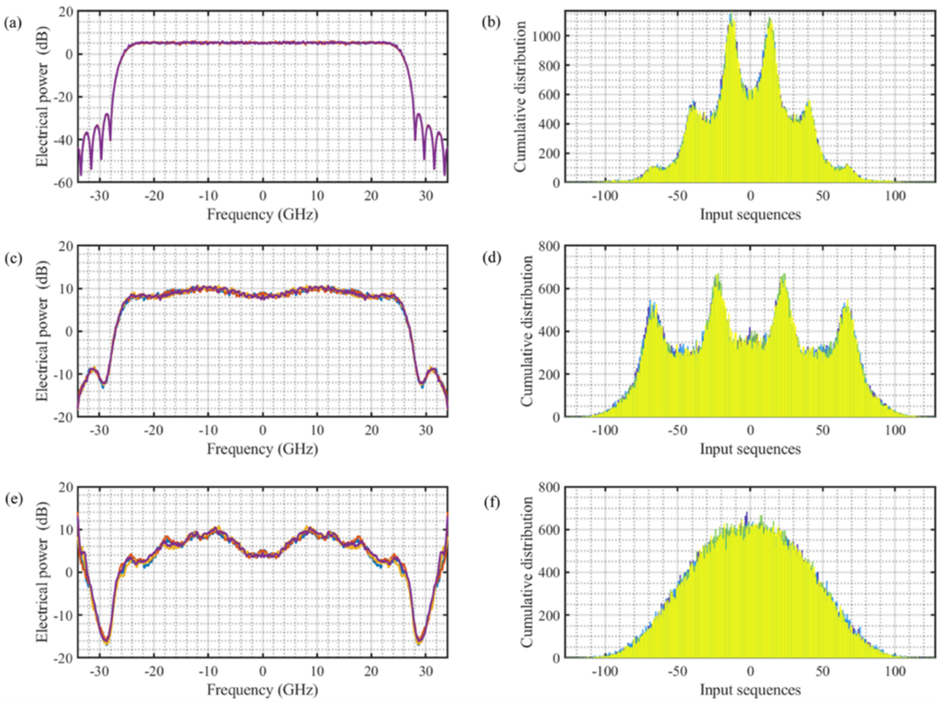

Figure 4.2: (a) The double-side spectra of transmitted PCS-64-QAM signal of the dual-polarized/ IQ channels with the entropy of 5.5 at 51.12 GBaud; (b) The input cumulative distribution histogram of the input 4 real-value (XI, XQ, YI, and YQ) signals; (c) The double-side spectra and (d) the input cumulative distribution histogram of corresponding transmitted pseudo-16-QAM signal mapped from Fig. 6(a) and Fig. 6(b), respectively; The pre-emphasized and quantified (e) double-side spectra and (f) cumulative distribution histogram of the 4 real-value pseudo-16-QAM signal processed from Fig. 6(c) and Fig. 6(d), respectively.

tion histogram of the sequence with PCS-64-QAM format. Then, the signal is further encrypted, which is mapped as a pseudo-m-QAM format. Here, the encrypted format is chosen and demonstrated in the order of 4, equivalent to m equal to 16. The double-side spectrum of the pseudo-16-QAM encrypted signal is shown in Fig. 4.2(c), where the envelope fluctuates slightly. A 16-QAM-liked cumulative distribution histogram is given in Fig. 4.2(d). The entropy of the PCS signal cannot be estimated in this step from the spectra and cumulative distribution histogram at all. In addition, for further converting the pseudo-16-QAM signal into a form suitable for an 80-km coherent transmission channel, pre-emphasis and quantization are implemented. Then the spectra in Fig. 4.2(e) and the corresponding cumulative distribution histogram in Fig. 4.2(f) appear, respectively.

4.3.2 Characterization of PCS-link without encryption

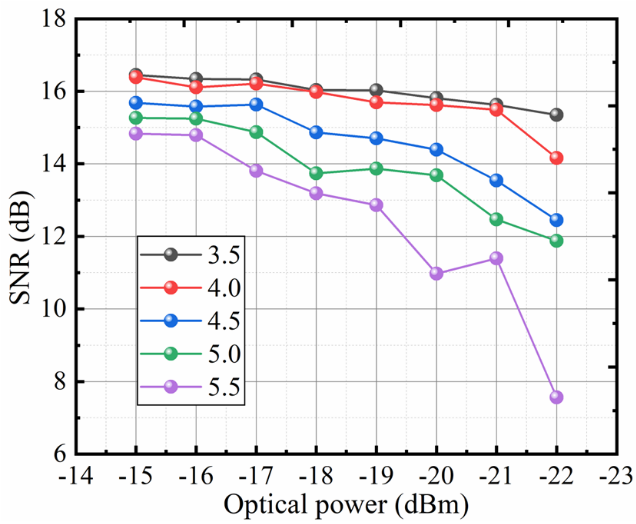

Figure 4.3: The average SNR distribution of single PCS-64-QAM ONU at 1560 nm with the entropy varying from 3.5 to 5.5 and the ROP from -15 dBm to -22 dBm (entropy interval: 0.5).

In this section, we evaluate the PCS link performance without encryption for a single legitimate receiving ONU. In a chaos-free encrypted channel, the modulation format is easily inferred and the entropy of the signal can be calculated from the intercepted frame sequence. Therefore, the information frame is exposed to eavesdropping users without encryption. For a specific legal ONU, the receiving characteristics generally distinguished from other ONU groups are usually determined by the wavelength. Compared with other ONUs in the same group, the limitation of communica-

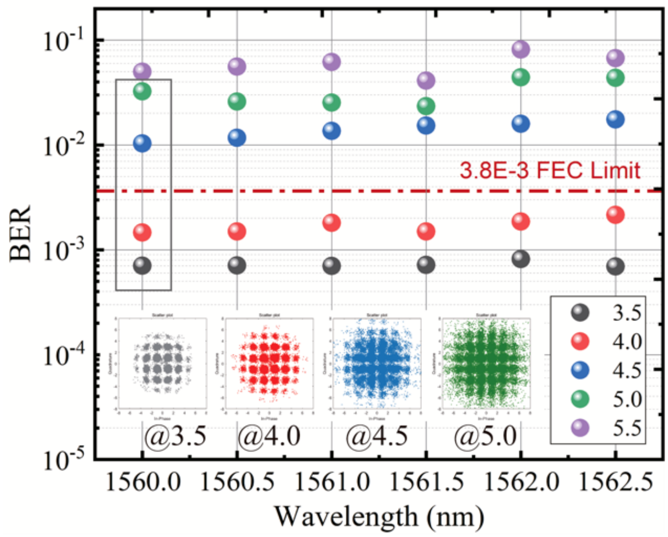

Figure 4.4: The average BERs of multiple PCS-64-QAM ONUs at a wavelength from 1560 nm to 1562.5 nm with the entropy varying from 3.5 to 5.5 (entropy interval: 0.5) at ROP of -15 dBm. (Inset: the corresponding constellation diagrams at the entropy of 3.5, 4.0, 4.5, and 5.0, respectively.)

tion performance is usually determined at the splitting power level, and data packets are allocated through different time slots by TDM.

The following experimental results are captured at a baud rate of 34.08 GBaud, corresponding to a line rate of 408.96 Gbps with dual polarization states. The link is evaluated at the entropies varying from 3.5 to 5.5 with an interval of 0.5. Fig. 4.3 is the relation between average SNR distribution and ROPs with various entropies of a PCS-64-QAM link for a single legal ONU group at 1560 nm. The SNR values decrease with increasing entropy and also with decreasing ROP. Without pseudo-*m*-QAM mapping, the SNR of links with different entropy is obviously layered, depending on the PAPR and other characteristics of the signals. Fig. 4.4 is the evaluation of communication performance for the PCS-64-QAM links for multiple legal ONU groups at the ROP of

-15 dBm. The inset figures in Fig. 8 are the PCS constellation diagrams at the entropies of 3.5, 4.0, 4.5, and 5.0, respectively, circled by a grey box at the ROP -15 dBm.

4.3.3 Characterization of encrypted pseudo-16-QAM-link for single ONU

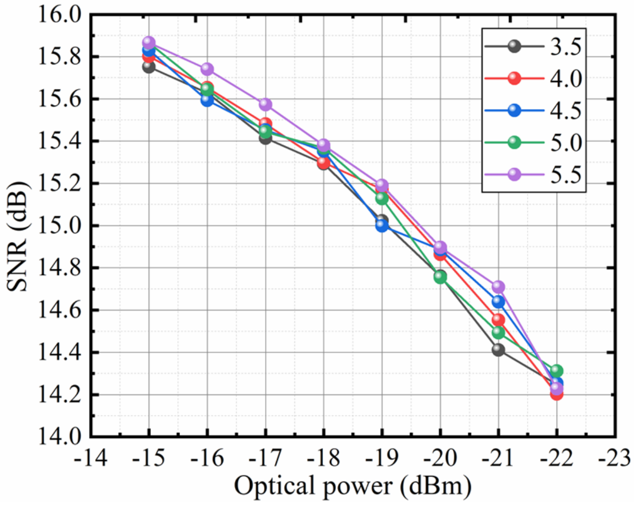

Figure 4.5: The average SNR distribution verse ROP of single encrypted pseudo-16-QAM ONU with the entropy varying from 3.5 to 5.5.

The flexible rates can be obtained with regulated entropy of the PCS-64-QAM sequence before mapping the bits as the pseudo-16-QAM format for a specific encrypted link. For a single legal ONU, its entropy/rate is unique relative to the key which can be obtained from the codebook one-to-one correspondence. The legal ONU enters the chaotic system through the initial value key to obtain the truncated chaotic sequence. Generally, in our designed WDM-CPON architecture, the flexible rate is facilitated by the ONU according to a question-and-answer mechanism. The ONU located downstream actively sends the request signaling to adjust the link data rate to the OLT located upstream through the uplink, while the OLT responds by adjusting the down-

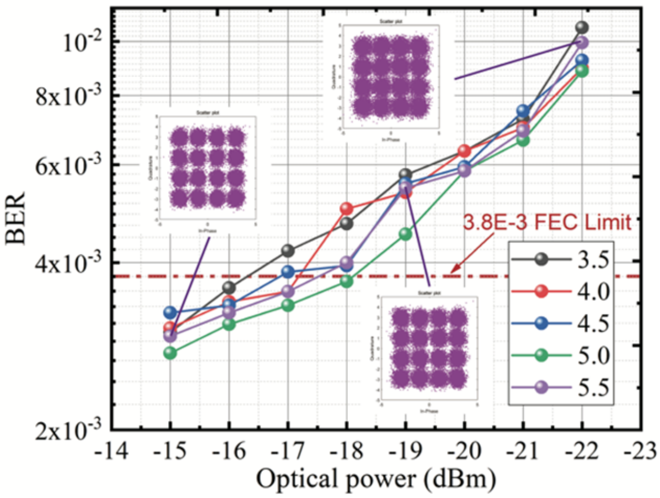

Figure 4.6: The average BERs verse ROP of multiple encrypted pseudo-16-QAM ONUs with the entropy varying from 3.5 to 5.5. (Inset: the constellation diagrams at the entropy of 5.5 and the ROP of -15 dBm, -19 dBm, and -22 dBm.)

link rate after receiving the ONU signaling. The communication and encryption performances of a legal ONU are characterized by varying ROP from -15 dBm to -22 dBm. Then, the scenarios of legal and illegal ONUs are also compared at the entropy of 5.5 at 51.12 GBaud and different ROPs.

Figure 4.5 is the average SNR distribution verse ROP of a single legal ONU under different entropy values. With the ROP decreasing from -15 dBm to – 22 dBm, the average SNRs also decrease from $\sim$ 15.8 to $\sim$ 14.2. The signal sequences with different entropy values all show similar distributions and trends, due to the same encrypted pseudo-16-QAM format. In addition, the corresponding average BERs are presented with the entropy varying from 3.5 to 5.5 in Fig. 4.6. Due to the overlapping distribution ranges, one can be selected as the analysis object. When the entropy is 5.5, corresponding to the net rate of 348.12 Gbps, encrypted transmissions can be achieved at the ROPs from -15 dBm to -18 dBm with the BERs of 2.6×10^{-3}, 2.9×10^{-3}, $3.1 \times$

10^{-3} and 3.6×10^{-3}, respectively. Furthermore, the gradually blurred constellation diagrams at the ROPs of -15 dBm, -19 dBm, and -22 dBm are also shown in the insets, respectively.

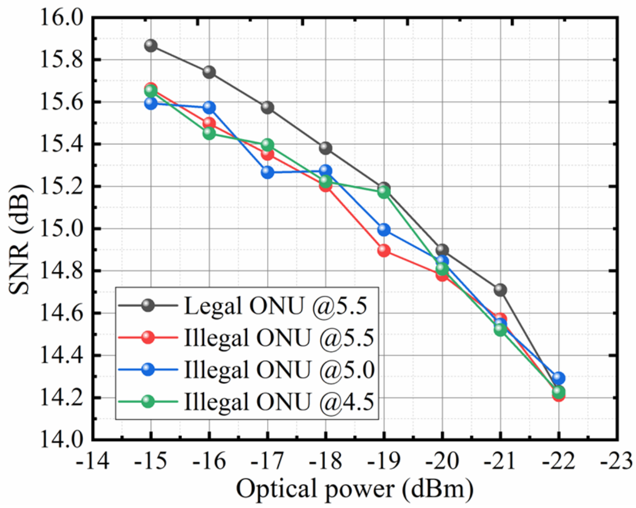

Figure 4.7: The average SNR verse ROP for legal ONU and illegal ONU when the decryption is correct and incorrect.

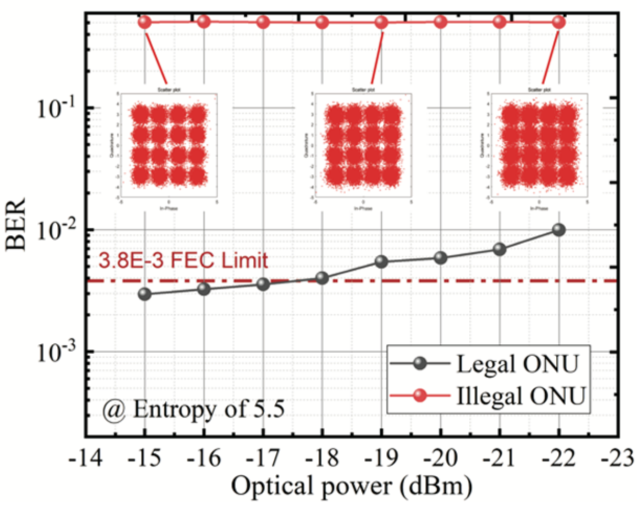

Figure 4.8: The average BERs verse ROP for legal ONU and illegal ONU when the decryption is correct and incorrect. (Inset: the pseudo-16-QAM constellation diagrams at the entropy of 5.5 and the ROP of -15 dBm, -19 dBm, and -22 dBm.)

Figure 4.7 is the average SNR distribution of illegal ONUs at the entropy of 4.5, 5, and 5.5 with the ROP varying from -15 dBm to -22 dBm, further compared with an SNR curve of legal ONU with the entropy of 5.5, extended from the result in Fig. 4.5. Here, illegitimate users may be eavesdroppers, or they may be sent to the wrong ONU destination, but none of them have the correct chaos key. Illegal eavesdroppers have no codebooks. However, the ONU that obtains information incorrectly due to incorrect link configuration cannot foreknowledge the value of entropy, and cannot find the key (the initial value of the chaotic system startup) from the large encryption space in the codebook. For the coherent link from the OLT to multiple ONUs, whether it is legal or not does not change the characteristics of the channel. Legal ONUs and illegal ONUs show almost similar average SNR distributions in the same chaotic mapping encryption with a specific m value. Fig. 4.8 further presents the corresponding average BERs curves and constellation diagrams, taking the entropy of 5.5 as an example. The legal ONU with the key can decrypt the ciphertext into the plaintext, while the BER of the illegal ONU without the key is around 0.5. For legal ONUs and illegal ONUs, the channel transmission characteristic represented by average SNRs in Fig. 4.7 is very similar, since the SNRs are evaluated before the decryption. The received pseudo-16-QAM constellation diagrams are almost identical, which gradually becomes blurred as the ROP decreases from the inset constellation diagrams at -15 dBm, -19 dBm, and -22 dBm in Fig. 4.8, respectively. However, the legal ONU can decrypt the original bit data stream, while the illegal ONU cannot know the key and obtain the entropy information. This experimental result holds not only for illegal ONUs but also for eavesdroppers without the key of chaotic sequence.

Table 4.3: The performances of encrypted pseudo-16-QAM link with entropy changed at 0.5 intervals at -15 dBm ROP and 51.12 GBaud.

	Entropy	3.5	4.0	4.5	5.0	5.5
Flexible rate	Line Rate without Encryption	408.96 Gbps at 34.08 GBaud @PCS-64-QAM				
	Line Rate with Encryption	408.96 Gbps at 51.12 GBaud @Pseudo-16-QAM				
	Net rate (Gbps)	211.80	245.88	279.96	314.04	348.12
x-pol. State	SNR (dB)	15.85	15.87	15.86	15.89	15.90
	BER	2.9×10^{-3}	2.7×10^{-3}	2.8×10^{-3}	2.3×10^{-3}	2.6×10^{-3}
y-pol. State	SNR (dB)	15.65	15.73	15.80	15.84	15.83
	BER	3.1×10^{-3}	3.4×10^{-3}	3.7×10^{-3}	3.2×10^{-3}	3.3×10^{-3}

Table 4.4: The performances of encrypted pseudo-16-QAM link with entropy changed at 0.1 intervals at -15 dBm ROP and 51.12 GBaud.

	Entropy	4.5	4.6	4.7	4.8	4.9
Flexible rate	Line Rate without Encryption	408.96 Gbps at 34.08 GBaud @PCS-64-QAM				
	Line Rate with Encryption	408.96 Gbps at 51.12 GBaud @Pseudo-16-QAM				
	Net Rate (Gbps)	279.96	286.776	293.592	300.408	307.244
x-pol. State	SNR (dB)	15.86	15.82	15.74	15.70	15.75
	BER	2.8×10^{-3}	3.0×10^{-3}	2.9×10^{-3}	3.0×10^{-3}	2.7×10^{-3}
y-pol. State	SNR (dB)	15.80	15.56	15.54	15.48	15.57
	BER	3.7×10^{-3}	3.6×10^{-3}	3.7×10^{-3}	4.2×10^{-3}	4.7×10^{-3}

In Tab. 4.3 and Tab. 4.4, we show the details of the tunable rate changing and the communication performances of each polarized component, to further present the stable realization across a wide entropy tunable range from 3.5 to 5.5 with 0.5 or 0.1 tunable intervals. At 51.12-GBaud, an interval of 0.5 from the entropy of 3.5 to the entropy of 5.5 corresponds to the rate change from 211.80 Gbps 348.12 Gbps (136.32-G tunable range) for dual-polarized encrypted links with 27.26-Gbps interval. While at the interval of 0.1 from the entropy of 4.5 to entropy of 4.9, the data rate changes from 279.96 Gbps to 307.244 Gbps with a minimum dual-polarized 6.816-Gbps step size. Tab. 4.3 shows the detailed communication performances of the x-polarized branch and the y-polarized branch corresponding with the rate changing with an interval of 17.04 Gbps, respectively. Tab. 4.4 shows similar results with entropy ranging from 4.5 to 4.9 with an interval of 0.1. All the SNR values are at the same level between 15 and 16. The BER performances of x-polarized branches are slightly better than the y-polarized branches for a specific ONU at all entropy values. This may be due to inherent defects in the optics components used in the coherent transmission system. Almost all the BERs of y-polarized branches are lower than the FEC limitation. However, at the entropies of 4.8 and 4.9, the BERs of y-polarized branches are 4.2 × 10^{-3} and 4.7 × 10^{-3}, which are slightly higher than the 7% FEC threshold of 3.8 × 10^{-3}. The corresponding pseudo-16-QAM constellation diagrams of all the polarized components show similar 16-QAM distributions, which further show a realization of confidential transmission crossing a wide entropy tunable range.

4.3.4 Characterization of encrypted pseudo-16-QAM-link for multiple ONU groups

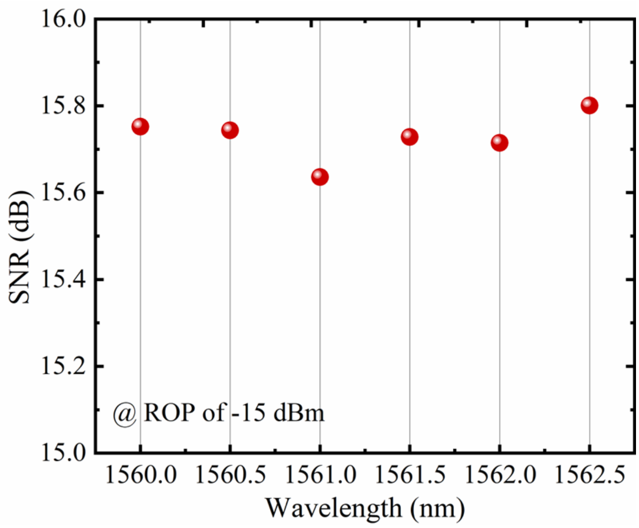

Figure 4.9: The average SNR distribution versus different wavelengths for multiple encrypted pseudo-16-QAM ONUs with the entropy of 5.5 at -15 dBm.

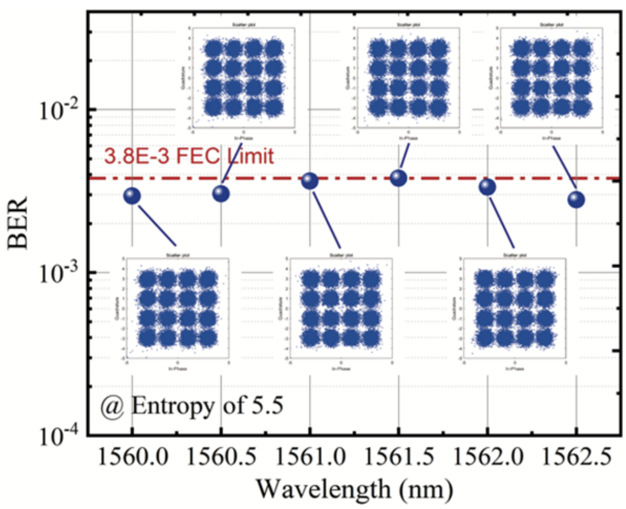

Figure 4.10: The average BERs versus different wavelengths for multiple encrypted pseudo-16-QAM ONUs with the entropy varying from 3.5 to 5.5 at -15 dBm. (Inset: the constellation diagrams at the different wavelengths.)

In the WDM-CPON experimental setup, different ONU groups are distinguished by tuning the wavelength from 1560 nm to 1562.5 nm with a 0.5 nm interval. Then, the ONUs within a single ONU group is divided by further splitting the ROP. Here we compare the performance of ONUs between groups rather than within groups. The section shows the stability of communication performances among different ONU groups with 6 carrier wavelengths. The average SNRs and BERs versus different wavelengths are shown in following Fig. 4.9 and Fig. 4.10, respectively. As shown in Fig. 4.9, using 6 different wavelengths for transmission, the average SNRs are all distributed around 15.7 with an entropy of 5.5 and an ROP of -15 dBm at 51.12 GBaud. The confidential transmissions with the pseudo-16-QAM format are achieved for different ONU groups within the FEC limitation over an 80-km SSMF. The corresponding BERs of 6 different wavelengths are further shown in Fig. 4.10, with the inset figures of the constellation diagrams. The experiment confirms that the chaotic encryption sequence can achieve relatively stable results for 6 different ONU groups at different carrier wavelengths in the proposed WDM-CPON framework.

4.3.5 Characterization of different pseudo-*m*-QAM links

The proposed chaotic encrypted method based on pseudo-m-QAM mapping can be adjusted according to the system performance, where the m value can be 2 (binary phase-shift keying, BPSK), 4 (quadrature phase-shift keying, QPSK), 8 (8-QAM), 16 (16-QAM), . . . , etc. Limited by a $\sim$ 30-GHz modulation bandwidth and relatively low PAPR tolerance of the coherent transmission platform, the m value is appropriately chosen to be 16 with a baud rate from 34.08 GBaud to $\sim$ 51.12 GBaud. However, in

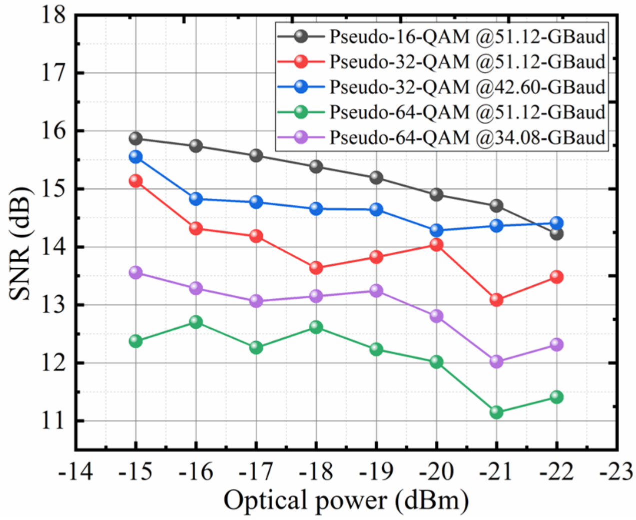

Figure 4.11: The average SNR distribution of different pseudo-m-QAM transmissions with m values equal to 16, 32, and 64 with corresponding data rates at 1560 nm at the entropy of 5.5.

a transmission platform with better performance, including higher modulation bandwidth, better linearity, and stronger PAPR tolerance, the value of m can be arbitrarily selected to suit the optical channels in specific scenarios. Within the 7% hard-decision FEC limitation, a pseudo-16-QAM encrypted transmission is achieved at -15 dBm over an 80-km SSMF. While the formats of pseudo-32-QAM and pseudo-64-QAM fail to meet the 7% hard-decision FEC threshold. Therefore, next, an experiment is designed to evaluate the performance of different m values over the same coherent transmission platform under the same 400-Gbps line rate. For the pseudo-32-QAM transmission link, if the line rate is to be equivalent to 400 Gbps (Equivalent to pseudo-16-QAM at 51.12 GBaud), the link baud rate needs to be readjusted to 42.60 GBaud. For the pseudo-64-QAM transmission link, the baud rate needs to be readjusted to 34.08 GBaud to adapt 400-Gbps line rate (Equivalent to pseudo-16-QAM at 51.12 GBaud).

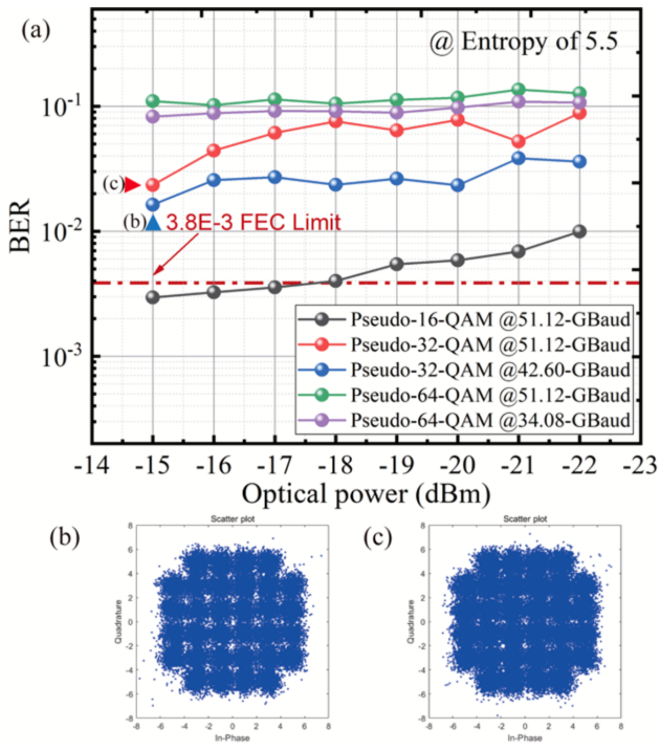

Figure 4.12: (a) The average BERs of different pseudo-m-QAM transmissions with m values equal to 16, 32, and 64 with corresponding data rates at 1560 nm at the entropy of 5.5. The constellation diagram of pseudo-32-QAM transmission with the baud rate of (b) 42.60 GBaud and (c) 51.12 GBaud, respectively.

In Fig. 4.11, the average SNR distributions of different pseudo-m-QAM mapping-based encrypted links are presented with different baud rates, which can then be compared under the same 400-Gbps line rate. With the decrease of ROP, the SNR generally shows a decreasing trend. Among them, the trends of pseudo-32-QAM at 42.60 GBaud at 51.12 GBaud are relatively uneven. With the modulation order increasing from 4 (16-QAM) to 6 (64-QAM), the average SNRs overall decline at all ROPs from -15 dBm to -22 dBm. Therefore, this SNR range provided by the coherent system over 80-km link is too noisy for the transmitting formats of 32 QAM and 64 QAM, which leads to imperfect DSP and cannot fully reflect the channel quality. In Fig. 4.12, the BER performances of different pseudo-m-QAM links are shown. Only the average BERs of pseudo-16-QAM links can achieve a performance lower than the FEC threshold of 3.8×10^{-3}. While the average BERs of pseudo-32-QAM and pseudo-64-QAM with different baud rates are all over the FEC limitation, due to larger PAPR, bandwidth, and SNR requirements. The corresponding constellation diagrams of the pseudo-32-QAM with the baud rate of 42.60 GBaud and of 51.12 GBaud are presented in Fig. 4.12(b) and Fig. 4.12(c), respectively. With the baud rate of the pseudo-32-QAM link increasing from 34.08 GBaud to 51.12 GBaud, the constellation diagram becomes blurrier.

4.4 TDMA Frame Design and Demonstration of Encrypted Coherent Fronthaul with Flexible and Monitored Rate

4.4.1 Introduction

To support the future Centralized Radio Access Network (C-RAN) in beyond 5th generation mobile networks (B5G), an ultra-100G rate-flexible and secure mobile fronthaul (MFH) scheme is expected in the future [99, 100]. For the realization of a flexible rate, the probabilistic constellation shaping-based (PCS-based) modulation format has tunable spectral efficiency (SE) [101]. By adjusting the entropy of the signal, different bandwidth resources can be allocated to different MFHs to achieve rate adaptation [102]. In addition, digital signal processing (DSP) can design initial value sensitive dynamical systems and further generate long sequences for chaotic encryption [103].

As standard solutions for MFHs, time division multiple access (TDMA) or frequency division multiple access (FDMA) can be used to combine data sequences with different formats into the same frame [104, 105]. For TDMA, the PCS-format sequence can be placed in the preamble sequence, while for FDMA, several subcarriers can be selected to load the PCS-format sequence. The selected small part of the transmitted frame is mapped into PCS format and the rest of the complete information frame is chaotically encrypted. The intra-frame combining is finished through a fast normalized cross-correlation (NCC) coefficient template matching algorithm [26].

4.4.2 Principles, Architecture and Experimental Setup

As shown in Fig. 4.13(a), the schematic of the TDMA frame design is illustrated for rate-flexible coherent MFH. The original frame is divided into two parts including an encrypted frame and an identification frame, which will be transmitted together. Encrypted frames will be encrypted and further mapped into a pseudo-16-quadrature amplitude modulation (pseudo-16-QAM) format, while identification frames will maintain the original PCS-64-QAM format with a specific entropy value. For a TDMA transmission frame, the preamble bits can be obtained by arbitrarily copying the partial transmission sequence. We set the length of the preamble sequence without encryption to 1/12 of the length of the message sequence with encryption.

At the receiver (Rx.), the Rx. DSP includes synchronization and downsampling to obtain the original frame sequence, which is further divided into two parts. The preamble enters the identification process in the upper part of the digital image processing flow of Fig. 4.13(b), which mainly includes two cross-correlation DSP operations over the generated PCS constellation diagrams with various entropies. In our experimental setting, the entropies are only taking a value among 3.5, 4, and 4.5. The fast NCC matching algorithm occupies an important position in the field of image matching, with a certain robustness to noise and the changing of image brightness. In Fig. 4.13(b), the digital image processing flow of the NCC calculation can be divided into two parts at the receiver. The first part is to monitor if the entropy/rate is changing by cross-correlating the constellation diagram of the last moment, and the other part is to monitor the value of entropy/rate by cross-correlating with a predetermined stored image mean template. According to the corresponding relationship between the entropy and the initial value of the chaotic system in the codebook, the long key is generated and used to decrypt with another part of the frame sequence.

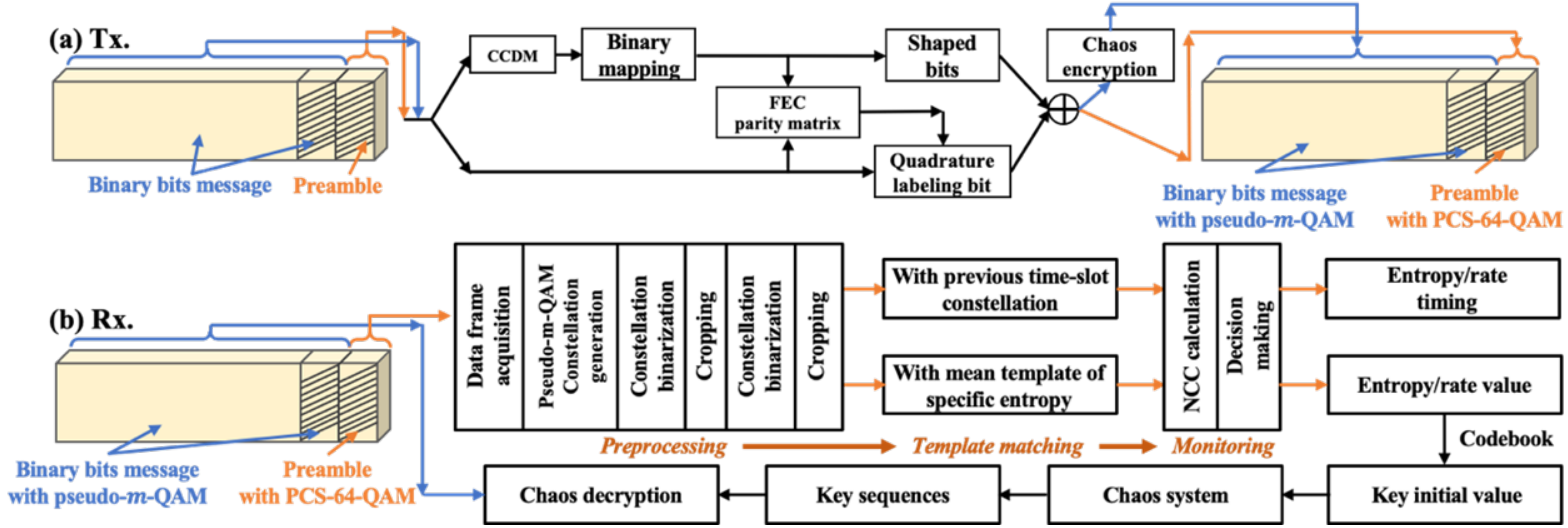

Figure 4.13: The working principle of transmitter frame structure: (a) Schematic of Tx. frame processing with combining PAS and chaotic encryption process; (b) Schematic of Rx. frame processing including constellation diagram template matching, frame synchronization, a look-up table (entropy value and initial value of chaotic system), and chaotic decryption.

4.4.3 Results and Discussions

As shown in Fig. 4.14(a), the original spectra of the four signal streams can be obtained by fast Fourier transform (FFT), which are highly overlapping in the frequency domain with a 50.12-GHz double-side bandwidth. Fig. 4.14(b) presents the result of the cross-correlation operation between an input 1/4 clipped gray constellation diagram with 3.5 entropy and a complete matching constellation diagram template with the same 3.5 entropy. A normalized peak of 0.85 value can be obtained which is higher than the other matching cross-correlation peaks with entropies of 4 or 4.5. From the size of the relative peak, we can judge the entropy value and thus get the rate [8]. Then, in Fig. 4.14(c) and Fig. 4.14(d), the communication performances are shown over 10-km standard single mode fiber (SSMF) at a receiving optical power (ROP) from -8 dBm to -24 dBm after chaotic decryption. Regardless of whether it is a legal or illegal user, the distribution trend of the signal-to-noise ratio (SNR) is similar and decreases with the decrease of the optical power from $\sim$15 dBm to$\sim$13 dBm. However, the illegal user has no way to obtain the corresponding chaotic key from entropy and the original data bits cannot be deciphered, resulting in a high bit-error rate (BER). At the ROP from -8 dBm to -22 dBm, the net data rate from 225.39 Gbps to 281.62 Gbps can be achieved with corresponding entropies from 3.5 to 4.5, and a tunable interval is 0.5. Insets are two PCS constellation diagram examples with the entropies of 3.5 and 4.5 at -8-dBm ROP, with BERs of 6.97 × 10^{-4} and 8.72 × 10^{-4}, respectively.

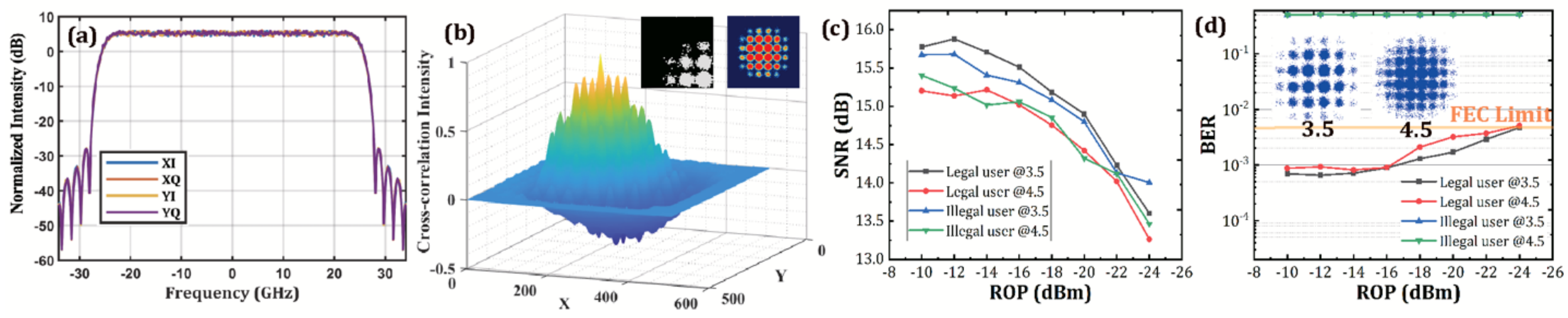

Figure 4.14: (a) The double-side spectra of transmitted PCS-64-QAM signal of the dual-polarized/ IQ channels with the entropy of 4.5 at 50.12 GBaud. (b) The result of the cross-correlation operation with 3.5 entropies is displayed as a surface with the highest peak. For the legal and illegal users, (c) the SNR and (d) the BER versus ROP with entropies of 3.5 and 4.5. (Inset: The corresponding constellation diagrams at -8-dBm ROP).

4.5 Section Summary

This section shows how we propose to perform dynamic encryption at the physical layer in a rate-flexible high-speed long-distance access network system.

Chapter 5

Service Fairness in CPON

5.1 Overview and Research Status

Above the physical layer, as an important business indicator for operators, fairness in user service quality involves how to fairly allocate network resources to meet the needs of all users equally [106, 107, 108]. Generally, the wider bandwidth and received optical power (ROP) guarantee of the physical layer means a faster and more stable data rate directly contributing to the volume of the throughput of transmission control protocol (TCP) of the network layer and the applications of the application layer [109]. The division of wideband schemes to provide various Internet services for access users is intrinsically the de-facto standard of congestion control protocols. User fairness control of PON in the network layer usually includes considerations of a series of figures of merit (FOM) such as latency, jitter, packet loss rate, quality of service (QoS), reliability, security, priority, and traffic management [110]. For example, QoS is a set of joint quantitative and qualitative network performance parameters and comprehensive concepts used to measure and describe the performance of network services, various aspects of service delivery, and the ability of the network to provide when meeting specific requirements [111, 112]. The latency, as another key factor, is strongly related to the satisfaction of the access user. Delay fairness ensures that all users on the network have relatively consistent response times to provide consistent and reliable services [113].

As for the physical layer, the server fairness discussions and demonstrations are still few, but it is the bottom line to ensure basic performance. In the traditional TDM-PON standard, using the time-slot fair allocation (TFA) algorithm improves the time slot density or priority of data frames to achieve fairness on the user side [114]. In time-wavelength division multiplexing (TWDM)-PON, the wavelength fair allocation (WFA) algorithm can also be used to effectively allocate wavelength routes to achieve an effective configuration of wavelength resources [115]. In addition, in many schemes based on frequency domain division, fairness of bandwidth resource allocation is the most common consideration. In PON based on digital subcarrier multiplexing or OFDM, the bandwidth combination of subcarriers can be divided by time or allocated on demand [116, 117, 118]. Bandwidth allocation fairness ensures that each user has a reasonable share of bandwidth on the network to meet their communication needs and respond to real-time feedback. Recent digital-domain power-division non-orthogonal multiplexing access (NOMA) shows the potential to solve the fairness service problem through signal superposition coding (SC) and power factor allocation [119, 120]. However, as far as we know, no work has discussed user service fairness, proposed solutions, and been demonstrated on the physical layer of coherent PON.

In this work, we propose and demonstrate a dual-polarized (DP) 200-Gbps coherent PON at C-band with two far-near access users with polarization division multiplexing (PDM) and quadrature phase-shift keying (QPSK). The signals to two destinations are overlapped in the time domain at a carrier of the same wavelength channel and then are distributed simultaneously. The digital signal processing (DSP) of SC and successive interference cancelation (SIC) are designed and embedded at the transmitter and receiver, respectively. In the case of different power allocations, edge users can obtain performance improvements as the superimposed power allocation ratio (PAR) increases. Therefore, by optimizing the PAR value, both near-center users with 10-km path loss and another 20-/30-/40-/50-km and 1: 4-/1: 8-/1: 16-/1: 32-/1: 64-SR far edge users can achieve a fair transmission at 200-Gbps line rate, respectively. Service fairness is further discussed in different cases and evaluated by Jain's fairness index at a fixed and flexible hard-decision forward error correction (HD-FEC) standard, and modified fairness index. The TDM-NOMA solution may provide an operational reference for the design of the next-generation coherent PON by multiplexing and superposition optimization in the power domain, where traditional quadrature amplitude modulation (QAM) over TDM-PON with unavoidable power difference cannot echo.

5.2 Issue Statement

Figure 5.1 presents three typical coherent PON architectures that evolute from NG-PON and 50-G PON, including Fig. 5.1(a) the full-tree topology, Fig. 5.1(b) the pyramid topology, and Fig. 5.1(c) the cube topology. In the rate-fixed PON downlink

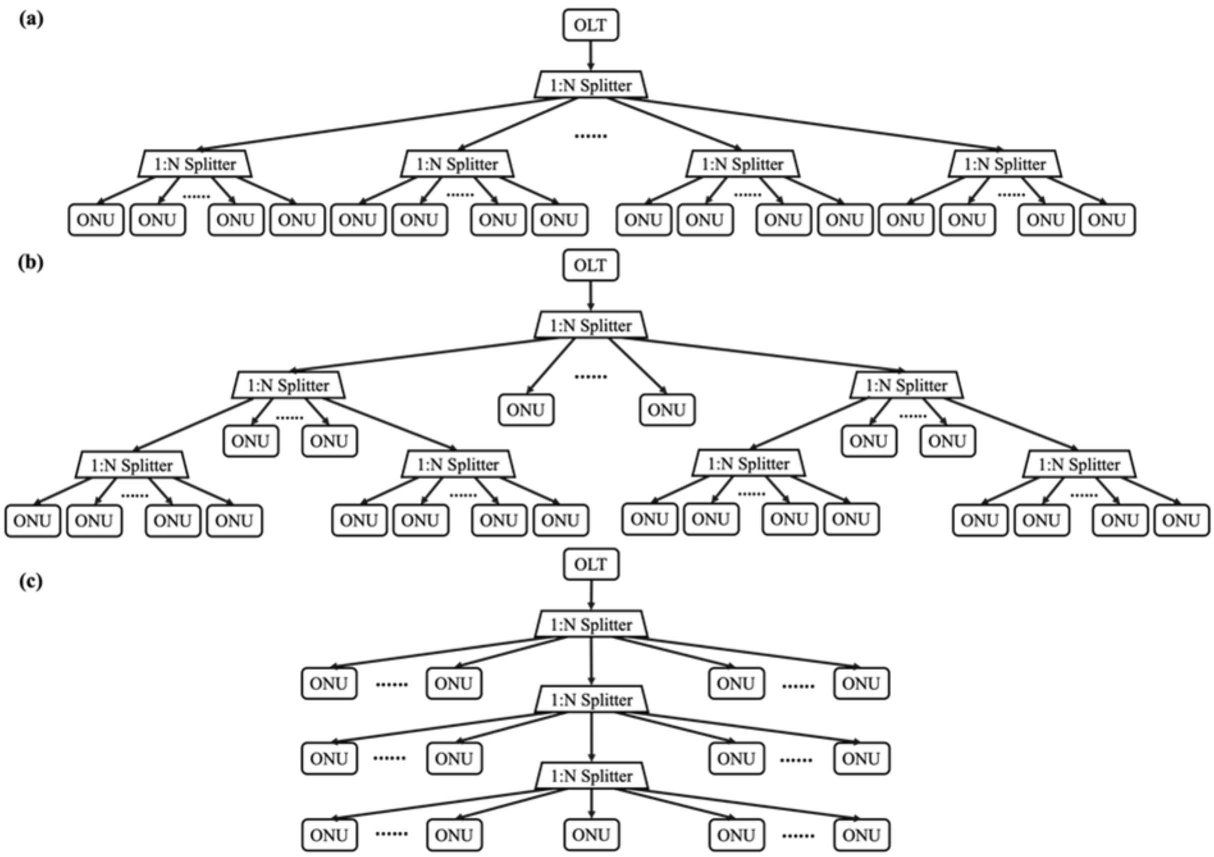

Figure 5.1: Typical architectures/ topologies of wide-coverage high-speed coherent PON: (a) full-tree topology, (b) pyramid topology, and (c) cube topology.

architecture, to ensure fairness, the overall communication performance is limited by the worst one, which usually has the longest transmission distance and the largest SR. Naturally, center users will have wider power budgets while edge users will not. In contrast, in the rate-flexible PON downlink architecture, the adaptation of modulation format, signal entropy, or spectral efficiency within a certain bandwidth changes the throughput rate, which is limited by the SNR at the receiver. The limitation further affects the central ONU that can use a high-order modulation format or high-entropy-loading format, while the edge ONU needs to reduce the entropy of information to ensure communication performance. In the full-tree structure, all the destinated power-limited ONUs have similar optimal received power due to the passing same link distance and same SR. All the access ONUs have the same power budget for receiving the signal with similar entropy. However, in the practical deployment, the double-layer or triple-layer pyramid or cube topologies shown in Fig. 5.1(b) and 5.1(c), respectively, are the more common wiring methods. In those cases, for rate-flexible PON, the center ONUs with the shortest distance and the smallest SR from OLT will have the widest rate-varying range, corresponding to the achievable data rate. The ONUs at the nearest layer from OLT also have the best bit-error performance compared with the other ONUs at the same throughput. This issue becomes apparent when the diameter of the PON coverage area exceeds 40 km and the SR exceeds 1:64 (-18 dB split loss).

Therefore, in the actual deployment of wide coverage, the OLT will be placed closer to the ONU or ONU group which requires higher performance, bandwidth, and throughput to provide more matching services. While ONUs with lower requirements for the above indicators can be placed relatively far away. However, in a more general scenario, we need to take care of all users under the coverage of the OLT to provide consistent performance services. The problem here is transformed into how to further optimize the network architecture via hardware or software to achieve service fairness between the ONU with the strongest ROP and the edge users with the weakest ROP. If this strategy becomes feasible, this solution can enable any two or any multiple ONUs to achieve fairness in resource allocation.

Table 5.1: The experimental NOMA-based CPON setup parameters and their corresponding states and specific values.

Parameter	Value
Operating Wavelength	1553.6 nm
Launch Optical Power (LOP)	0 dBm
Supported ONUs	2 $\sim$64
Min. Transmission Distance	10 km
Max. Transmission Distance	50 km
Splitter Number (1:2)	1 $\sim$3
Baud Rate	50 GBaud
Modulation Format	QPSK
Roll-off Factor	0.1
Polarization State	2
SC Users Number	2

5.3 Experimental Setup

The experimental setup shown in Fig. 5.2 adopts multiple far-near ONUs configurations but evaluates two of them with the largest received power difference. Depending on the path loss caused by the distributed fiber length and the SR caused by the passive splitter, we mainly consider and analyze the service fairness between the best and worst users in the entire network topology. The experimental implementation and the DSP flow are presented in Fig. 5.2, and the configuration can be promoted to any two or more users with ROP differences at any dense access network. In Table 5.1, the basic parameters of the power-domain NOMA-based coherent PON setup are presented with corresponding values

At the digital domain of the transmitter, two pseudo-random bit sequences (PRBS) are generated firstly for ONUs at different far-near positions and then mapped into QPSK symbols. Due to the in-phase quadrature (IQ) and dual polarization configuration, this step processes the eight-string parallel sequences of two users and performs

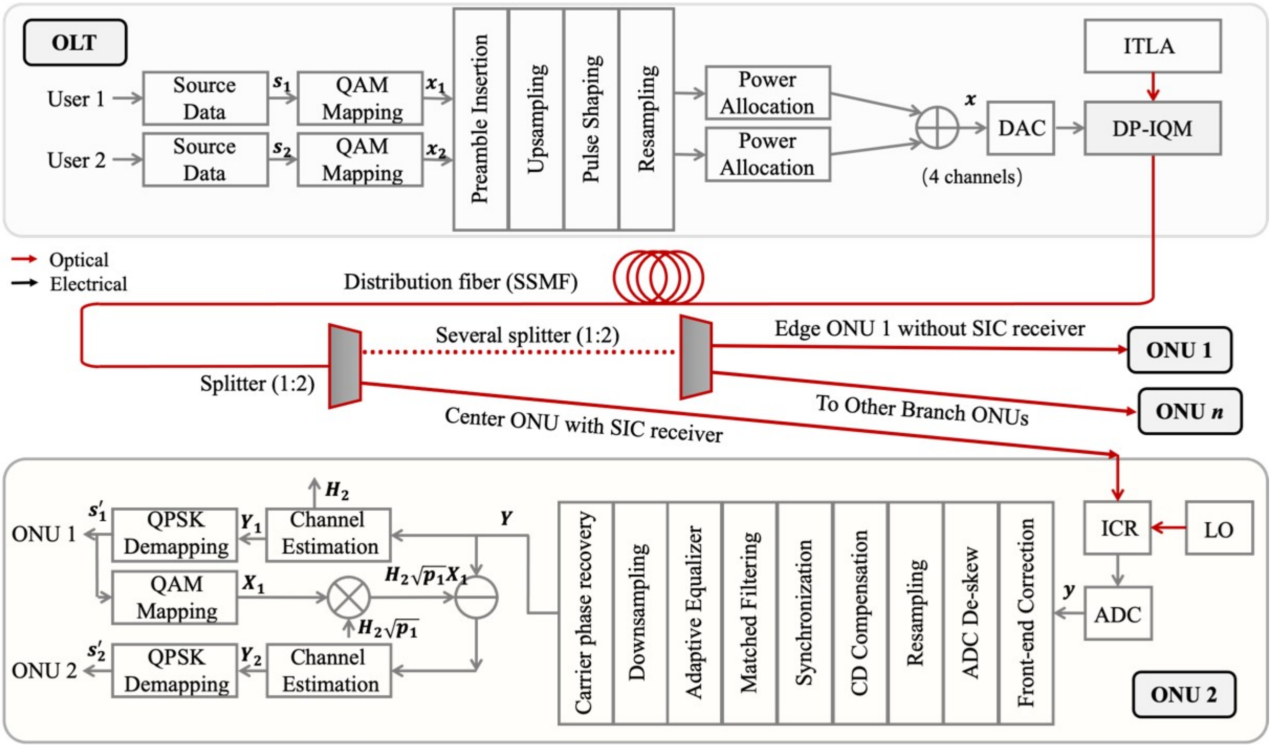

Figure 5.2: The experimental setup of the TDM-NOMA coherent PON with an OLT and two far-near ONUs, and the DSP flow including the SC operation at the transmitter and the SIC operation at the near ONU receiver.

the operations including the inserting preamble sequences, up-sampling, pulse shaping, and resampling, respectively. Here, the four sequences, represented by XI, XQ, YI, and YQ, are up-sampled to 2 *sps* and shaped by the root-raised cosine (RRC) pulse filter. Next, the SC superimposes eight sequences into four sequences to be transmitted, where the two sequences are each assigned a power coefficient and then linearly added. A digital-to-analog converter (DAC) sent 4-channels superimposed digital signals (XI, XQ, YI, and YQ) into a DP IQ modulator (DP-IQM) and then loaded into the 1553.6-nm optical carrier derived from the integrated tunable laser (ITLA). The superimposed optical signal travels along the fiber with different lengths and one or several passive splitters (1:2). It is then captured by the two far-near ONUs coherent receivers. The overall attenuation will be mainly caused by path loss, power division inside passive splitters, and coupling insertion loss. For controlling the receiver power difference over the optical distribution node (ODN), the center ONU 2 passes only a 10-km optical fiber link as well as a -3-dB power splitter, while the edge ONU 1 needs to separately pass 20-km/ 30-km/ 40-km/ 50-km optical fiber links and several power splitters with the SR from 1:4 to 1:60, respectively. These experimental configurations correspond to the actual four scenarios in practical deployment, including traditional 20-km dense access, 30-km dense access, 40-km long-reach access, and 50-km Super-PON access. A C-band variable optical attenuator (VOA) and multiple 1:2 SR passive splitters are used to set up the user cases.

The hardware configurations of the two destination ONUs are similar. A micro-integrated coherent receiver (micro-ICR), a 1553.6-nm local oscillator (LO), and an analog-to-digital converter (ADC) service as a front-end receiving module to capture the optical signal and convert it into an electrical signal. The captured electrical signal is operated as follows in turn, including front-end correction, ADC de-skew, resampling, chromatic dispersion (CD) compensation, synchronization, matched filtering, adaptive multiple-input multiple-output (MIMO) equalization, down-sampling, and phase carrier recovery. Among them, the sequence is re-sampled and down-sampled to 2 *sps* and 1 *sps*, respectively, and the MIMO equalization can be used to further estimate the channel characteristics of the corresponding ONU, which will be utilized at the following SIC operation. For the far edge ONU 1, because the relatively larger power coefficient is assigned, the center ONU 2 signal on its superposition is considered as an interference term. The above DSP is executed at the far edge ONU 1 side, the QPSK symbols are de-mapped into binary bits directly. However, for the near center ONU 2, the SIC operation based on the power division de-multiplexing module should be performed according to the descending order of power factor proportion. As shown in Fig. 3, according to the obtained $h2$ profile from the channel estimation, the SIC receiver performs the necessary coherent DSP of the superimposed symbol sequence, which is then de-mapped into the binary bit signal sequence of far edge ONU 1 over channel 2. Next, the SIC receiver reuses the receiving symbol sequence again to subtract the re-mapping QPSK sequence of the previous bit signal for far edge ONU 1, thereby finally obtaining the symbol sequence of user 2 superimposed on the AWGN introduced by channel 2 and the error propagation from the imperfect SIC. Finally, the sequence of symbols for near ONU 2 is de-mapped into binary bits and then the SINR and BER are calculated.

5.4 Results and Discussions

The results and discussion in Section 5.4 have several parts for evaluating communication performance and fairness. The following presentations include four sub-experiments with various path loss and SRs, corresponding to different user cases. Then, the fairness service is evaluated by the calculations of Jain's fairness index at a fixed and flexible FEC standard, and modified fairness index, respectively.

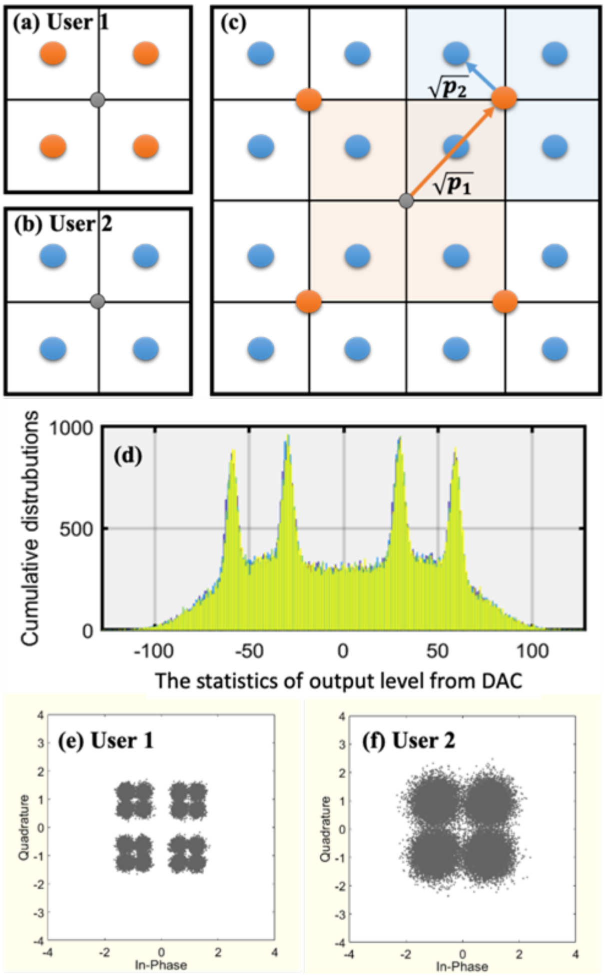

Figure 5.3: The transmitted constellation diagrams of (a) user 1 with QPSK format, (b) user 2 with QPSK format, and (c) the multiplexed NOMA. (d) The cumulative distribution histogram of the transmitted NOMA signal from the output level of the DAC with the PAR of 9. (e) (f) The received constellation diagrams of two users overlapped within a single timeslot.

5.4.1 Characterization of NOMA transmitted signals

Figure 5.3 shows the characteristics of input and output constellation mapping of NOMA with two multiplexed QPSK signals. As shown in the schematics from Fig. 5.3(a) to Fig. 5.3(c), the transmitted two QPSK symbol sequences are multiplexed and then generated a 16-QAM-like constellation diagram with full symmetry of area. According to the PAR and the system performance, in Fig. 5.3(c), the distances between the mapping point from the origin (*marked in black*) to the first user (*marked in orange*), and the mapping point from the first user to the second user (*marked in blue*) can be adjusted at SC operation. Then, an example of two ONUs with 9 PAR and the same 10-km transmission link is shown to elaborate the principle further.

In Fig. 5.3(c), at the transmitter side, a cumulative distribution histogram shows the distribution of points in the 16-QAM-like constellation diagram. The four-channel input sequences (XI, XQ, YI, and YQ) are multiplexed with two users and overlapped together. Since the power allocated to ONU 1 is 9 times that of ONU 2, it can be clearly seen that the Euclidean distance between the two peaks in the middle is much longer than the Euclidean distance between the two peaks on the left or right sides. This reflects that in the 16-QAM-like constellation diagram in Fig. 5.3(c), the blue constellation points in the four symmetrical areas are closer to the orange constellation point in the middle. While the distribution of the four blue point clusters to the origin is relatively far. A simple pilot experiment is performed here to illustrate the receiving constellation diagrams of NOMA-based coherent PON. Two sequences for two users are captured one time over a 10-km DP coherent transmission and two constellation diagrams are generated as shown in Fig. 5.3(e) and Fig. 5.3(f). As described above, the 16-QAM-like constellation for user 1 is distributed into four relatively symmetrical clusters. For user 2, it is still a regular QPSK constellation point distribution. However, it appears noisier due to the lower signal power of user 2.

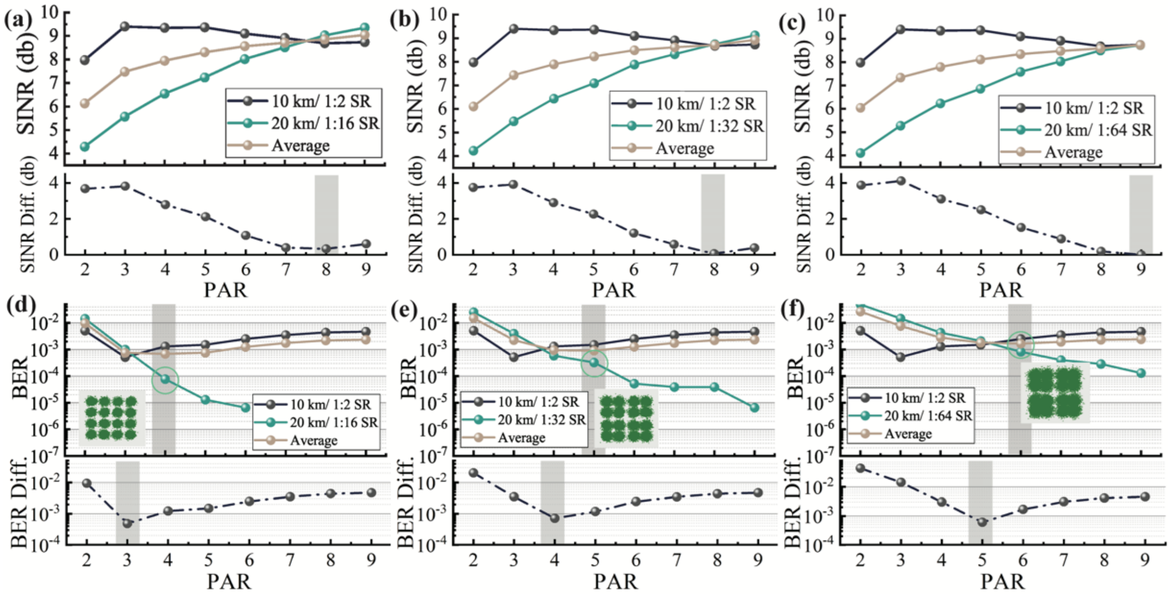

Figure 5.4: Short-reach dense access case over traditional 20-km PON range. The (a) (b) (c) SINR and (d) (e) (f) BER performances between 10-km center ONU 2 with 1:2 SR and 20-km edge ONU 1 with 1:16, 1:32, and 1:64 SR, respectively. The inserted constellation diagrams of far edge ONU 1 in (d) (e) (f) are with the PAR of 4, 5, and 6, respectively.

5.4.2 Characterization of dense access cases

Two user cases are evaluated in this section with traditional PON configuration coverages less than the maximum differential distance of 40 km, including the 20-km range PON and 30-km range PON with 1:16, 1:32, and 1:64 SR, respectively. These are the dense access scenarios.

Here, for the 10-km ONU 2 with SIC operation, the performances of the following three experimental scenarios over 30 km, 40 km, and 50 km with various SRs are similar. According to the SIC decoding process, the user interference terms from ONU 1 experience the same channel profile as the multiplexed signal to ONU 2, which does not depend on the channel conditions experienced by the TDM-NOMA signal to far

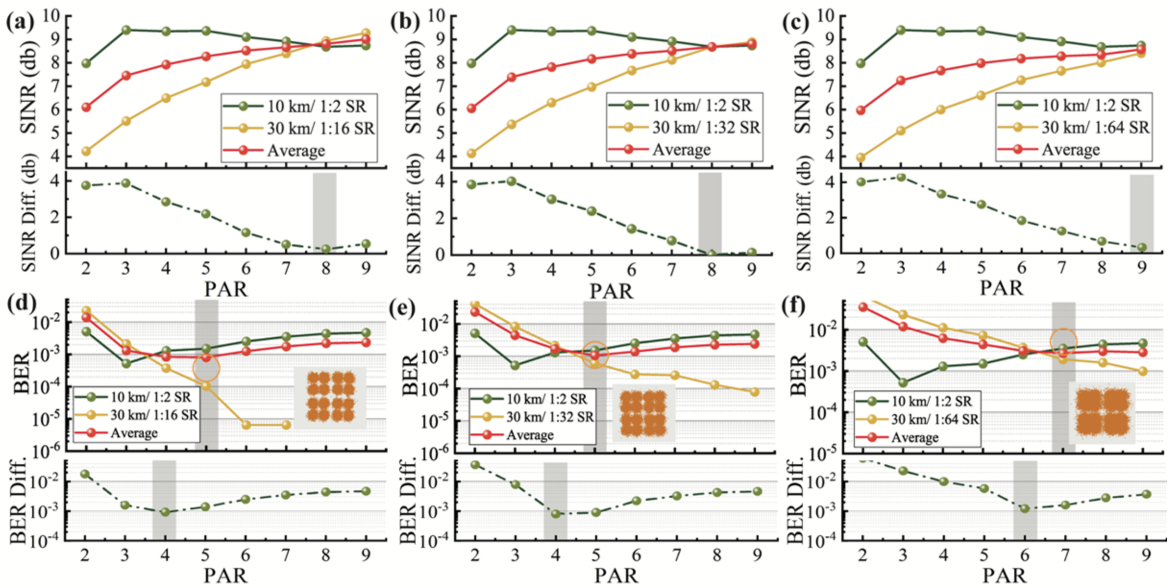

Figure 5.5: Short-reach user case over traditional 30-km PON range. The (a) (b) (c) SINR and (d) (e) (f) BER performances between 10-km center ONU 2 with 1:2 SR and 30-km edge ONU 1 with 1:16, 1:32, and 1:64 SR, respectively. The inserted constellation diagrams of far edge ONU 1 in (d) (e) (f) are with the PAR of 5, 5, and 7, respectively.

edge ONU 1, including fiber length and any number of passive splitters. From the results of multiple experiments with ONU 2 under different conditions, ONU 1 with a 10-km link and 1:2 SR have repeated almost consistent results. As PAR increases, the power allocated to near center ONU 2 decreases. The tendency of the SINR curve first increases and then decreases slowly, and reaches the maximum value of 9.3978 when PAR is 3. Under the 200-Gbps line rate, the BER also achieved a maximum value of 5.2 $\times 10^{-4}$ with a PAR of 3. The results, including the SINR and BER of near center ONU 1, are given from Fig. 5.4 to Fig. 5.7 as a comparison scale, but the experimental results will not be described repeatedly.

Fig. 5.4(a) and Fig. 5.4(d) show the SINRs and the BERs of the 10-km ONU 2 (user 2 with SIC), 20-km 1:16-SR ONU 1 (user 1 without SIC), the average values, and the differential values, respectively. The inserted constellation diagram in Fig. 5(d) shows the signal quality of 20-km 1:16-SR ONU 1 under the PAR of 4. Then, the pairs of Fig. 5.4(b) and Fig. 5.4(e), as well as the pairs of Fig. 5.4(c) and Fig. 5.4(f) show the same FOMs of the independent, average, and differential SINR and BER, and constellation point distributed performances but at the different SR of 1:32 and 1:64. Combining these three sub-cases to analyze and observe the changing trends of SINR and BER as SR increases from 1:16 to 1:64, the adjusted PAR can significantly change overall and fair performances. With the increase of the SR, the ROP is decreasing from -18.02 dBm to -21.02 dm, and then to -24.03 dBm.

From Fig. 5.4(a) to Fig 5.4(c), with a decrease of the ROP, the far edge ONU 1 needs more power allocation to achieve a similar SINR compared with the near center ONU 2. The interaction points of two SINR curves or the minimum SINR differential value will be more inclined to places with higher PAR. For the BER curve such as the green curve in Fig. 5.4(d), if no BER point is shown in the case of high PAR, it means that error-free communication is possible for far edge ONU 1. At the SR from 1:16 to 1:32 and then to 1:64, the lowest average BERs occur at PARs of 4, 5, and 6, which are 7.6 × 10^{-4}, 9.42 × 10^{-4}, and 1.8 × 10^{-3}, respectively. The minimum BER differences between two users occur at PARs of 3, 4, and 5, which are 4.8 × 10^{-4}, 7.15 × 10^{-4}, and 6 × 10^{-4}, respectively. From a physical experiment, we allocate higher power to the far-edge ONU at these PAR points, thereby achieving better fairness compared to two QPSK signals propagating independently. As the ROP difference becomes larger, the far-edge ONU needs to allocate more power, and the PAR needs to increase. The inserted constellation diagrams from Fig. 5.4(d) to Fig. 5.4(f) become more blurred and the point clustering becomes more obvious. For the 30-km access user cases with SP from 1:16 to 1:64, similar trends and analysis can be obtained from Fig. 5.5(a) to Fig. 5.5(f). The only difference from the 20-km case is that the far edge ONU introduces more 10-km path loss, resulting in higher ($\sim$1.9 dB) loss. The SINR curves from Fig. 5.5(a) to Fig. 5.5(c) follow almost the same trends compared to the results from the 20-km access user case, while the experimental available BER varies. The lowest average BERs shift to the PAR at 5, 5, and 7, with the values of 8.02 × 10^{-4}, 1.05 × 10^{-3}, and 2.7 × 10^{-3}, respectively. The fairest points are obtained when PAR is 4, 4, and 6 with the differential values of BERs being 9.26 × 10^{-4}, 8 × 10^{-4}, and 1.2 × 10^{-3}, respectively. The constellation diagrams of far edge ONU 1 are also inserted from Fig. 5.5(d) to Fig. 5.5(f).

5.4.3 Characterization of long-reach cases

Compared with the coverage of traditional PON architecture, two subsequent experiments with longer reach and smaller SR are further verified, including the user case with a maximum differential distance of 50-G PON standard of 40 km and the Super-PON user case with a differential distance of 50 km. These user cases are mainly for access applications in remote areas such as suburbs. Generally, as the access link distance increases, the number of accessed users will decrease accordingly. Similar to how the previous section was presented, we compare 40-km or 50-km far edge ONU 1 with the SR of 1:4, 1:8, and 1:16 with 10-km near center ONU 2 with the SR of 1:2, respectively.

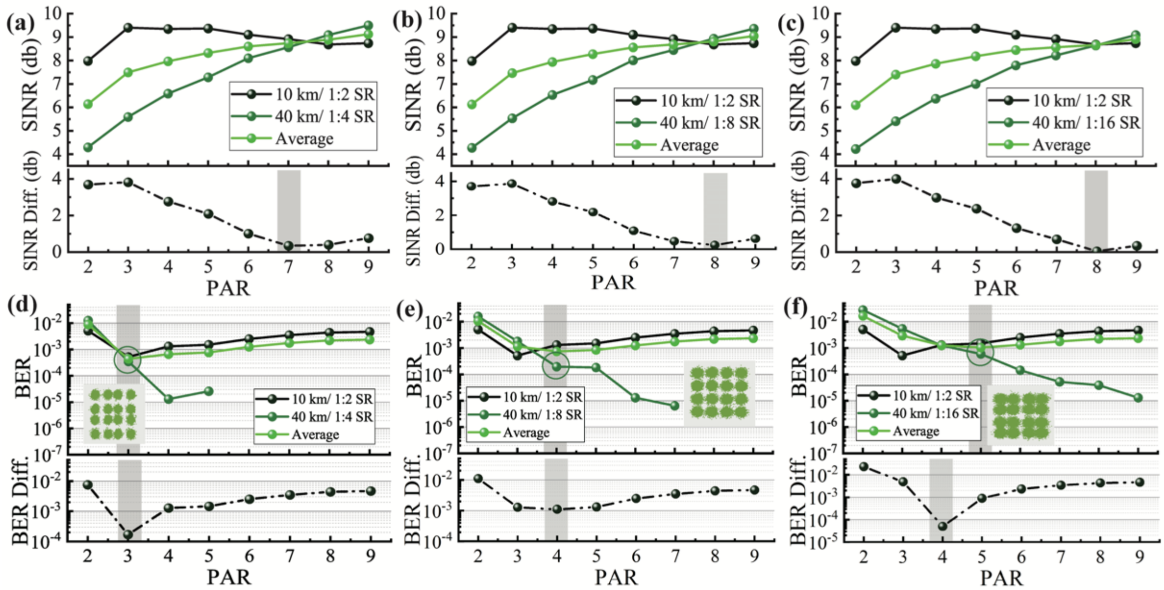

Figure 5.6: Long-reach user case over PON with a maximum differential distance of 50-G PON of 40 km and smaller SR. The (a) (b) (c) SINR and (d) (e) (f) BER performances between 10-km center ONU 2 with 1:2 SR and 40-km edge ONU 1 with 1:4, 1:8, and 1:16 SR, respectively. The inserted constellation diagrams of far edge ONU 1 in (d) (e) (f) are with the PAR of 3, 4, and 5, respectively.

For the 40-km user case, the ROPs are -15.79 dBm, -18.78 dBm, and -21.82 dBm at the SRs of 1:4, 1:8, and 1:16, respectively, while an additional ~1.9 dB path loss is added in the 50-km user case. From Fig. 5.6(a) to Fig. 5.6 (c), the same trend is observed. The smallest SINR difference values were obtained when PAR was optimized at 7, 8, and 8, respectively. When the SR of far edge ONU 1 is 1:4, the optimal average BER and differential BER are both obtained when the PAR is 3, which are 4.35 × 10^{-4} and 1.69 × 10^{-4}, respectively. When the SR increases to 1:8, both of the optimal PAR values move to the right 4. The optimal average BER and differential BER are 7.47 × 10^{-4} and 1.11 × 10^{-3}, respectively. In Fig. 5.6(e), the 16-QAM-like constellation diagram of far edge ONU 1 becomes a standard 16-QAM constellation diagram, while the constellation diagram in Fig. 5.6(d) at PAR of 3 has a more dispersed cluster. When the SR is

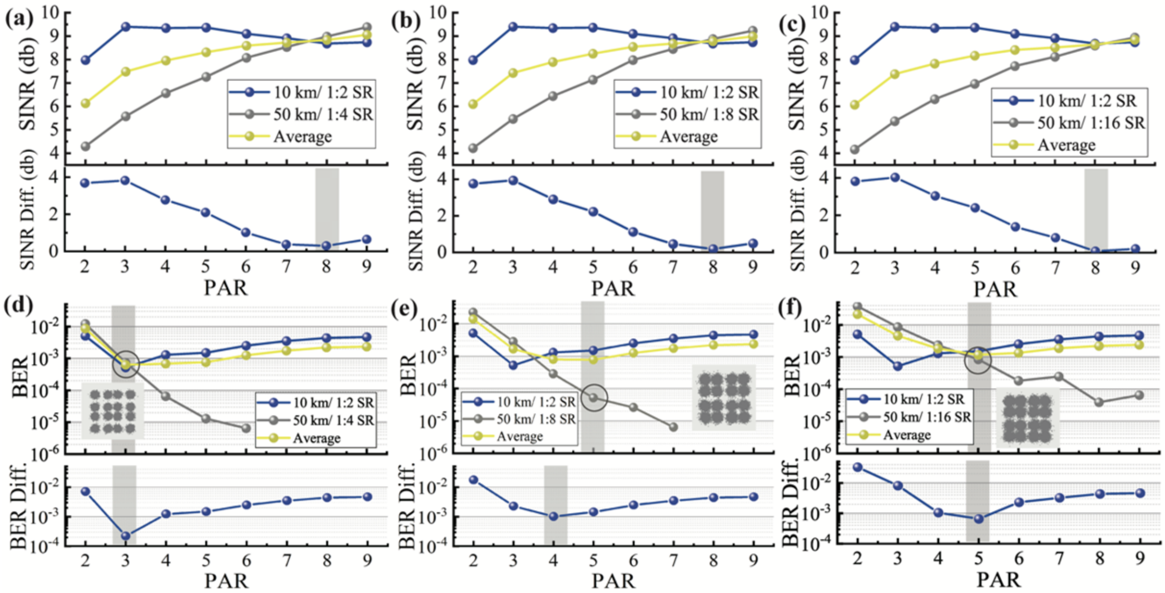

Figure 5.7: Next-generation Super-PON user case with a differential distance of 50 km and smaller SR. The (a) (b) (c) SINR and (d) (e) (f) BER performances between 10-km center ONU 2 with 1:2 SR and 50-km edge ONU 1 with 1:4, 1:8, and 1:16 SR, respectively. The inserted constellation diagrams of far edge ONU 1 in (d) (e) (f) are with the PAR of 3, 5, and 5, respectively.

increased to 1:16, in Fig. 5.6(f) the PAR for minimum differential BER of 5 × 10^{-5} is still at 4, but the PAR for optimal average BER of 1.05 × 10^{-3} moves to 5.

From Fig. 5.7(a) to Fig. 5.7(f), both the SINR and BER curves for 50-km Super-PON access user cases are presented. The SINR curves from Fig. 5.7(a) to Fig. 5.7(c) are similar to the results in 40-km long-reach cases. The minimum SINR difference values are all obtained when the PAR is equal to 8. As shown from Fig. 5.7(d) to Fig. 5.7(f), the optimal average BERs are 6.3 × 10^{-4}, 7.76 × 10^{-4}, and 1.17 × 10^{-3}, respectively. The overall trend is towards a slight increase in the optimized PAR. The minimum differential BERs follow the same situation which are 2.21 × 10^{-4}, 1.014 × 10^{-3}, and 6.55 × 10^{-3}, respectively. By now, four user cases have verified that the proposed TDM-NOMA solution is not only compatible with traditional dense access scenarios but can

Table 5.2: The HD-FEC Thresholds of certain codes recommended.

HD-FEC Code type [1]	Pre-BER	Post-BER	OH [3]	Ref.
Reed–Solomon (RS) (528,514) "KR4" [2]	2.18×10^{-5}	1×10^{-15}	2.7%	[121]
RS (544,514) "KP4"	2.26×10^{-4}	1×10^{-15}	5.8%	[121]
Proprietary "P-FEC"	3.84×10^{-3}	$\leq 1 \times 10^{-15}$	6.7%	[122, 123]
Convolutional + RS	5.20×10^{-3}	1×10^{-15}	24.5%	[121]

also be delivered in the next-generation 40-km suburban access and wide-coverage Super-PON scenarios.

5.4.4 Characterization of service fairness

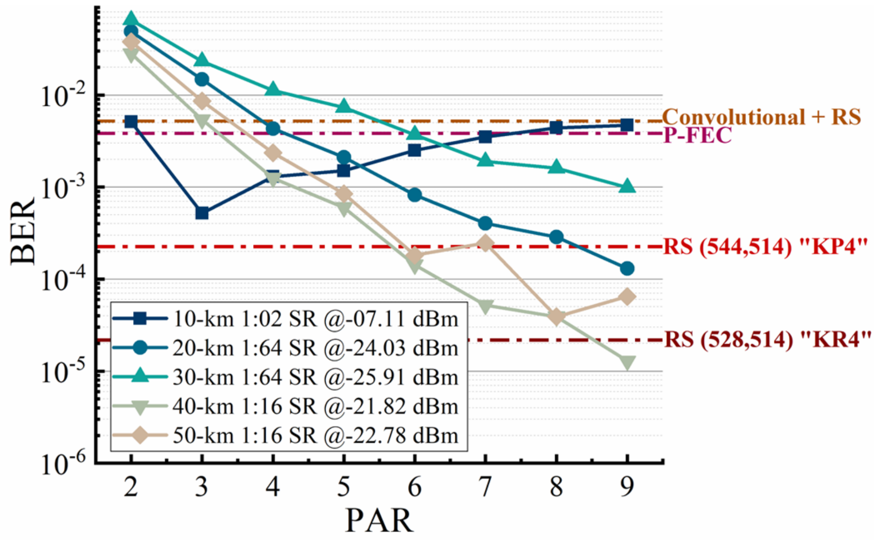

Figure 5.8: The BERs extracted from Fig. 5.4(f), Fig. 5.5(f), Fig. 5.6(f), and Fig. 5.7(f), versus PARs with different HD-FEC standards.

Two far-near users cannot simultaneously demonstrate fairness in SINR and BER under a specific PAR. This reason is mainly due to error propagation caused by imper-

[1]The soft-decision forward error correction (SD-FEC) schemes are not used for fairness service comparison because SD-FEC are typically designed for additive white Gaussian noise (AWGN) channels-based systems. The user case of the proposed TDM-NOMA scheme has inter-user noise interference terms and error propagation at the receiver which do not satisfy the pre-conditions of AWGN [124].

[2]The pre-FEC BERs of two KP4 standard were estimated by the accurate approximation by assuming bounded-distance decoding.

[3]OH: Overhead.

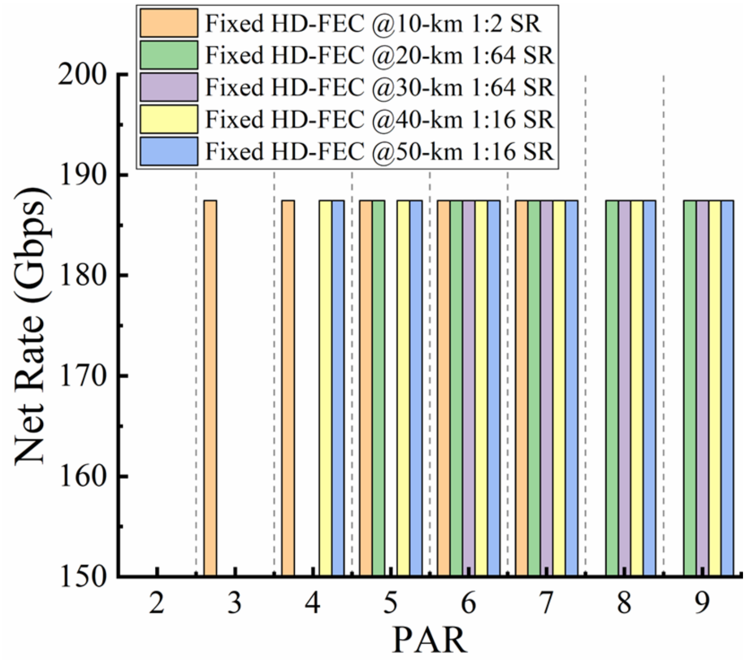

Figure 5.9: The net rates versus PARs for the four user cases with different path losses and SRs using fixed HD-FEC standard. (Adopting P-FEC with a threshold of 3.84×10^{-3}.)

fect SIC receivers. Even though coherent detection provides a relatively wide receiver sensitivity, the complexity of the SIC receiver will also increase with the demodulation level, which further limits the number of users supported by the TDM-NOMA PON solution within a single timeslot. Next, the net rates with various HD-FEC thresholds from a line rate of 200 Gbps are presented, as well as the service fairness indexes. Here, we select each subcase with the worst power budget among the above four user cases (12 subcases in total). It is easy to infer that if the proposed TDM-NOMA performs well in each of the worst subcases, the remaining subcases can obtain better fair service results.

We extract the communication performance BERs data of far edge ONUs 2 from Fig. 5.4(f), Fig. 5.5(f), Fig. 5.6(f), and Fig. 5.7(f) and reorganize them in Fig. 5.8

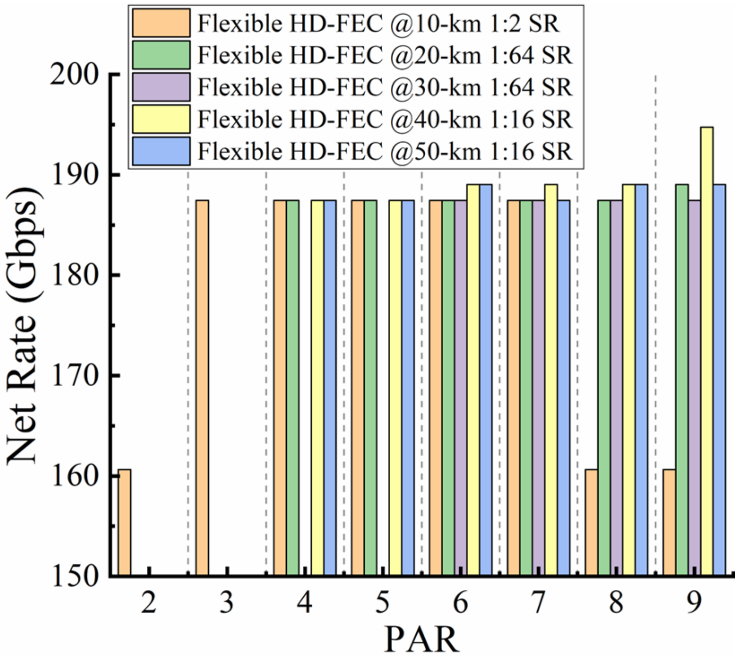

Figure 5.10: The net rates versus PARs for the four user cases with different path losses and SRs using flexible HD-FEC standard from Table. 5.2.

with the BER of near center ONU 1 and with the four HD-FEC standards of Table Table 5.2. Considering dual-polarization transmission, the line rate of each channel is 200 Gbps at 50-Gbaud. The overall communication performances are closely related to ROPs. Next, we consider two situations, including fair serviceability under the fixed HD-FEC standard and the flexible HD-FEC standard. The P-FEC of 3.84×10^{-3} with 6.7% overhead (OH) is one of the most commonly used FEC standards in optical communication links, which is used here for the fixed correction. Anything below this threshold will be corrected and a net rate of 187.44 Gbps will be obtained. As shown in Fig. 5.9, all five ONUs can be lower than the P-FEC threshold of 3.84×10^{-3} by optimizing the allocation of PAR. For example, when PAR is 2, all user cases are higher than the P-FEC threshold, but all lower than the P-FEC threshold and reach a net rate of 187.44 Gbps at the PAR of 6 or 7. In addition, considering that different

ONUs may adopt different FEC standards in next-generation PON, three other HD-FEC standards from Table 5.2 are also adopted for fairness evaluation, including the RS (528, 514) KR4 with 2.7% OH and threshold of 2.18 × 10^{-5}, the RS (544, 514) KP4 with 5.8% OH and threshold of 2.26 × 10^{-4}, and the Convolutional + RS with 24.5% OH and threshold of 5.2 × 10^{-3}. As shown in Fig. 11 with four net rate levels, those with BERs lower than the Convolutional + RS threshold but higher than the P-FEC threshold will get a net rate of 160.64 Gbps, such as the user case at 10 km with 1:2 SR and 2, 8, and 9 PAR. BERs below the P-FEC threshold but above the RS (544, 514) KP4 threshold will be corrected and result in net rates of 187.44 Gbps, which is the same as the fixed FEC situation above. Those lower than the RS (544, 514) KP4 threshold but higher than the RS (528, 514) KR4 threshold will be judged as net rates of 189.04 Gbps. Finally, those below the RS (528, 514) KR4 threshold will get the highest net rates of 194.74 Gbps, where only the 40-km user case with the highest PAR of 9 can get it in Fig. 5.10.

The Jain's fairness indexes versus PAR from 2 to 9 are calculated and presented in Fig. 5.11 and Fig. 5.12 from the actual obtained net rates data for four user cases. From Fig. 5.11(a) to Fig. 5.11(d), the Jain's fairness indexes for four subcases are shown under the fixed HD-FEC standard with P-FEC. Restricted by both two near-far ONUs performances, perfect fairness implementation with Jain's fairness index of 1 can only be within a limited PAR range. For example, in the worst subcase of 30-km 1:64 SR ONU with the lowest ROP of -25.91 dBm, it is only possible to optimize PAR at 6 or 7 to achieve perfect fairness. Compared with fixed HD-FEC, as shown in Fig. 5.12(a) to Fig. 5.12(d), flexible HD-FEC provides a wider PAR optional space. Mainly because

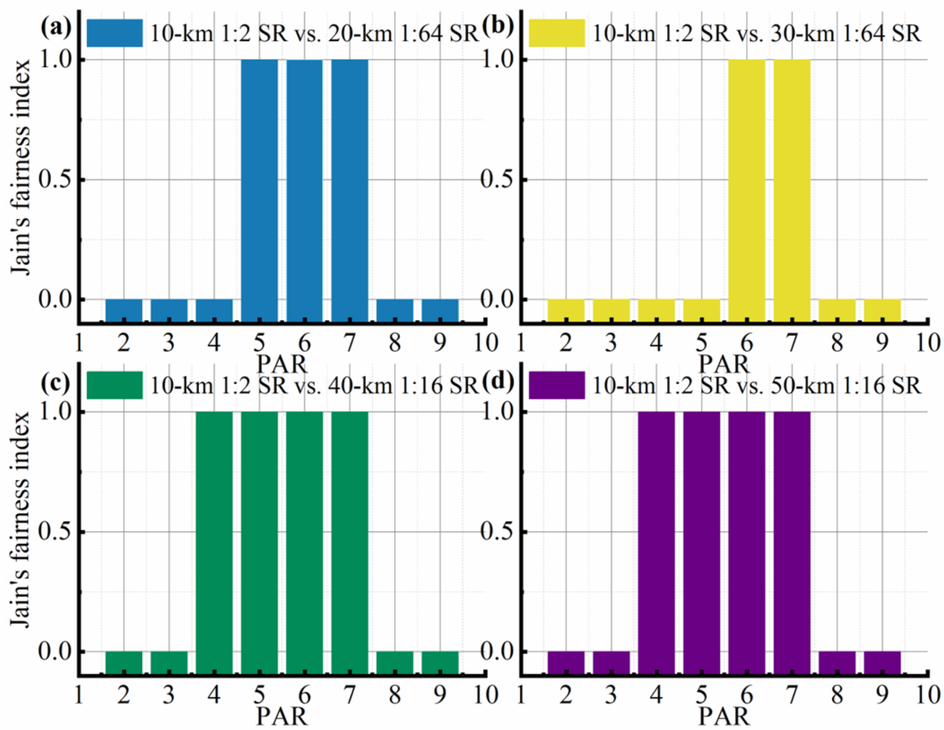

Figure 5.11: The Jain's fairness indexes versus PARs for four user cases using fixed HD-FEC standard with P-FEC.

for 10-km center ONU 1 at PARs of 8 or 9, its BERs are lower than the Convolutional + RS threshold but higher than the P-FEC threshold. The same situation occurs with 20-km edge ONU 2 with the PAR of 4. Furthermore, for the subcases such as the 40-km edge ONU 2 at the PAR of 5 or 6 and the 50-km edge ONU 2 at the PAR of 6, the Jain's fairness indexes very close to 1 due to the net rate of 189.04 Gbps under RS (544, 514) KP4 and 187.44 Gbps under P-FEC are very close in nature.

In addition, the modified fairness indexes are also calculated and presented in Fig. 14 from the perspective of obtained SINR and theoretically achieving channel capacity. These are essentially just estimates for providing a reference without actually being implemented in experiments in this work. From Fig. 5.13(a) to Fig. 5.13(d), the overall convergence situation is mainly related to ROP. For these four user cases, it

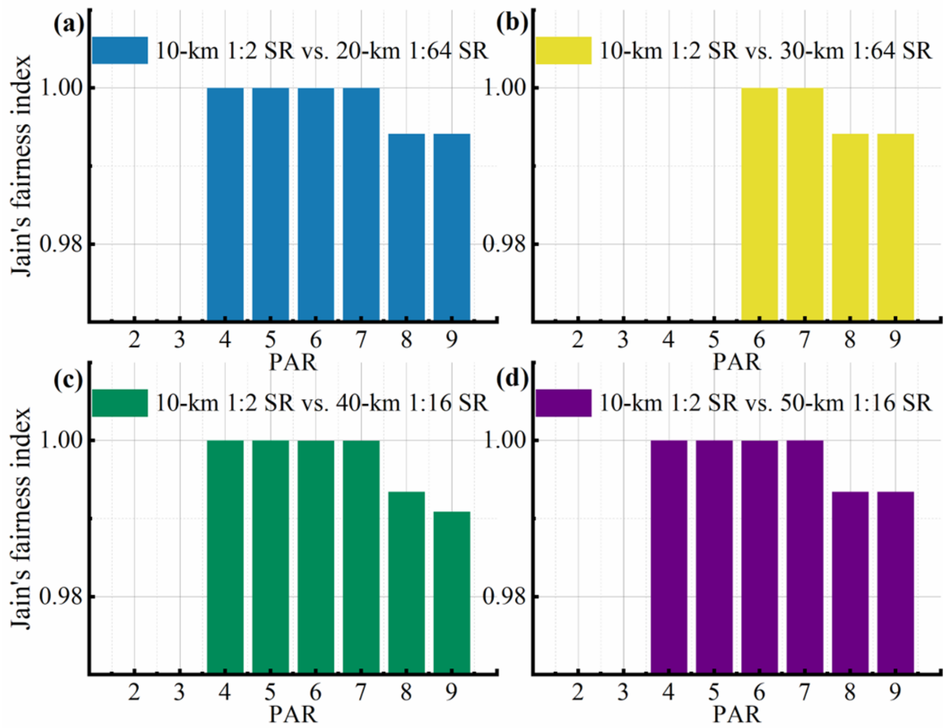

Figure 5.12: The Jain's fairness indexes versus PARs for four user cases using flexible HD-FEC standards.

is not difficult to find that as the power allocation to the far edge ONU increases, its modified fairness indexes gradually approach 1. Even in the worst case for 30-km 1:64 SR edge ONU 2 as shown in Fig. 5.13(b), its modified fairness index can reach 0.976. By adopting the TDM-NOMA schematic with optimizing PAR, fairness can be well guaranteed.

5.5 Section Summary

The service fairness of the far-near user access in 100/ 200-Gbps coherent PON with various user cases is discussed in this work. The first work uses digital-domain power-division NOMA in 100/ 200-Gbps far-near transmission coherent PON.

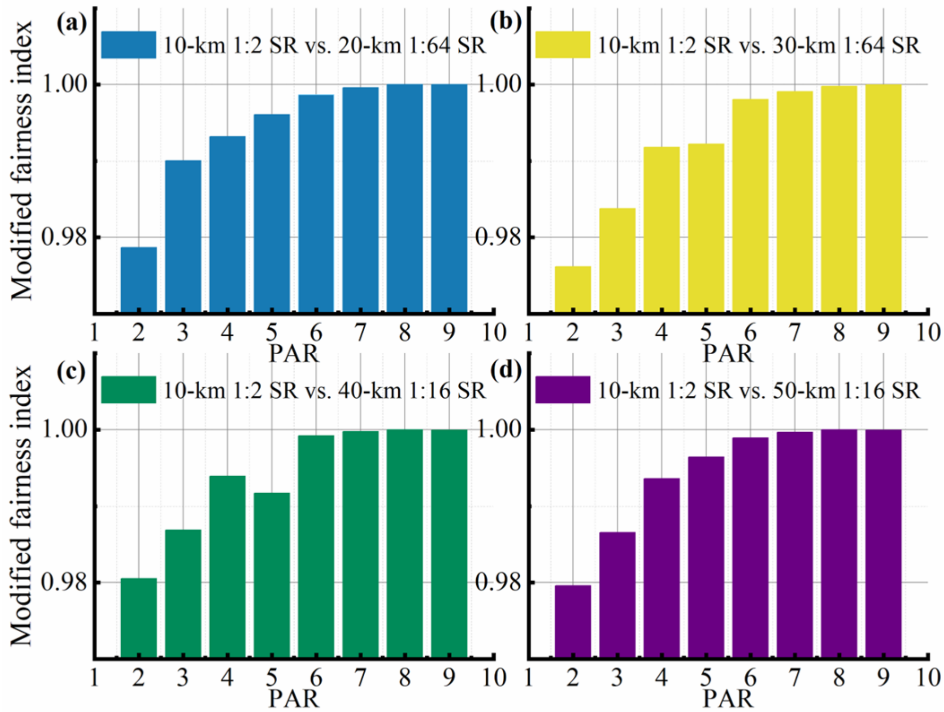

Figure 5.13: The modified fairness indexes versus PARs for four user cases in term of SINR and achieving channel capacity.

Chapter 6

Conclusions

6.1 Summary

To meet the requirement of the development of a high-capacity, rate-flexible, secure, monitorable, and fair coherent optical communication system, and access network, in this thesis, we mainly worked on three selected topics in next-generation CPON. The three main chapters (*from Chapter 3 to Chapter 5*) of the thesis target each one of these research directions (*parameter monitoring, dynamic security, and servicer fairness*). But since meeting the data traffic, dense access and various demands are the main driving forces of the next-generation optical access networks, we focus on DSP-based dynamic behaviors and access methods in all our work.

In **Chapter 3**, a joint PCS and ET-AMI scheme is proposed and demonstrated over a coherent optical transmission system. The entropy-tunable characteristic of PCS enables rate-flexible transmissions. AL is introduced to combine with the CNN-based image classifier. The pool-based AL reduces the training sample size while the

AlexNet performs efficient image feature extraction. The communication performance of the coherent system and the classification accuracy of AL-based ET-AMI with tunable entropy changing in an interval of 0.5 and 0.1 are presented, respectively. The transmission data rate is from 350 to 550 Gbps with a minimal tunable rate of 5 Gbps for each polarization component, and the classification accuracy of AL-based ET-AMI can reach 95% and 99% without and with DA, respectively. Then, the AL-based AMI model is further used to monitor the SNR changing with ROP. The same 87% classification accuracy of AL-based AMI is achieved with an SNR interval of 1 dB with or without DA. Our proposed technique provides a new perspective to develop and manage next-generation rate-flexible coherent optical systems and networks.

We also extend this method from the system to the CPON in **Chapter 3**. Evolved from current rate-fixed PONs, higher-speed and rate-flexible PON systems are urgently needed in the development of next-generation access networks. Here, we present an experimental demonstration of a time-variant entropy-regulated multiple access scheme for FLCS-CPON implemented in a real-time coherent optical transmission system. Different PCS-64-QAM signals with entropies from 3.5 to 5.5 are generated and transmitted, which significantly reduces the BER and improves the performance compared with traditional 64-QAM. A data rate from 350 Gb/s to 450 Gb/s is achieved below the HD-FEC threshold, supporting 5 independent ONUs. The received constellations are sampled, matched, and monitored in real-time by using an NCC template matching algorithm with 96.13% classification accuracy. This work provides a new technical route for future CPON to distinguish different users by regulating the time-varying entropy. Then, to further increase the data rate and rate flexibility of next-generation PONs, we propose and demonstrate a 350-Gb/s/$\lambda \sim$ 450-Gb/s/λ 80-km TWDM-CPON architecture with rate monitoring. The coherent PON is dynamically regulated with time-variant entropy and the transmitted frames allocated to different ONUs can be identified and distinguished by the value of entropy. A 0.5/0.1 interval value of entropy is precisely tuned to achieve a 100%/95% constellation identification accuracy by an AL-based image classifier, corresponding to rate tuning steps of 25 Gb/s and 5 Gb/s at 50 Gband. Due to the query mechanism, the AL-based entropy/rate identification scheme has shown advantages over other schemes in the case of a small sample size. Our work provides a powerful rate monitoring tool for the next-generation rate-adjustable optical access network.

For meeting the requirement of security optical access networks, in **Chapter 4**, a 400-G/80-km PCS-64-QAM-based rate-flexible WDM-CPON with a novel chaotic encryption scheme is proposed for $6\lambda \times 2$ independent ONUs. The entropy-tunable characteristic of PCS enables SE-flexible regulation and rate-flexible transmission. Then, a pseudo-m-QAM mapping method based on a chaotic system is designed for parallel long-sequence encryption, which eliminates the entropy of the transmission sequence and the original mapping relationship. In this work, within the hard-decision FEC limitation, the WDM-CPON configuration at -15 dBm and at 51.12-GBaud can achieve a net 211.80-Gbps $\sim$ 348.12-Gbps encrypted transmission with pseudo-16-QAM format over an 80-km SSMF. At the tunable steps of 0.5/ 0.1 entropies, corresponding to the single-polarized data rate steps of 17.04/ 3.408 Gbps, stable communication performances are achieved over the encrypted pseudo-16-QAM link with the data rates from 211.80 Gbps to 348.12 Gbps. The transceiver's DSP operations are online to support a real-time high-speed coherent transmission. The communication and encryption performances are stable with the wavelengths tuning from 1560 nm to 1562.5 nm for 6 different ONU groups. Then the different encrypted mappings with various m values are also presented and compared. The experimental results show a promising solution for future next-generation rate-flexible and secure 400-G coherent access networks.

We also describe and demonstrate the first real-time PCS-64-QAM coherent flexible MFH with TDMA frame design and chaotic system-based encryption in **Chapter 4**. An FNCC coefficient template matching algorithm was designed to obtain the entropy value among 3.5, 4, and 4.5. The template matching-based pattern recognition accuracy ($\sim$ 97%) obtains the initial values of the chaotic system from the codebook, and then to generate a decrypted long sequence. We demonstrated TDMA frame detection over a real-time coherent transmission platform over a 10-km SSMF. Within the hard-decision forward error correction (FEC) threshold of 3.8×10^{-3}, the net data rate of 225.39-Gbps to 281.62-Gbps transmissions for dual-polarized channels was achieved for next-generation high-capacity B5G C-RAN.

In **Chapter 5**, user service fairness is a key consideration in next-generation coherent PON, which ensures that all users can enjoy fair and high-quality services. Without being unfairly affected by network congestion, resource allocation, or other physical layer factors, this requires access network managers to adopt appropriate strategies to achieve it. A TDM-NOMA solution is proposed over 200-Gbps coherent PON by opening up the two physical dimensions of time-power and ensuring fair rate services within the same timeslot. Four user cases with each three SRs are verified over traditional dense coverage and next-generation long-reach coverage. Twelve subcases were able to achieve almost close SINR or BER by optimized PAR, and the four worst subcases further passed the test of fair index, presenting a result close to 1 at specific PAR values. Similar fairness tests pass for a fixed FEC and four flexible FECs. Our proposed TDM-NOMA solution experimentally demonstrates superiority in meeting the requirement of the development of high-capacity, rate-flexible, fair-service coherent PON.

6.2 Future works

Despite all the results presented in this thesis, there are still opportunities for future projects that can be built upon the completed work. We briefly introduce some of the prospective research avenues based on this thesis. Especially the works on parameter monitoring and service fairness in CPON.

6.2.1 Future works on parameter monitoring

In Chapter 3, according to the experimental results, we would like to discuss some trade-offs and perspectives of our future works, including the identification models and performance indicators.

Classification and regression

In the above experimental work, we abstract and categorize all three independently conducted experiments into a classification problem defined in the field of machine learning and digital image processing. That is, to classify constellation diagrams with different entropies (with intervals of 0.5 and 0.1, respectively) and different SNRs. For the identification problem of variable entropy, a tuning accuracy of 0.1 corresponds to a data rate change of 5 Gbps over the mentioned 50-Gbaud coherent optical system. More flexible data rate changes correspond to less entropy tuning resolution (<0.1 granularity). At the same time, it will make the generated constellation diagram more difficult to distinguish, so a more powerful digital image classifier is required. The identification problem of variable SNR is also converted into a classification problem by grouping in the above experimental demonstration. However, for a practical optical communication system, with the introduction of noise, fluctuations in optical power, and other factors, the SNR often changes continuously. Therefore, the problem of continuous change should be converted into a regression problem with output continuity when abstracting the monitoring model.

Real-time characteristics and complexity

In our proposed CV-aided monitoring solution, the pattern extraction, recognition, comparison, and decision-making of high-dimensional features of images are performed over the generation of the received signal constellation diagrams. Image recognition methods represented by DL have achieved rapid development in the past two decades. However, for optical communication-oriented applications, there are often three dimensions that need to be considered: algorithm complexity (including time and space complexities), training sample size, and recognition accuracy. Typically, low-complexity digital image classifiers have correspondingly low recognition accuracy. These three figures of metrics (FoMs) determine whether the designed algorithm can be well deployed in actual scenarios, due to the strong real-time and embedded nature of optical communication systems and networks. AL acts as a tool for accelerating convergence for conventional CNN, and finds a good balance between training sample size and recognition accuracy. However, the complexity of the algorithm leads us to perform offline image processing in this work and introduces energy consumption as another consideration, simultaneously. This is a trade-off and also an optimization direction for future work.

6.2.2 Future works on service fairness

In Chapter 5, to meet the wider coverage requirement of the development of future CPON architecture and ensure service fairness, some trade-offs and perspectives about further works are shared and discussed.

Fairness over Rate-flexible PON

Both 200-Gbps rate-fixed and rate-flexible PON are hot topics and are compatible with the above solutions. The theoretical part of Section 2 applies to both rate-fixed and rate-flexible TDM-NOMA PON systems. However, in the experimental parts of Section 3 and Section 4, we only demonstrated rate-fixed coherent PON. For the rate-fixed PON, the limitation is obvious, because in an actual PON deployment within a certain standard power budget, the gain of the proposed TDM-NOMA scheme is the performance improvement of SINR and the reduction of BER. However, for the rate-flexible PON, the improvement brought by the proposed solution is significant, because the gain brought by power allocation can directly lead to increases in the entropy of the transmitted signal, thereby further changing the throughput rate.

SIC-free ONU Receiver

In the above proposed digital-domain power-division NOMA solution, the most obvious DSP cost is the introduction of SIC operations on the receiving ONU side. The complexity of the receiver and the allocation of power are used to achieve transmission of two far-near users with similar performance in the same timeslot. However, on the one hand, a single ONU receiver usually needs to consider the energy consumption caused by the DSP chip, especially in dense access scenarios. As a point-to-multi-point network topology, OLT can be designed to be very complex, but ONU sides should be designed as simple as possible, which is the current mainstream. On the other hand, SIC will lead to error propagation and obvious signal transmission delay. Decoding errors generated by the previous user will be accumulated by the next user. Combined with the receiving sensitivity requirements, this characteristic directly causes the proposed TDM-NOMA solution cannot superimpose too many users at the transmitter side DSP when performing SC operations. This solution can generally optimize service fairness between two to three users, limited by the SIC and sensitivity range.

Bibliography

[1] Ji Zhou, Zhenping Xing, Haide Wang, Kuo Zhang, Xi Chen, Qiguang Feng, Keshuang Zheng, Yijia Zhao, Zhen Dong, Tao Gui, et al. Flexible coherent optical access: Architectures, algorithms, and demonstrations. *Journal of Lightwave Technology*, 2024.

[2] Elaine Wong. Next-generation broadband access networks and technologies. *Journal of lightwave technology*, 30(4):597–608, 2011.

[3] Leonid G Kazovsky, Wei-Tao Shaw, David Gutierrez, Ning Cheng, and Shing-Wa Wong. Next-generation optical access networks. *Journal of lightwave technology*, 25(11):3428–3442, 2007.

[4] Joseph W. Lechleider. High bit rate digital subscriber lines: A review of hdsl progress. *IEEE Journal on Selected Areas in Communications*, 9(6):769–784, 1991.

[5] Paul W Shumate. Fiber-to-the-home: 1977–2007. *Journal of Lightwave Technology*, 26(9):1093–1103, 2008.

[6] Chang-Hee Lee and Ki-Man Choi. Fiber to the home. In *LEOS 2007-IEEE Lasers and Electro-Optics Society Annual Meeting Conference Proceedings*, pages 937–938. IEEE, 2007.

[7] Thomas Favale, Francesca Soro, Martino Trevisan, Idilio Drago, and Marco Mellia. Campus traffic and e-learning during covid-19 pandemic. *Computer networks*, 176:107290, 2020.

[8] Yuguang Yang, Shupeng Geng, Baochang Zhang, Juan Zhang, Zheng Wang, Yong Zhang, and David Doermann. Long term 5g network traffic forecasting via modeling non-stationarity with deep learning. *Communications Engineering*, 2(1):33, 2023.

[9] Derek Nesset. The progress of higher speed passive optical network standardisation in itu-t. In *2021 European Conference on Optical Communication (ECOC)*, pages 1–4. IEEE, 2021.

[10] Junwen Zhang and Zhensheng Jia. Coherent passive optical networks for 100g/λ-and-beyond fiber access: Recent progress and outlook. *IEEE Network*, 36(2):116–123, 2022.

[11] Fan Li, Zhibin Luo, Mingzhu Yin, Xiaowu Wang, and Zhaohui Li. Architectures and key dsp techniques of next-generation passive optical network (pon). In *2022 Optical Fiber Communications Conference and Exhibition (OFC)*, pages 1–3. IEEE, 2022.

[12] Wey Jun Shan. The outlook for pon standardization: a tutorial. *Journal of Lightwave Technology*, 38(1):31–42, 2019.

[13] Zixian Wei, Zhaoming Wang, Jianan Zhang, Qian Li, Junping Zhang, and HY Fu. Evolution of optical wireless communication for b5g/6g. *Progress in Quantum Electronics*, 83:100398, 2022.

[14] Ying Loong Lee, Donghong Qin, Li-Chun Wang, and Gek Hong Sim. 6g massive radio access networks: Key applications, requirements and challenges. *IEEE Open Journal of Vehicular Technology*, 2:54–66, 2020.

[15] Auwalu Usman, Nadiatulhuda Zulkifli, Mohd Rashidi Salim, Kharina Khairi, and Asrul Izam Azmi. Optical link monitoring in fibre-to-the-x passive optical network (fttx pon): A comprehensive survey. *Optical Switching and Networking*, 39:100596, 2020.

[16] Huda Saleh Abbas and Mark A Gregory. The next generation of passive optical networks: A review. *Journal of network and computer applications*, 67:53–74, 2016.

[17] Nurul Ikhwan, Hani Rubiani, Noerlaelly Barorroh Taufik Abdul Ghofur, and Yang Zhu. Fiber to the home (ftth) network design using gigabit passive optical network (gpon) technology using link power budget and rise time budget analysis in cibeber village tasikmalaya. *International Journal of Quantitative Research and Modeling*, 4(1):30–36, 2023.

[18] Chien-Hung Yeh, Wei-Hung Hsu, Bo-Yin Wang, Jhao-Ren Chen, Wei-Yao You, and Chi-Wai Chow. Dual-polarized wdm access network with fiber to the extension (ftte) connection. *IEEE Photonics Journal*, 13(4):1–6, 2021.

[19] Dezhi Zhang, Dekun Liu, Xuming Wu, and Derek Nesset. Progress of itu-t higher speed passive optical network (50g-pon) standardization. *Journal of Optical Communications and Networking*, 12(10):D99–D108, 2020.

[20] Dezhi Zhang, Yuanqiu Luo, and Jialiang Jin. Highspeed 50 gb/s passive optical network (50g-pon) applications in industrial networks. In *2022 IEEE 23rd International Conference on High Performance Switching and Routing (HPSR)*, pages 113–118. IEEE, 2022.

[21] Zhenping Xing, Kuo Zhang, Xi Chen, Qiguang Feng, Keshuang Zheng, Yijia Zhao, Zhen Dong, Ji Zhou, Tao Gui, Zhicheng Ye, et al. First real-time demonstration of 200g tfdma coherent pon using ultra-simple onus. In *2023 Optical Fiber Communications Conference and Exhibition (OFC)*, pages 1–3. IEEE, 2023.

[22] Dongxu Zhang, Xiaofeng Hu, Xiaoan Huang, and Kaibin Zhang. Experimental demonstration of 200 gb/s/λ coherent pon with a low-complexity receiver and a multi-purpose neural network. In *2022 Optical Fiber Communications Conference and Exhibition (OFC)*, pages 1–3. IEEE, 2022.

[23] Luiz Anet Neto, Jochen Maes, Per Larsson-Edefors, Junichi Nakagawa, Kiyoshi Onohara, and Stephen J Trowbridge. Considerations on the use of digital signal processing in future optical access networks. *Journal of Lightwave Technology*, 38(3):598–607, 2020.

[24] Yixiao Zhu, Lilin Yi, Bo Yang, Xingang Huang, Jun Shan Wey, Zhuang Ma, and Weisheng Hu. Comparative study of cost-effective coherent and direct detection schemes for 100 gb/s/λ pon. *Journal of Optical Communications and Networking*, 12(9):D36–D47, 2020.

[25] Haide Wang, Ji Zhou, Zhenping Xing, Qiguang Feng, Kuo Zhang, Keshuang Zheng, Xi Chen, Tao Gui, Liangchuan Li, Jianrui Zeng, et al. Fast-convergence digital signal processing for coherent pon using digital scm. *Journal of Lightwave Technology*, 2023.

[26] Zixian Wei, Jinsong Zhang, Weijia Li, and David V Plant. Time-variant entropy regulated multiple access for flexible coherent pon. *Optics Letters*, 47(19):5148–5151, 2022.

[27] Jun Shan Wey and Junwen Zhang. Passive optical networks for 5g transport: technology and standards. *Journal of Lightwave Technology*, 37(12):2830–2837, 2018.

[28] Elaine Wong, Michael Mueller, and Markus C Amann. Characterization of energy-efficient and colorless onus for future twdm-pons. *Optics express*, 21(18):20747–20761, 2013.

[29] Hirotaka Nakamura. Ng-pon2 technologies. In *National Fiber Optic Engineers Conference*, pages NTh4F–5. Citeseer, 2013.

[30] Yuanqiu Luo, Xiaoping Zhou, Frank Effenberger, Xuejin Yan, Guikai Peng, Yinbo Qian, and Yiran Ma. Time-and wavelength-division multiplexed passive

optical network (twdm-pon) for next-generation pon stage 2 (ng-pon2). *Journal of lightwave technology*, 31(4):587–593, 2013.

[31] IEEE LAN/MAN Standards Committee et al. Draft standard for ethernet amendment: Physical layer specifications and management parameters for 25 gb/s, 50 gb/s, and 100 gb/s passive optical networks. *IEEE P802. 3ca/D3*, pages 1–270, 2018.

[32] Ali Shahpari, Ricardo M Ferreira, Ruben S Luis, Zoran Vujicic, Fernando P Guiomar, Jacklyn D Reis, and António L Teixeira. Coherent access: A review. *Journal of Lightwave Technology*, 35(4):1050–1058, 2017.

[33] Massimo Artiglia, Marco Presi, Fabio Bottoni, Mario Rannello, and Ernesto Ciaramella. Polarization-independent coherent real-time analog receiver for pon access systems. *Journal of Lightwave Technology*, 34(8):2027–2033, 2016.

[34] Domaniç Lavery, Sezer Erkilinç, Polina Bayvel, and Robert I Killey. Recent progress and outlook for coherent pon. In *2018 Optical Fiber Communications Conference and Exposition (OFC)*, pages 1–3. IEEE, 2018.

[35] Shaoliang Zhang, Zhen Qu, Fatih Yaman, Eduardo Mateo, Takanori Inoue, Kohei Nakamura, Yoshihisa Inada, and Ivan B Djordjevic. Flex-rate transmission using hybrid probabilistic and geometric shaped 32qam. In *Optical Fiber Communication Conference*, pages M1G–3. Optica Publishing Group, 2018.

[36] Mu Xu, Haipeng Zhang, Zhensheng Jia, and Luis Alberto Campos. Adaptive modulation and coding scheme in coherent pon for enhanced capacity and ru-

ral coverage. In *Optical Fiber Communication Conference*, pages Th5I–4. Optica Publishing Group, 2021.

[37] Marco Presi, Massimo Artiglia, Fabio Bottoni, Mario Rannello, Ivan N Cano, Jaison Tabares, Juan-Camilo Velásquez, Saeed Ghasemi, Victor Polo, Guang Yong Chu, et al. Field-trial of a high-budget, filterless, $\backslash\lambda$-to-the-user, udwdm-pon enabled by an innovative class of low-cost coherent transceivers. *Journal of Lightwave Technology*, 35(23):5250–5259, 2017.

[38] Ricardo M Ferreira, Ali Shahpari, Jacklyn D Reis, and António L Teixeira. Coherent udwdm-pon with dual-polarization transceivers in real-time. *IEEE Photonics Technology Letters*, 29(11):909–912, 2017.

[39] Guoqiang Li, Sizhe Xing, Zhongya Li, Junwen Zhang, and Nan Chi. 200-gb/s/λ coherent tdm-pon with wide dynamic range of¿ 30-db based on local oscillator power adjustment. In *Optical Fiber Communication Conference*, pages Th3E–3. Optica Publishing Group, 2022.

[40] Junwen Zhang, Zhensheng Jia, Mu Xu, Haipeng Zhang, and Luis Alberto Campos. Efficient preamble design and digital signal processing in upstream burst-mode detection of 100g tdm coherent-pon. *Journal of Optical Communications and Networking*, 13(2):A135–A143, 2021.

[41] Claudio DeSanti, Liang Du, Jhon Guarin, Jason Bone, and Cedric F Lam. Super-pon: an evolution for access networks. *Journal of optical communications and networking*, 12(10):D66–D77, 2020.

[42] Zixian Wei, Jinsong Zhang, Weijia Li, and David V Plant. 400-gbps/80-km rate-flexible pcs-64-qam wdm-cpon with pseudo-m-qam chaotic physical layer encryption. *Journal of Lightwave Technology*, 41(8):2413–2424, 2023.

[43] J Molina-Luna, R Gutiérrez-Castrejón, and DE Ceballos-Herrera. Alternative to super-pon downstream transmitter using a directly-modulated soa. *Optical and Quantum Electronics*, 54(12):830, 2022.

[44] Tanjila Ahmed, Sabidur Rahman, Sifat Ferdousi, Massimo Tornatore, Abhijit Mitra, Bijoy Chand Chatterjee, and Biswanath Mukherjee. Dynamic routing, spectrum, and modulation-format allocation in mixed-grid optical networks. *Journal of Optical Communications and Networking*, 12(5):79–88, 2020.

[45] Dave Welch, Antonio Napoli, Johan Bäck, Sanketh Buggaveeti, Carlos Castro, Aaron Chase, Xi Chen, Vince Dominic, Thomas Duthel, Tobias A Eriksson, et al. Digital subcarrier multiplexing: enabling software-configurable optical networks. *Journal of Lightwave Technology*, 41(4):1175–1191, 2023.

[46] Zixian Wei, Jinsong Zhang, Weijia Li, and David V Plant. Active learning-aided cnn-based entropytunable automatic modulation identification for rate-flexible coherent optical system. *Journal of Lightwave Technology*, 2023.

[47] Martin Maier. Toward 6g: A new era of convergence. In *Optical Fiber Communication Conference*, pages F4H–1. Optica Publishing Group, 2021.

[48] Lisu Yu, Jingxian Wu, Andong Zhou, Erik G Larsson, and Pingzhi Fan. Massively distributed antenna systems with nonideal optical fiber fronthauls: A

promising technology for 6g wireless communication systems. *IEEE Vehicular Technology Magazine*, 15(4):43–51, 2020.

[49] Ippokratis Sartzetakis, Konstantinos Christodoulopoulos, and Emmanuel Varvarigos. Cross-layer adaptive elastic optical networks. *Journal of Optical Communications and Networking*, 10(2):A154–A164, 2018.

[50] Ruijie Zhu, Shihu Li, Peisen Wang, and Junling Yuan. Time and spectrum fragmentation-aware virtual optical network embedding in elastic optical networks. *Optical Fiber Technology*, 54:102117, 2020.

[51] Qunbi Zhuge, Mohamed Morsy-Osman, Xian Xu, Mathieu Chagnon, Meng Qiu, and David V Plant. Spectral efficiency-adaptive optical transmission using time domain hybrid qam for agile optical networks. *Journal of lightwave technology*, 31(15):2621–2628, 2013.

[52] Long Gong and Zuqing Zhu. Virtual optical network embedding (vone) over elastic optical networks. *Journal of Lightwave Technology*, 32(3):450–460, 2013.

[53] Junwen Zhang, Zhensheng Jia, Haipeng Zhang, Mu Xu, Jingjie Zhu, and Luis Alberto Campos. Rate-flexible single-wavelength tfdm 100g coherent pon based on digital subcarrier multiplexing technology. In *2020 Optical Fiber Communications Conference and Exhibition (OFC)*, pages 1–3. IEEE, 2020.

[54] Jose Krause Perin, Anujit Shastri, and Joseph M Kahn. Design of low-power dsp-free coherent receivers for data center links. *Journal of Lightwave Technology*, 35(21):4650–4662, 2017.

[55] Jose Krause Perin, Anujit Shastri, and Joseph M Kahn. Coherent data center links. *Journal of Lightwave Technology*, 39(3):730–741, 2020.

[56] Di Che, An Li, Xi Chen, Qian Hu, Yifei Wang, and William Shieh. Stokes vector direct detection for linear complex optical channels. *Journal of Lightwave Technology*, 33(3):678–684, 2014.

[57] Antonio Mecozzi, Cristian Antonelli, and Mark Shtaif. Kramers–kronig coherent receiver. *Optica*, 3(11):1220–1227, 2016.

[58] Naoki Suzuki, Hiroshi Miura, Keita Mochizuki, and Keisuke Matsuda. Simplified digital coherent-based beyond-100g optical access systems for b5g/6g. *Journal of Optical Communications and Networking*, 14(1):A1–A10, 2022.

[59] Robert Borkowski, Michael Straub, Yanni Ou, Yannick Lefevre, Željko L Jelić, Wouter Lanneer, Noriaki Kaneda, Amitkumar Mahadevan, Volker Hückstädt, Dora van Veen, et al. Flcs-pon–a 100 gbit/s flexible passive optical network: Concepts and field trial. *Journal of Lightwave Technology*, 39(16):5314–5324, 2021.

[60] Paola Parolari, Alberto Gatto, Christian Neumeyr, and Pierpaolo Boffi. Flexible transmitters based on directly modulated vcsels for next-generation 50g passive optical networks. *Journal of Optical Communications and Networking*, 12(10):D78–D85, 2020.

[61] Robert Borkowski, Michael Straub, Yanni Ou, Yannick Lefevre, Željko Jelić, Wouter Lanneer, Noriaki Kaneda, Amitkumar Mahadevan, Volker Hückstädt, Dora van Veen, et al. World's first field trial of 100 gbit/s flexible pon (flcs-pon).

In *2020 European Conference on Optical Communications (ECOC)*, pages 1–4. IEEE, 2020.

[62] Borui Li, Derek Nesset, Dekun Liu, Zhicheng Ye, and Liangchuan Li. Dsp enabled next generation flexible pon for 50g and beyond. In *Optical Fiber Communication Conference*, pages M3G–1. Optica Publishing Group, 2022.

[63] Philipp C Schindler, R Schmogrow, Michael Dreschmann, Joachim Meyer, Ioannis Tomkos, J Prat, H-G Krimmel, Thomas Pfeiffer, Pandelis Kourtessis, A Ludwig, et al. Colorless fdma-pon with flexible bandwidth allocation and colorless, low-speed onus. *Journal of Optical Communications and Networking*, 5(10):A204–A212, 2013.

[64] Rui Zhang, Noriaki Kaneda, Yannick Lefevre, Amitkumar Mahadevan, Doutje van Veen, and Vincent Houtsma. Probabilistic and geometric shaping for next-generation 100g flexible pon. In *2020 European Conference on Optical Communications (ECOC)*, pages 1–4. IEEE, 2020.

[65] Qinghua Xiao, Yifan Chen, Shangxin Lin, Hailian He, Xinxing Wu, Jialin You, Youxu Zeng, Lin Zhou, and Ze Dong. Dft-spread dmt-wdm-pon employing ldpc-coded probabilistic shaping 16 qam. *Journal of Lightwave Technology*, 38(4):714–722, 2020.

[66] Sizhe Xing, Guoqiang Li, Jiang Chen, Junwen Zhang, Nan Chi, Zhixue He, and Shaohua Yu. First demonstration of ps-qam based flexible coherent pon in burst-mode with 300g peak-rate and record dynamic-range and net-rate product up

to 7,104 db· gbps. In *2022 Optical Fiber Communications Conference and Exhibition (OFC)*, pages 1–3. IEEE, 2022.

[67] Fred Buchali, Fabian Steiner, Georg Böcherer, Laurent Schmalen, Patrick Schulte, and Wilfried Idler. Rate adaptation and reach increase by probabilistically shaped 64-qam: An experimental demonstration. *Journal of lightwave technology*, 34(7):1599–1609, 2015.

[68] Robert Borkowski, Yannick Lefevre, Amitkumar Mahadevan, Doutje Van Veen, Michael Straub, Ralph Kaptur, Björn Czerwinski, Bruno Cornaglia, Vincent Houtsma, Werner Coomans, et al. Flcs-pon—an opportunistic 100 gbit/s flexible pon prototype with probabilistic shaping and soft-input fec: operator trial and odn case studies. *Journal of Optical Communications and Networking*, 14(6):C82–C91, 2022.

[69] Patrick Schulte and Georg Böcherer. Constant composition distribution matching. *IEEE Transactions on Information Theory*, 62(1):430–434, 2015.

[70] Junho Cho, Xi Chen, Sethumadhavan Chandrasekhar, Gregory Raybon, Ronen Dar, Laurent Schmalen, Ells Burrows, Andrew Adamiecki, Steve Corteselli, Yan Pan, et al. Trans-atlantic field trial using high spectral efficiency probabilistically shaped 64-qam and single-carrier real-time 250-gb/s 16-qam. *Journal of Lightwave Technology*, 36(1):103–113, 2018.

[71] Bin Chen, Chigo Okonkwo, Hartmut Hafermann, and Alex Alvarado. Increasing achievable information rates via geometric shaping. In *2018 European Conference on Optical Communication (ECOC)*, pages 1–3. IEEE, 2018.

[72] Fred Buchali, Georg Böcherer, Wilfried Idler, Laurent Schmalen, Patrick Schulte, and Fabian Steiner. Experimental demonstration of capacity increase and rate-adaptation by probabilistically shaped 64-qam. In *2015 European Conference on Optical Communication (ECOC)*, pages 1–3. IEEE, 2015.

[73] Benjamin P Smith and Frank R Kschischang. A pragmatic coded modulation scheme for high-spectral-efficiency fiber-optic communications. *Journal of Lightwave Technology*, 30(13):2047–2053, 2012.

[74] Metodi P Yankov, Darko Zibar, Knud J Larsen, Lars PB Christensen, and Søren Forchhammer. Constellation shaping for fiber-optic channels with qam and high spectral efficiency. *IEEE Photonics Technology Letters*, 26(23):2407–2410, 2014.

[75] Lotfollah Beygi, Erik Agrell, Joseph M Kahn, and Magnus Karlsson. Rate-adaptive coded modulation for fiber-optic communications. *Journal of lightwave technology*, 32(2):333–343, 2013.

[76] Lin Jiang, Lianshan Yan, Anlin Yi, Yan Pan, Ming Hao, Wei Pan, and Bin Luo. An effective modulation format identification based on intensity profile features for digital coherent receivers. *Journal of Lightwave Technology*, 37(19):5067–5075, 2019.

[77] Songnian Fu, Zuying Xu, Jianing Lu, Hexun Jiang, Qiong Wu, Zhouyi Hu, Ming Tang, Deming Liu, and Calvin Chun-Kit Chan. Modulation format identification enabled by the digital frequency-offset loading technique for hitless coherent transceiver. *Optics Express*, 26(6):7288–7296, 2018.

[78] Zhenhua Dong, Faisal Nadeem Khan, Qi Sui, Kangping Zhong, Chao Lu, and Alan Pak Tao Lau. Optical performance monitoring: A review of current and future technologies. *Journal of Lightwave Technology*, 34(2):525–543, 2015.

[79] Xiang Lin, Octavia A Dobre, Telex MN Ngatched, Yahia A Eldemerdash, and Cheng Li. Joint modulation classification and osnr estimation enabled by support vector machine. *IEEE Photonics Technology Letters*, 30(24):2127–2130, 2018.

[80] Qun Zhang, Yanfu Yang, Changjian Guo, Xian Zhou, Yong Yao, Alan Pak Tao Lau, and Chao Lu. Accurate ber estimation scheme based on k-means clustering assisted gaussian approach for arbitrary modulation format. *Journal of Lightwave Technology*, 38(8):2152–2157, 2019.

[81] Danshi Wang, Min Zhang, Ze Li, Jin Li, Meixia Fu, Yue Cui, and Xue Chen. Modulation format recognition and osnr estimation using cnn-based deep learning. *IEEE Photonics Technology Letters*, 29(19):1667–1670, 2017.

[82] Qianwu Zhang, Hai Zhou, Yuntong Jiang, Bingyao Cao, Yingchun Li, Yingxiong Song, Jian Chen, Junjie Zhang, and Min Wang. A simple joint modulation format identification and osnr monitoring scheme for imdd oofdm transceivers using k-nearest neighbor algorithm. *Applied Sciences*, 9(18):3892, 2019.

[83] Faisal Nadeem Khan, Kangping Zhong, Xian Zhou, Waled Hussein Al-Arashi, Changyuan Yu, Chao Lu, and Alan Pak Tao Lau. Joint osnr monitoring and modulation format identification in digital coherent receivers using deep neural networks. *Optics express*, 25(15):17767–17776, 2017.

[84] Li Zhang, Xiaolin Zhou, Jianhong Du, and Pengfei Tian. Fast self-learning modulation recognition method for smart underwater optical communication systems. *Optics Express*, 28(25):38223–38240, 2020.

[85] Marc-André Carbonneau, Eric Granger, and Ghyslain Gagnon. Bag-level aggregation for multiple-instance active learning in instance classification problems. *IEEE transactions on neural networks and learning systems*, 30(5):1441–1451, 2018.

[86] Chongfu Zhang, Wei Zhang, Chen Chen, Xiujun He, and Kun Qiu. Physical-enhanced secure strategy for ofdma-pon using chaos and deoxyribonucleic acid encoding. *Journal of Lightwave Technology*, 36(9):1706–1712, 2018.

[87] MS Erkılınç, R Emmerich, KPON Habel, V Jungnickel, C Schmidt-Langhorst, C Schubert, and R Freund. Pon transceiver technologies for $\geq$ 50 gbits/s per λ: Alamouti coding and heterodyne detection. *Journal of Optical Communications and Networking*, 12(2):A162–A170, 2020.

[88] Thomas Pfeiffer, Pascal Dom, Sarvesh Bidkar, François Fredricx, Konstantinos Christodoulopoulos, and René Bonk. Pon going beyond ftth [invited tutorial]. *Journal of Optical Communications and Networking*, 14(1):A31–A40, 2022.

[89] Liang B Du, Xiangjun Zhao, Shuang Yin, Tao Zhang, Adam ET Barratt, Joy Jiang, Daoyi Wang, Junyan Geng, Claudio DeSanti, and Cedric F Lam. Long-reach wavelength-routed twdm pon: technology and deployment. *Journal of Lightwave Technology*, 37(3):688–697, 2019.

[90] Md Saifuddin Faruk, Xiang Li, Derek Nesset, Iván N Cano, Albert Rafel, and Seb J Savory. Coherent passive optical networks: why, when, and how. *IEEE Communications Magazine*, 59(12):112–117, 2021.

[91] Shweta Bhosale, Bhagyashri Darunkar, Nikhil Punekar, Greg MacDonald, and Pramode Verma. Polarization based secure aes key transmission over optical fiber. In *2016 IEEE International Conference on Communications (ICC)*, pages 1–6. IEEE, 2016.

[92] Seok Hee Jeon and Sang Keun Gil. Optical implementation of asymmetric cryptosystem combined with dh secret key sharing and triple des. *Journal of the Optical Society of Korea*, 19(6):592–603, 2015.

[93] Federico Pederzolli, Domenico Siracusa, Andrea Zanardi, Gabriele Galimberti, Domenico La Fauci, and Giovanni Martinelli. Path-based fragmentation metric and rsa algorithms for elastic optical networks. *Journal of Optical Communications and Networking*, 11(3):15–25, 2019.

[94] Vaibhav Poonia and Narendra Singh Yadav. Analysis of modified blowfish algorithm in different cases with various parameters. In *2015 International Conference on Advanced Computing and Communication Systems*, pages 1–5. IEEE, 2015.

[95] Xiaonan Hu, Xuelin Yang, Zanwei Shen, Hao He, Weisheng Hu, and Chenglin Bai. Chaos-based partial transmit sequence technique for physical layer security in ofdm-pon. *IEEE Photonics Technology Letters*, 27(23):2429–2432, 2015.

[96] Jiajia Shen, Bo Liu, Yaya Mao, Rahat Ullah, Jianxin Ren, Jianye Zhao, and Shuaidong Chen. Enhancing the reliability and security of ofdm-pon using modified lorenz chaos based on the linear properties of fft. *Journal of Lightwave Technology*, 39(13):4294–4299, 2021.

[97] Zhao Yang, Junxiang Ke, Qunbi Zhuge, Weisheng Hu, and Lilin Yi. Coherent chaotic optical communication of 30 gb/s over 340-km fiber transmission via deep learning. *Optics Letters*, 47(11):2650–2653, 2022.

[98] Jianxin Ren, Bo Liu, Delin Zhao, Shun Han, Shuaidong Chen, Yaya Mao, Yongfeng Wu, Xiumin Song, Jianye Zhao, Xueyang Liu, et al. Chaotic constant composition distribution matching for physical layer security in a ps-ofdm-pon. *Optics Express*, 28(26):39266–39276, 2020.

[99] Liljana Gavrilovska, Valentin Rakovic, Aleksandar Ichkov, Davor Todorovski, and Simona Marinova. Flexible c-ran: Radio technology for 5g. In *2017 13th International Conference on Advanced Technologies, Systems and Services in Telecommunications (TELSIKS)*, pages 255–264. IEEE, 2017.

[100] Colm Browning, Qixiang Cheng, Nathan C Abrams, Marco Ruffini, Liang Yuan Dai, Liam P Barry, and Keren Bergman. A silicon photonic switching platform for flexible converged centralized-radio access networking. *Journal of Lightwave Technology*, 38(19):5386–5392, 2020.

[101] Junho Cho and Peter J Winzer. Probabilistic constellation shaping for optical fiber communications. *Journal of Lightwave Technology*, 37(6):1590–1607, 2019.

[102] Qi Zhou, Rui Zhang, You-Wei Chen, Shuyi Shen, Shang-Jen Su, Jeffrey Finkelstein, and Gee-Kung Chang. Combining efficient probabilistic shaping and deep neural network to mitigate capacity crunch in 5g fronthaul. In *2020 Optical Fiber Communications Conference and Exhibition (OFC)*, pages 1–3. IEEE, 2020.

[103] Tingwei Wu, Chongfu Zhang, Yuhang Chen, Mengwei Cui, Huan Huang, Zhi Zhang, Heping Wen, Xiong Zhao, and Kun Qiu. Compressive sensing chaotic encryption algorithms for ofdm-pon data transmission. *Optics express*, 29(3):3669–3684, 2021.

[104] Ed Harstead, Doutje van Veen, Vincent Houtsma, and Pascal Dom. Technology roadmap for time-division multiplexed passive optical networks (tdm pons). *Journal of Lightwave Technology*, 37(2):657–664, 2018.

[105] Reuben George Stephen and Rui Zhang. Joint millimeter-wave fronthaul and ofdma resource allocation in ultra-dense cran. *IEEE Transactions on Communications*, 65(3):1411–1423, 2017.

[106] Tania Panayiotou and Georgios Ellinas. Optimal and near-optimal alpha-fair resource allocation algorithms based on traffic demand predictions for optical network planning. *Journal of Optical Communications and Networking*, 13(3):53–68, 2021.

[107] Hassan Khanahmadzadeh, Arash Rezaee, and Lotfollah Beygi. Joint fairness, fragmentation, and physical layer impairments aware routing, spectrum and modulation level allocation in elastic optical network. In *2022 30th International Conference on Electrical Engineering (ICEE)*, pages 1039–1044. IEEE, 2022.

[108] Anastasios Valkanis, Georgios Papadimitriou, Georgia Beletsioti, Emmanouel Varvarigos, and Petros Nicopolitidis. Efficiency and fairness improvement for elastic optical networks using reinforcement learning-based traffic prediction. *Journal of Optical Communications and Networking*, 14(3):25–42, 2022.

[109] Minghan Jia, Weifeng Sun, Zun Wang, Yaohua Yan, Hongyu Qin, and Kelong Meng. Mfbbr: an optimized fairness-aware tcp-bbr algorithm in wired-cum-wireless network. In *IEEE INFOCOM 2020-IEEE Conference on Computer Communications Workshops (INFOCOM WKSHPS)*, pages 171–176. IEEE, 2020.

[110] Ravneet Kaur, Akshita Gupta, Anand Srivastava, Bijoy Chand Chatterjee, Abhijit Mitra, Byrav Ramamurthy, and Vivek Ashok Bohara. Resource allocation and qos guarantees for real world ip traffic in integrated xg-pon and ieee802. 11e edca networks. *IEEE Access*, 8:124883–124893, 2020.

[111] Nafisa Tasneem and Monir Hossen. Traffic localization-based dynamic bandwidth allocation algorithm for improvement of qos in peer-to-peer architecture of passive optical networks. *Optical Fiber Technology*, 67:102722, 2021.

[112] Mohammad Hadi, Chayan Bhar, and Erik Agrell. General qos-aware scheduling procedure for passive optical networks. *Journal of Optical Communications and Networking*, 12(7):217–226, 2020.

[113] István Pelle, Francesco Paolucci, Balázs Sonkoly, and Filippo Cugini. Latency-sensitive edge/cloud serverless dynamic deployment over telemetry-based packet-optical network. *IEEE Journal on Selected Areas in Communications*, 39(9):2849–2863, 2021.

[114] Bingli Guo, Yu Shang, Yunquan Zhang, Wenzhe Li, Shan Yin, Yongjun Zhang, and Shanguo Huang. Timeslot switching-based optical bypass in data center for intrarack elephant flow with an ultrafast dpdk-enabled timeslot allocator. *Journal of Lightwave Technology*, 37(10):2253–2260, 2019.

[115] Lincong Zhang, Jifeng Qi, Kefeng Wei, Wenbo Zhang, Yongxin Feng, and Weigang Hou. High-priority first dynamic wavelength and bandwidth allocation algorithm in twdm-pon. *Optical Fiber Technology*, 48:165–172, 2019.

[116] Jianqiang Hui, Chaoqin Gan, Lijuan Wu, and Zhongsen Xu. High bandwidth utilization dwba algorithm for upstream channel in ng-epon. *IEEE Access*, 10:99435–99444, 2022.

[117] Ammar Rafiq, Muhammad Faisal Hayat, and Muhammad Usman Younus. Dynamic bandwidth allocation algorithm for avoiding frame rearrangement in ng-epon. *Optical Switching and Networking*, 43:100645, 2022.

[118] Damanjeet Kaur, Garima Gupta, and Vivekanand Jha. A game theoretic bandwidth allocation scheme towards improving the fairness of xg-pon systems. In *2021 International Conference on Information and Communication Technology Convergence (ICTC)*, pages 921–926. IEEE, 2021.

[119] Nan Feng and Xiang Sun. Implementation of network-coding approach for improving the ber performance in non-orthogonal multiple access (noma)-pon. *Optics Communications*, 462:125301, 2020.

[120] Qiong Wu, Zhenhua Feng, Ming Tang, Xiang Li, Ming Luo, Huibin Zhou, Songnian Fu, and Deming Liu. Digital domain power division multiplexed dual polarization coherent optical ofdm transmission. *Scientific reports*, 8(1):15827, 2018.

[121] Erik Agrell and Marco Secondini. Information-theoretic tools for optical communications engineers. In *2018 IEEE Photonics Conference (IPC)*, pages 1–5. IEEE, 2018.

[122] LE Nelson, SL Woodward, S Foo, X Zhou, MD Feuer, D Hanson, D McGhan, H Sun, M Moyer, MO Sullivan, et al. Performance of a 46-gbps dual-polarization qpsk transceiver with real-time coherent equalization over high pmd fiber. *Journal of Lightwave Technology*, 27(3):158–167, 2009.

[123] Kim Roberts, Qunbi Zhuge, Inder Monga, Sebastien Gareau, and Charles Laperle. Beyond 100 gb/s: capacity, flexibility, and network optimization. *Journal of Optical Communications and Networking*, 9(4):C12–C24, 2017.

[124] Junho Cho, Chongjin Xie, and Peter J Winzer. Analysis of soft-decision fec on non-awgn channels. *Optics Express*, 20(7):7915–7928, 2012.